Max-Planck-Institut
für Meteorologie

MAX PLANCK
GESELLSCHAFT

International Max Planck Research School
on Earth System Modelling

Historical Warming and Climate Sensitivity

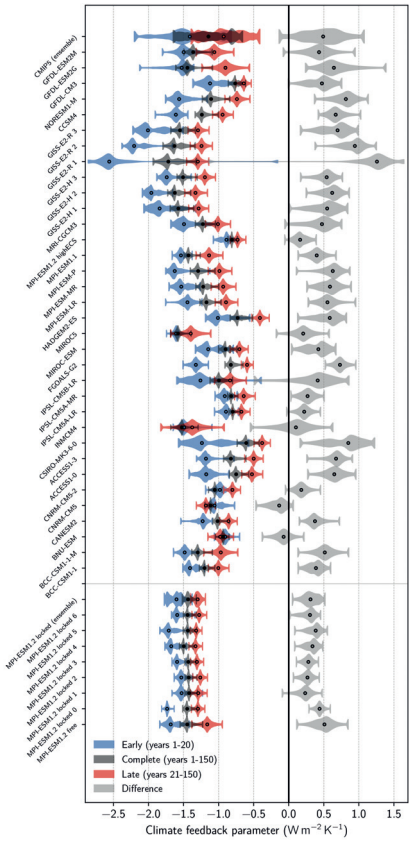

Diego Jiménez-de-la-Cuesta Otero

Hamburg 2020

Berichte zur Erdsystemforschung
Reports on Earth System Science

231
2020

Hinweis

Die Berichte zur Erdsystemforschung werden vom Max-Planck-Institut für Meteorologie in Hamburg in unregelmäßiger Abfolge herausgegeben.

Sie enthalten wissenschaftliche und technische Beiträge, inklusive Dissertationen.

Die Beiträge geben nicht notwendigerweise die Auffassung des Instituts wieder.

Die "Berichte zur Erdsystemforschung" führen die vorherigen Reihen "Reports" und "Examensarbeiten" weiter.

Notice

The Reports on Earth System Science are published by the Max Planck Institute for Meteorology in Hamburg. They appear in irregular intervals.

They contain scientific and technical contributions, including Ph. D. theses.

The Reports do not necessarily reflect the opinion of the Institute.

The "Reports on Earth System Science" continue the former "Reports" and "Examensarbeiten" of the Max Planck Institute.

Anschrift / Address

Max-Planck-Institut für Meteorologie
Bundesstrasse 53
20146 Hamburg
Deutschland

Tel./Phone: +49 (0)40 4 11 73 - 0
Fax: +49 (0)40 4 11 73 - 298

name.surname@mpimet.mpg.de
www.mpimet.mpg.de

Layout

Bettina Diallo and Norbert P. Noreiks
Communication

Copyright

Historical Warming and Climate Sensitivity

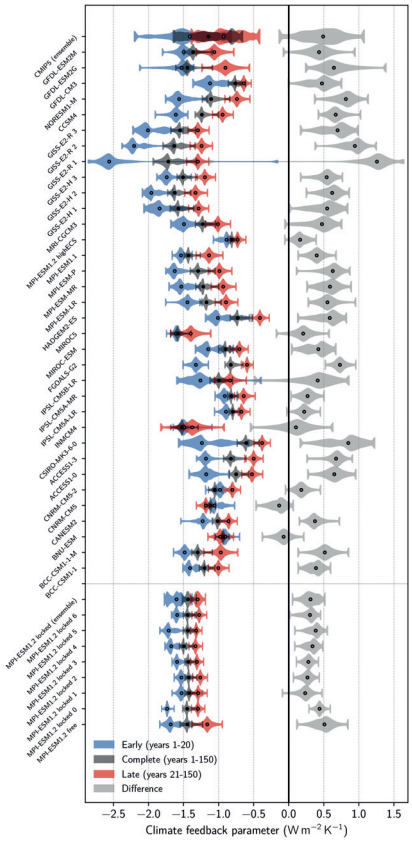

Diego Jiménez-de-la-Cuesta Otero

Hamburg 2020

Diego Jiménez-de-la-Cuesta Otero
aus Mexiko-Stadt, Mexiko

Max-Planck-Institut für Meteorologie
The International Max Planck Research School on Earth System Modelling
(IMPRS-ESM)
Bundesstrasse 53
20146 Hamburg

Universität Hamburg
Geowissenschaften
Meteorologisches Institut
Bundesstr. 55
20146 Hamburg

Tag der Disputation: 11. Juni 2020

Folgende Gutachter empfehlen die Annahme der Dissertation:
Prof. Dr. Thorsten Mauritsen
Prof. Dr. Björn Stevens

Vorsitzender des Promotionsausschusses:
Prof. Dr. Dirk Gajewski

Dekan der MIN-Fakultät:
Prof. Dr. Heinrich Graener

The figure on the front page presents figure 4.2 (page 44): Modelled climate feedback parameter for CMIP5 models, MPI-ESM1.2-highECS, MPI-ESM1.1 Grand Ensemble and MPI-ESM1.2 free- and locked-cloud experiments. Blue distributions correspond to the early period (years 1 to 20). Red distributions correspond to the late period (years 21 to 150). Dark grey distributions correspond to the complete abrupt4xCO_2 run (years 1 to 150). Light grey distributions show the difference between red and blue. The dots mark the median values of the distributions. The limits mark the 5 to 95 percentile range.

Berichte zur Erdsystemforschung / Max-Planck-Institut für Meteorologie 231
Reports on Earth System Science / Max Planck Institute for Meteorology 2020

ISSN 1614-1199

Abstract

In this dissertation, we study the climate sensitivity of the Earth. The climate sensitivity quantifies the response of the Earth system to radiative forcing, in particular, the radiative forcing induced by humans. We use both complex climate modelling and observations from the historical record for this endeavour. We analyse these data sources from the perspective of a conceptual framework based on the Earth's energy budget. The foci of our study are on two wide topics.

The first topic estimates how sensitive the Earth's climate is to carbon dioxide using the historical warming. We use two quantities to measure the sensitivity: the transient climate response (TCR) and the long-term equilibrium climate sensitivity (ECS). Past studies analysed the historical observations of warming and forcing in the light of the Earth's energy budget to estimate TCR and ECS. We ascertain that some of these calculations underestimate TCR and ECS. First, we analyse the disadvantages of past observational estimates concerning the uncertainties in the anthropogenic radiative forcing. Based on this analysis, we select the post-1970s period. Then we link the modelled warming in this period in complex climate models with the corresponding modelled TCR and ECS. This relationship between warming and sensitivity, and the observed post-1970s warming allow us to estimate TCR and ECS. Our TCR estimate is higher than the past estimates, and we find that this difference can be explained by past studies assuming that the ocean mixed-layer is equilibrated. Our ECS estimate is also higher than some past estimates and is in line with other studies that accounted for the effects of an evolving sea-surface temperature pattern. The evolving sea surface temperature pattern changes the feedback mechanisms on the warming and temporarily counteract the radiative forcing.

The second topic explores the role of clouds in this temporary dampening of the transient global warming. We find that the cloud feedback not only acts directly with the sea surface temperature patterns that arise when the climate system is out of equilibrium, but clouds also affect other relevant feedback mechanisms. Past studies found that the evolving sea surface temperature pattern changes the radiative response between decadal and centennial timescales. A proposed mechanism connects clouds with the evolving pattern. They also show in observations the relationship between the decadal cloud variations and the corresponding variations in the radiative response of the Earth. Assisted by a complex climate model, we find that not only clouds link the evolving pattern with the radiative response, but also that they influence the remaining relevant mechanisms. To unravel the role of clouds, we use a cloud-locking technique which inhibits cloud feedback. We find that: a) clouds explain almost half of the difference in the radiative response between decadal and centennial timescales, and b) a synergy between cloud processes, lapse-rate and water-vapour feedback provides the tropical free-tropospheric warming that the proposed physical mechanism needs.

Zusammenfassung

In dieser Dissertation untersuchen wir die Klimasensitivität der Erde. Die Klimasensitivität misst die Reaktion des Erdsystems auf den Strahlungsantrieb unter besonderer Berücksichtigung des anthropogenen Strahlungantriebes. Dazu verwenden wir sowohl komplexe Klimamodelle, als auch historische Beobachtungen. Wir analysieren beide Datenquellen im physikalisch-konzeptuellen Rahmen des Wärmehaushaltes der Erde. Die Schwerpunkte unserer Untersuchung liegen auf zwei großen Themengebieten.

Das erste Thema schätzt basierend auf der historischen Erwärmung ab wie sensibel das Klima der Erde auf Kohlendioxyd reagiert. Wir verwenden zwei Maße, um die Sensitivität zu messen: die kurzfristige *Transient Climate Response* (TCR) und die langfristige *Equilibrium Climate Sensitivity* (ECS). Vorherige Untersuchungen analysieren historische Beobachtungen der Erwärmung und des Strahlungsantriebes mit dem Wärmehaushalt der Erde, um die TCR und die ECS zu berechnen. Wir stellen fest, dass einige dieser früheren Berechnungen die TCR und die ECS unterschätzen. In dieser Dissertation analysieren wir zuerst die Nachteile dieser früheren Schätzungen in Bezug auf die Messunsicherheit des anthropogenen Strahlungsantriebs. Aufgrund der niedriegeren Messunsicherheit des anthropogenen Aerosolstrahlungsantriebes wählen wir für unsere Analyse den Zeitraum ab den 1970-iger Jahren aus. Dann verbinden wir die modellierte Erwärmung in diesem Zeitraum mit den entsprechenden modellierten TCRs und ECSs. Die ermittelte Beziehung zwischen Erwärmung und Sensitivität und die tatsächliche Erwärmung seit den 1970-iger Jahren macht eine neue Schätzungen der tatsächliche TCR und ECS möglich. Unsere Schätzung der TCR ist höher als die früheren Schätzungen. Wir stellen fest, dass der Unterschied auf eine Annahme vorheriger Schätzungen zurückführbar ist: Bezüglich des Wärmeaustausches ist der gutgemischte Ozean stationär. Unsere Schätzung der ECS ist ebenfalls höher als diejenigen einiger vorheriger Schätzungen. Unsere Schätzung stimmt mit anderen Schätzungen, die die Effekte eines sich entwickelnden Musters der Meeresoberlfächnetemperatur berücksichtigen, überein. Dieses Muster verändert die Rückkopplungsmechanismen und wirkt dem Strahlungsantrieb vorläufig entgegen.

Das zweite Thema handelt von der Rolle der Wolken in dieser vorläufigen Dämpfung der transienten globalen Erwärmung. Wir entdecken, dass die Wolkenrückkopplung nicht nur eine direkte Wirkung hat, sondern auch, dass die Wolken andere relevante Rückkopplungen beeinflussen. Vorherige Untersuchungen stellten fest, dass das sich entwickelnde Muster der Meeresoberflächentemperatur die Strahlungsreaktion zwischen zehn- und hundertjährigen Zeitskalen verändert. Ein möglicher physikalischer Mechanismus, der die Wolken mit dem sich entwickelnden Muster verknüpft, wurde vorgeschlagen. Die Beziehung zwischen den zehnjährigen Schwankungen der Wolken und den entsprechenden Änderungen in der Strahlungsreaktion der Erde konnte bereits durch Beobachtungen verifiziert werden. Mit Hilfe eines komplexen Kimamodells finden wir, dass nicht nur die Wolken das

sich entwickelnde Muster mit der Strahlungsreaktion verknüpfen, sondern auch, dass die Wolke die übrigen relevanten Mechanismen beeinflussen. Um die Rolle der Wolken zu untersuchen, verwenden wir eine "cloud-locking" Technik, die die Wolkenrückkopplung unterbindet. Unser Resultat ist: a) die Wolken erklären fast die Hälfte der Änderung der Strahlungsreaktion zwischen zehn- und hundertjährigen Zeitskalen und b) eine Synergie zwischen Wolkenprozessen, die Temperatur-Gradient- und die Wasserdampfrückkopplung liefert die tropische frei-troposphärische Erwärmung, die der vorgeschlagene physikalische Mechanismus benötigt.

Contents

Climate sensitivity, energy cycle and the instrumental record

Die Erde war da. Grün, blau und weiß.
Wir lebten auf ihrer Haut. Bequem und frei.
Aber der Wechsel kam. Mit uns weg war die Balance.

Traces of the climate change

Fourier (1827) was one of the first to recognise that the atmospheric gases played a role in increasing the surface temperature of the Earth, given that freezing temperatures would be the norm if the atmosphere were transparent to the radiation emitted by the sun-warmed surface. On the wake of the work of Tyndall (1861) on the infrared absorption of various gases, Arrhenius (1896) was the first to quantify the effect of CO_2 in the atmosphere. He speculated on the role of CO_2 in the past variations of the climate. Building upon these ideas, Callendar (1938) took the estimates of the CO_2 actually produced by humans. With a simple energy balance calculation, he concluded that surface temperature would appreciably increase due to CO_2 concentration increments. He looked into temperature observations of the time and found trends in the surface temperature consistent with the CO_2 anthropogenic increase. We show in figure 1.1 the observed changes in the global mean surface temperature and, in comparison, the estimated changes in forcing (IPCC 2013a) along the 20th century and the first years of the 21st century. This figure should make the reader ask if one can dismiss a relationship between warming and anthropogenic forcing.

The instrumental record

We define the instrumental record as the registry of variables that describe the Earth's climate during the historical period (from the 19th and 21st centuries). During the same period advances in Earth system science and high-performance computing became the harbingers of complex Earth system models: numerical models that represent Earth's climate through the circulation of the atmosphere and global ocean and the energy cycle that drives them. The interest in climate science mainly stems from the above-discussed signs of the ongoing human-induced climate change and the question of how sensitive is the Earth's climate to the changes in greenhouse gases and other factors that alter the energy flow in the system.

Energy cycle

Solar shortwave radiation feeds the Earth's energy cycle. A fraction of this radiation is reflected by clouds, aerosol particles and surface features. The net shortwave radiation warms the surface and the atmosphere. Warm bodies emit radiation in such a way that the absorbed energy is balanced by the emitted energy. The Earth's emitted radiation approximately follows the Stefan-Boltzmann law, and it is mostly longwave (or thermal) radiation. The atmospheric greenhouse gases absorb part of the outgoing thermal radiation, acting as a blanket, warming more the surface and establishing a vertical temperature gradient. The remaining radiation that either the atmospheric gases did not absorb or they did not emit towards the ground leaves the system. Now, tropical regions receive more

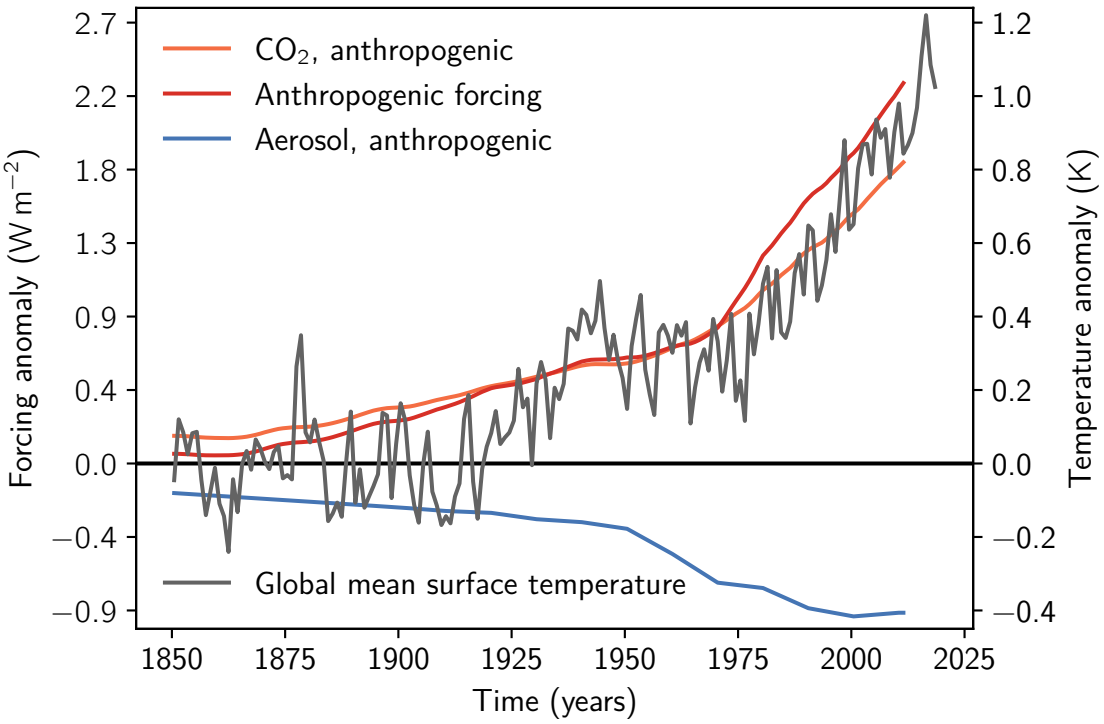

Figure 1.1: Temperature change and human intervention in the radiative forcing. Global mean surface temperature anomaly from the dataset (version 2) provided by Cowtan and Way (2014). The reference period for the temperature anomalies is 1850-1900. The forcing time series are those collected by the IPCC (IPCC 2013a). Note that the striking temperature increase since the 1970s coincides with the increase of the total anthropogenic forcing after the reduction in the anthropogenic aerosol forcing.

shortwave radiation than higher latitudes; therefore, there is also a meridional temperature gradient. In response, mechanisms such as atmospheric and oceanic circulation, convection and clouds, modify the meridional and vertical gradients, the net incoming shortwave energy flux at the top of the atmosphere (TOA) and the outgoing longwave radiation (OLR). If these mechanisms reduce the difference between the TOA incoming and OLR energy fluxes, they are negative feedback mechanisms. Otherwise, they are positive feedback mechanisms.

Forcing, TOA imbalance and steady state

In the outline of the energy cycle presented above, the net radiative forcing is the net radiative input that generates a response in the system through the feedback mechanisms. While the system reacts, there is a non-zero TOA energy imbalance: the difference between the incoming and outgoing energy fluxes at the TOA. On Earth, the global ocean mainly stores the TOA imbalance. If the net response of the system reduces the TOA imbalance, the system is stable to radiative forcing changes. When there are no changes in the radiative forcing, it attains a steady-state which is characterised by the value of the time-averaged state variables and zero time-averaged TOA imbalance (Trenberth et al. 2009; Sherwood et al. 2015).

Human-induced forcing, global warming and sensitivity

During the historical period, humans have introduced changes in the radiative forcing. One example is the increase in atmospheric greenhouse gas concentration, which strengthens

the net radiative forcing by reducing the transparency of the atmosphere to thermal radiation and leading to global warming. Some authors suggest that changes in other state variables scale with changes in global mean surface temperature (e.g. Held and Soden 2006; Lambert and Webb 2008; Hansen et al. 2010). Therefore, global mean surface temperature changes are a proxy of the response of the system. The instrumental record can provide the actual surface temperature, radiative forcing and the TOA imbalance changes. From this data, one can derive metrics of the sensitivity of the Earth to forcing changes and, hopefully, project future climate with the help of scenarios of future radiative forcing. Thus, the sensitivities shall be given as a global mean surface temperature change due to some reference forcing change (Otto et al. 2013; Mauritsen and Pincus 2017).

Definitions of sensitivity

Let us make two thought-experiments to get standard definitions of sensitivity. We assume that we start in a steady-state. The first experiment assumes that we increase the atmospheric CO_2 concentration at a rate of $1\,\%\,\mathrm{yr}^{-1}$ starting from the pre-industrial level. After seventy years, the concentration doubles relative to the pre-industrial concentration. The global mean surface temperature change due to this gradual change in radiative forcing is the transient climate response (TCR, Gregory and Forster 2008). The second thought-experiment assumes that we double the pre-industrial concentration and maintain it afterwards. After the Earth attains a new steady-state, the global mean surface temperature change is the equilibrium climate sensitivity (ECS, Gregory et al. 2004)

TCR and ECS from the instrumental record

An educated-guess tells us that the global mean surface temperature changes are approximately proportional to forcing changes. Also, we can guess that TCR should be proportional to the historical global mean surface temperature change. If these assumptions comply, then the proportionality constant should be the ratio of the forcing changes. In the case of ECS, we need to adjust the first assumption. We do not know the global mean temperature change needed to reach the new steady-state from the instrumental record. However, we know that the thermal capacity of the system stores the TOA imbalance change, delaying the evolution towards the steady-state. Thus, we assume that global mean surface temperature changes are proportional to forcing changes minus the TOA imbalance change that is stored in the system. Thus, we also know that both ECS and the historical global mean surface temperature change are proportional to the ratio of forcing changes minus TOA imbalance changes (Otto et al. 2013).

Instrumental record and forcing uncertainty

As discussed above, observed forcing and global mean surface temperature changes let us derive an estimate of TCR and ECS. Notwithstanding, it is valid to ask how precise and accurate these estimates are when using the instrumental record. The first caveat is that the instrumental record is not uniform in time and space. One of the reasons is that we went from scarce to denser spatial and temporal coverage during the historical period (e.g. for the surface temperature as presented by Cowtan and Way 2014). This problem is not inconsequential for the inference of historical forcing change. In terms of forcing, the anthropogenic forcing components are challenging except for the better-known GHG components (Otto et al. 2013; Mauritsen and Pincus 2017; Gregory et al. 2002; Lewis and Curry 2014). For example, the direct aerosol forcing change in the historical period is, according to IPCC (2013b), $-0.4\,\mathrm{W\,m}^{-2}$(-1.0–$0.1\,\mathrm{W\,m}^{-2}$, 5-95 percentile range) and the aerosol-cloud interactions contribute $-0.5\,\mathrm{W\,m}^{-2}$(-1.2–$0.0\,\mathrm{W\,m}^{-2}$). Thus, the uncertainty is larger than for GHG (IPCC 2013b). The geographical shift of the sources of aerosol particles and changes in environmental regulations during the 1970s also grant

time-varying magnitude and uncertainty (Smith et al. 2011; Stevens 2015; Fiedler et al. 2017). Therefore, the high uncertainty in the historical forcing change coming from the aerosol component translates in poor precision and accuracy in the estimates of TCR and ECS.

TOA imbalance uncertainty

Let us turn our attention to the observed TOA imbalance. Estimates of the TOA imbalance can be obtained from satellite measurements of radiative flux, e.g. CERES instruments and their product CERES-EBAF (Loeb et al. 2009). Given that above 90 percent of the TOA imbalance manifests as an increment in the ocean energy content (Levitus et al. 2012; Trenberth and Balmaseda 2014), we can also estimate the TOA imbalance with data from profiling floats, e.g. ARGO floats, from which the energy stored in the oceans can be derived. Other methods include reconstructions from surface temperatures and oceanic transport processes (Zanna et al. 2019) or oxygen and carbon dioxide isotopes (Resplandy et al. 2014). However, such measurment projects' inception came after the 1970s, and ocean heat uptake has only been well-observed since the start of the 21st century (Johnson et al. 2016). Instruments, reconstructions and proxies introduce other kinds of uncertainty. Thus, additional to the uncertainty coming from the historical forcing and warming, uncertainty in the observed TOA imbalance produces a wide range of ECS estimates consistent with the observed warming.

Pattern-effect

When we estimate TCR and ECS from the instrumental record, we rely upon proportionality assumptions. Their physical meaning is that feedback mechanisms and the ocean heat uptake rate are intrinsic characteristics of the system, no matter the state of the system. Several lines of evidence suggest the contrary (Good et al. 2015; Gregory et al. 2015; Armour 2017). If the feedback mechanisms change, the ECS estimated from the instrumental record is severely afflicted by construction, given that the rate of the imbalance change would vary with time. In contrast, both the historical and the TCR-defining forcing should be affected in almost the same proportion and, therefore, the inferred TCR should not be as afflicted as in the case of ECS. The solution to this problem demands an understanding of the physical mechanisms that could vary the feedback mechanisms. Evidence shows that the evolution of the sea surface temperature (SST) spatial pattern connects ocean heat uptake to cloud and atmospheric lapse-rate feedback mechanisms (Zhou et al. 2016; Ceppi and Gregory 2017). The proposed physical mechanism is the tropical deep convection that warms the free-troposphere. This warming propagates and controls the stability in subsidence regions where stratocumulus clouds form, modulating the reflected shortwave radiation and, therefore, the TOA imbalance. This connection is known as the pattern-effect. If we do not account for it, then the inferred ECS would be underestimated as well as the long-term projections of the global mean surface temperature change.

Modelling and the instrumental record

Above, we summarised the caveats that the instrumental record presents as a source of information on the properties of the climate system. The fact is that we have only one realisation of the Earth's climate. With the numerical modelling of the Earth system, we can explore multiple realisations of the instrumental record. It also becomes a useful tool to explore forcing and feedback mechanisms. The trade-off is that modelling only approximates the real system: all models are wrong, but some are useful (Box 1976). Earth system models use process parameterisation through semi-empirical relationships to represent biochemistry, vegetation, land-atmosphere interactions, convection or cloud physics, for

naming some of the parameterised processes (Mauritsen et al. 2012). These approximations stem from limitations in either spatial and temporal resolution or a lack of understanding of the processes. Exhaustive representation of more aspects of the Earth system arguably leads to more accurate representations of it. However, biases persist, e.g. in precipitation. Despite this, we can easily force our modelled Earth system with the appropriate idealised forcing and get its TCR and ECS (Mauritsen et al. 2019). Then, we can figure out what controls the values of these quantities (Mauritsen et al. 2013),Furthermore, we can trace the relationship between historical warming and climate sensitivity on a simulated historical period. However, if we want to understand the physical mechanisms suggested by model output, we need the assistance of simple conceptual modelling to interpret the complex modelling results (Arrhenius 1896; Callendar 1938; Manabe and Strickler 1964; Budyko 1969; Held et al. 2010; Dacie et al. 2019; Kluft and Dacie 2019; Rohrschneider et al. 2019).

In chapter 2, we present the basic conceptual framework used to interpret the instrumental record and the model output. Afterwards, in chapter 3, we take the instrumental record, select a period from it that has less uncertainty in the anthropogenic aerosol forcing change and during which most of the net anthropogenic forcing change has been applied. Then, we use the model output from the Climate Model Inter-comparison Project phase 5 (CMIP5) to reduce the uncertainty in the observational estimates of TCR and ECS and interpret this reduction in terms of the physical insight given by the conceptual framework (Jiménez-de-la-Cuesta and Mauritsen 2019). In chapter 4, we test the hypothesis that the cloud feedback contributes the most to the pattern-effect, by contrasting standard experiments and experiments without cloud feedback in one complex Earth system model. Throughout this thesis, we emphasise how crucial conceptual understanding is for the interpretation of the instrumental record and other modelling tools.

Earth's energy cycle and the two-layer model

Ahora la vida se tuerce,
El mundo de dolor perece.
Ese mundo verdeazulado ha pasado.
Se hunde agobiado, enfermo, acabado.

We introduced the concept of the energy cycle in chapter 1. In this chapter, we shall formalise it mathematically with the help of the principle of conservation of energy. The resulting conceptual framework, the two-layer model, and its mathematical form presented henceforth, shall be the reference frame to interpret the results in the following chapters.

2.1 Planetary energy budget

Forcing and feedback

The Earth's climate system obeys the principle of conservation of energy. Gauss's divergence theorem ensures that the change in internal energy of the system is equal to the energy imbalance at the top of the atmosphere (TOA). The energy imbalance at the TOA is the difference between the net incoming solar radiation flux at TOA and the outgoing longwave radiation (OLR). If no changes happen in the incoming and outgoing fluxes, the TOA energy imbalance is zero. If the TOA imbalance is not zero, then the system is under radiative forcing. Depending on the sign of the radiative forcing, the system gains or loses internal energy. Thus, its state changes. The state variables, such as surface temperature, describe the state of the system and, therefore, these variables change. The feedback mechanisms that we mentioned in chapter 1 respond to the temperature changes, modify the radiative properties of the system and change the TOA imbalance. If the net feedback is negative, the system minimises the TOA imbalance. Thus, if the radiative forcing becomes constant in time and the climate feedback is negative, then there exists a state where the radiative response of the feedback mechanisms counteract the radiative forcing, leading to no net gain or loss of internal energy: a stable steady-state.

The planetary budget equation

Let us assume that a stable steady-state exists. Then the feedback mechanisms counteract small deviations from zero in the TOA energy imbalance. We also assume that there is intrinsic variability in the system around this steady-state. The complex interactions between components in the system generate this variability. It can be approximated as stochastic noise either on the radiation balance (Hasselmann 1976) or the exchange of energy with the deep oceans. Therefore, the time-averaged value of the TOA imbalance change is zero at the steady-state. Also, the time-averaged global mean surface temperature characterises the state. The radiative forcing also determines the steady-state, because the time-averaged radiative response of the system should cancel out the time-averaged net radiative forcing in the steady-state. Thus, provided that the system stays in a neighbourhood of the steady-state, deviations from the time-averaged values of the TOA

imbalance, radiative forcing, and response at the steady-state describe any other state. Henceforth, N, F and R are the deviations from the steady-state for the TOA imbalance, forcing and response, respectively. Then we write the principle of conservation of energy as

$$N = F + R \tag{2.1}$$

The interplay of forcing and response through feedback mechanisms gives the name of the forcing-feedback framework to this theory (Sherwood et al. 2015).

Form in equilibrium

In this formulation, the steady-state reduces equation (2.1) to the expression $0 = 0 + 0$ with $N = F = R = 0$. If the system finds another steady-state after a forcing perturbation, the corresponding TOA imbalance anomaly is 0 and equation (2.1) becomes $R = -F$: the system's response balances the forcing.

2.1.1 General definitions of ECS and TCR

We now formulate the quantities at the spotlight of this thesis: the equilibrium climate sensitivity (ECS) and the transient climate response (TCR). These measures of the sensitivity to the radiative forcing show the effects of the changes in radiative forcing as global mean surface temperature changes.

General definition of ECS

Let us assume that we start at a steady-state Earth with atmospheric CO_2 concentration at pre-industrial levels. We abruptly double the CO_2 concentration and maintain it afterwards. Thus, $F(0) = 0$, $F(t) = F_{2x}$ for $t > 0$. Here, $F_{2x} \approx 3.7\,\mathrm{W\,m^{-2}}$ is the radiative forcing due to the doubling. Just after the sudden forcing, $N = F_{2x}$. The system will gradually respond by counteracting the forcing anomaly, $R = N - F_{2x}$. If the system attains another steady-state compatible with $F = F_{2x}$, then the global mean surface temperature change at the new equilibrium defines ECS (Gregory and Forster 2008).

Abrupt forcing and other equilibrium sensitivities

The abrupt forcing in the definition of the ECS is only a convenience. Provided that the system has no bifurcations and that the period in which the radiative forcing changes is finite, the radiative forcing evolution from zero to the doubling can be applied in any way imaginable, and there will be no difference in the new steady-state that defines the ECS. However, the new steady-state can differ depending on the feedback mechanisms that are included. If the global carbon cycle, the ice sheet or the vegetation evolve, we define more general steady-states that define other equilibrium sensitivities such as the Earth System Sensitivity (ESS Lunt et al. 2010).

General definition of TCR

We look now at the transient response of the system to radiative forcing. If the system is under a continuously-changing forcing, it does not attain another steady-state. To explore the transient behaviour, we use a forcing that evolves with a similar timescale as the length of the historical period. Let us assume that we start at a steady-state Earth with atmospheric CO_2 pre-industrial conditions. Then we raise concentration at a rate of $1\,\%\,\mathrm{yr^{-1}}$ compound, an exponential growth. The time of the doubling is at $t_{2x} = \ln(2)/\ln(1.01) \approx 70\,\mathrm{yr}$. Since Arrhenius (1896) times, we know that the radiative forcing due to CO_2 is an approximately-logarithmic function of the concentration. Thus, the forcing evolves linearly $F(t) = (F_{2x}/t_{2x})t$, where $F(t_{2x}) = F_{2x}$. The global mean surface temperature change at $t = t_{2x}$ defines TCR (Gregory and Forster 2008).

Modelling quirks

These definitions rest on idealised experiments coming from the modelling world. However, in practice, these definitions are not followed strictly. For example, given that

complex climate models have internal variability, TCR is not the global mean surface temperature change at the time of the doubling but typically taken to be the average global mean surface temperature change in a 20-year period centred at t_{2x}. This averaging smooths the variability coming from the complex interactions between the components of the Earth system. In the case of fully coupled models, the time to attain a new steady-state in the ECS-defining experiment can be in the order of millennia due to the ocean's thermal capacity. Thus, an accurate estimate of ECS is not affordable usually. Therefore, we use a linear ordinary least-squares regression of annually-averaged global mean TOA imbalance change on the global mean surface temperature change using the first 150 years of the experiment. With the regression line, we extrapolate to $N = 0$, and the corresponding global mean surface temperature change is the estimate of ECS (Gregory et al. 2004).

2.1.2 Evolution of the energy cycle and thermal capacity

Evolution of the energy cycle

Gauss's theorem ensures the equality of the TOA imbalance and the change in the internal energy of the system. Although the Earth is not in thermodynamical equilibrium with its surroundings and, thus, a thermodynamical temperature of the planet remains undefined, surface temperature changes are related to the amount of energy that is gained or lost by the planet. Thus, the global mean surface temperature change T is related to the change in internal energy via the concept of thermal capacity. Assuming that T completely describes the state, then $N := C\dot{T}$, where $\dot{T} := dT/dt$. Thus, the equation (2.1) is a first-order differential equation that describes the evolution of Earth's energy cycle. The thermal capacity of the system C is the amount of energy needed to change the temperature of the system in one degree Kelvin. Thus, C delays global warming and sets a timescale to achieve equilibrium. Therefore, the value of C should not modify ECS but affects TCR.

Units of the thermal capacity

Usual thermal capacities have units of $J\,K^{-1}$. Dimensional analysis of $N := C\dot{T}$ results in $[C] = J\,K^{-1}\,m^{-2}$. Then C is a thermal capacity per unit of area. The high thermal capacity of water makes the global ocean the main energy reservoir in the Earth system. One can argue that Earth's crust is large enough to supersede the global ocean, but the conductivity of rock and soil restricts the thermally-active crust to only a few metres in comparison to the kilometres provided by the fluid ocean. Therefore, we refer all thermal capacities in the Earth system to the volumetric thermal capacity of pure water, $c_w = 4.181 \times 10^6\,J\,K^{-1}\,m^{-3}$. Thus, $C = hc_w$, where h is the depth of a layer of water covering the whole Earth with a thermal capacity per unit of area equivalent to C.

2.2 Linearisation of the planetary budget equation

Climate feedback parameter

There is no closed mathematical expression for the radiative response. A first approximation to the radiative response considers the overall contribution of all the feedbacks and assumes feedbacks that only depend on T. We linearise such radiative response using the usual Taylor power series $R(T) = R(0) + R'(0)T + \dots$. We assume that the series exists and converges around the steady-state. By construction, $R(0) = 0$ and we write $R(T) = R'(0)T + \dots$, where $R'(T) := dR/dT$. The factor $\lambda := R'(0)$ is the climate feedback parameter (Gregory et al. 2004) and measures how the system counteract TOA imbalance changes expressed as changes in surface temperature stemming from TOA imbalance changes. We assume that

λ is an intrinsic characteristic of the system. Later, we will discuss how this assumption breaks. With the proposed linearisation, equation (2.1) becomes

$$N = C\dot{T} \approx F + \lambda T \tag{2.2}$$

where $[\lambda] = W\,m^{-2}\,K^{-1}$ and $\lambda < 0$ in a stable Earth system.

Linearised definition of ECS and TCR

Using the definition of ECS in equation (2.2), we obtain that ECS $\approx -F_{2x}/\lambda$. For TCR, we solve the differential equation (2.2) and obtain the solution TCR $\approx (ECS/t_{2x})\{(C/\lambda)[1-\exp((\lambda/C)t_{2x})] + t_{2x}\}$. These equations confirm that C only affects the transient behaviour, but not the final steady-state.

2.3 Timescales in the Earth system

Upper- and deep-ocean layers

The planetary thermal capacity sets the timescale to attain a steady-state. The Earth's global ocean is the energy reservoir of the system, as explained in chapter 1. However, the ocean stratification establishes two regimes in the storage. We have an ocean layer directly in contact with the atmosphere which is kept well-mixed by winds. We call both the atmosphere and this well-mixed layer the upper-ocean layer. Under the thermocline, we find a stratified ocean with a slow circulation. It is the deep-ocean layer. Circulation brings energy from the tropics to the high latitudes. High-latitude wind-driven upwelling brings cold water from the deep ocean that warms, absorbing the energy that came from the tropics. This water goes further into the high latitudes and again sinks into the deep ocean. This process transfers energy from the mixed to the deep-ocean layer and is the so-called deep-ocean heat uptake. It shall depend not only on the global mean surface temperature change but also on the changes in the global mean temperature of the deep ocean. Presumably, it is to first order a function of the difference between both temperature changes. If the global mean surface temperature changes more than the deep ocean temperature, net energy should flow into the deep ocean.

Thermal capacities

We can estimate the thermal capacities of the upper- and deep-ocean layers taking into account the dry air and the ocean water thermal capacities. We can also take into account the presence of water vapour and phase changes, as well as land's thermal capacity. The contributions to the Earth's thermal capacity, in terms of depths of layers of pure water, reveal that dry air contributes with $\sim 2\,m$. Water vapour with phase changes amount $\sim 1\,m$. In comparison, land only contributes $\sim 0.01\,m$, whereas the 75-metre-depth mixed layer (covering 75 % of the Earth's surface) contributes with $\sim 52\,m$. Thus, the upper-ocean layer thermal capacity is equivalent to a global layer of $\sim 55\,m$ of pure water. However, the largest thermal capacity in the Earth system is that of the 4000-metre-depth deep-ocean layer: $\sim 3000\,m$, two orders of magnitude larger than the upper-ocean layer. These estimates show why most of the TOA imbalance goes into the global ocean.

Timescales

With the thermal capacities presented above, we can roughly estimate the timescales in the Earth system. Thermal capacity determines how much energy is needed to change in one Kelvin the temperature. Thus, we need an estimate of how much energy per unit time is introduced per one Kelvin change. For the upper ocean, an estimate of this quantity is λ. In the case of the deep ocean, it is the rate at which the deep ocean uptakes heat from the upper ocean. We call this γ. Some model-based estimates are $\lambda \sim -1.3\,W\,m^{-2}\,K^{-1}$

and $\gamma \sim 0.7\,\mathrm{W\,m^{-2}\,K^{-1}}$ (Geoffroy et al. 2013a). Then the timescales are the ratios of the thermal capacities to the aforementioned rates. Thus, $\tau_u = C_u/|\lambda| = h_u(c_w/|\lambda|) \approx 6\,\mathrm{yr}$ and $\tau_d = C_d/|\gamma| = h_d(c_w/|\gamma|) \approx 570\,\mathrm{yr}$. In these rough estimates we consider that the layers are decoupled. The coupling extends the timescale of the upper ocean and reduces the deep ocean's. Regardless of the coupling, the upper ocean sets a decadal timescale, whereas the deep ocean provides a centennial timescale to the Earth system.

2.4 The two-layer model

Non-linearised two-layer model

The budget equation (2.1) describes the global energy cycle. However, in the previous section, we discussed the timescales set by the upper-ocean and deep-ocean layers, both connected by the deep-ocean heat uptake. Thus, we can rewrite the planetary budget equation (2.1) depending on two other budget equations corresponding to each one of the layers. Thus, the system of equations is:

$$\begin{array}{rcccccc} N & = & N_u & + & N_d & & \\ N_u = C_u\dot{T}_u & = & F & + & R & - & H \\ N_d = C_d\dot{T}_d & = & & & & & H \end{array} \tag{2.3}$$

In the system (2.3), there are three equations: first is the planetary energy budget. Second and third equations are the upper- and deep-ocean budgets, respectively. Each compartment has its own temperature change but T_u is equivalent to the global mean surface temperature change. The new term in these equations is H, the deep-ocean heat uptake. This term does not alter the planetary budget, which still is $N = F + R$, as can be seen by adding the expressions for N_u and N_d.

Equations with explicit pattern-effect

Coupled climate models show a non-linear relationship between TOA imbalance and global mean surface temperature change, which means that the climate feedback parameter λ is not constant, depending on the evolution of the system. Given that λ has been defined as a derivative evaluated at the neighbouring steady-state, the inconstancy of the climate feedback parameter possibly reveals that the linear approximation of the radiative response is overly coarse, the feedbacks depend on the actual state of the system, or some feedbacks depend on other state variables. Although one can argue non-linearity and state dependency for some feedbacks (Good et al. 2015; Gregory et al. 2015; Senior and Mitchell 2000; Voss and Mikolajewicz 2001; Colman and McAvaney 2009; Caballero and Huber 2013; Jonko et al. 2013; Block and Mauritsen 2013; Meraner et al. 2013), the non-linear relationship between TOA imbalance and global mean surface temperature in models has found an explanation in feedbacks that vary with other state variables: an evolving sea surface temperature pattern varies cloud feedback mainly (Zhou et al. 2016; Andrews et al. 2015). This spatial pattern is also related to the deep-ocean heat uptake (Held et al. 2010; Winton et al. 2010; Armour et al. 2013; Geoffroy et al. 2013b). Thus, R has a component that not only depends on global mean surface temperature change but the difference $T_u - T_d$. Let us call R^* the component that only depends on T_u, then $R - R^*$ is this component that depends on $T_u - T_d$. We conveniently reformulate it in terms of H because from the perspective of the upper-ocean $R - R^*$ can be seen as a modified deep-ocean heat uptake. If we use R^* in the equation of the upper ocean of the system

(2.3), we obtain that the deep-ocean heat uptake from the perspective of the upper ocean is $H^* = H - (R - R^*)$. The equations (2.3) with the explicit pattern-effect are

$$\begin{array}{lcccccc} N & = & N_u & + & N_d & & \\ N_u = C_u \dot{T}_u & = & F & + & R^* & - & H^* \\ N_d = C_d \dot{T}_d & = & & & & & H \end{array} \tag{2.4}$$

The planetary budget equation becomes $F + R^* - (H^* - H) = F + R$. Thus, the conservation of energy remains.

2.5 Linearised two-layer model

Form of heat uptake terms

Deep-ocean heat uptake does not have a precise mathematical expression. As we postulated above, energy transfer depends on the state of the upper- and deep-ocean layers. We linearise with $H(T_u, T_d) \sim H(0,0) + \gamma(T_u - T_d) + \ldots$, where γ is the rate at which the energy transfer happens when the difference $T_u - T_d$ changes. By construction $H(0,0) = 0$. Also, H^* should have a similar form, and the only modification is a prefactor to the γ coefficient. Thus, the linearised equations (2.4) are

$$\begin{array}{lcccccc} N & = & N_u & + & N_d & & \\ N_u = C_u \dot{T}_u & \approx & F & + & \lambda^* T_u & - & \varepsilon\gamma(T_u - T_d) \\ N_d = C_d \dot{T}_d & \approx & & & & & \gamma(T_u - T_d) \end{array} \tag{2.5}$$

where λ^* is the climate feedback parameter that only contains T_u-dependent feedbacks, γ is the heat uptake rate that has units of $\mathrm{W\,m^{-2}\,K^{-1}}$ and ε is the efficacy parameter that is a non-dimensional quantity. Henceforth, for the sake of simplicity, we will write λ instead of λ^*.

Transient behaviour and the pattern-effect

Explicitly, the pattern-effect term is $H - H^* = (1 - \varepsilon)\gamma(T_u - T_d)$. No pattern-effect means that the pattern-effect term vanishes for any state of the system. Thus, the pattern-effect only vanishes if $\varepsilon = 1$. During ECS-defining experiments in complex climate models, the pattern-effect increases the effective response of the system in the first decades. As the temperature anomaly gradient between upper- and deep-ocean layers becomes smaller in later decades, the pattern-effect becomes weaker. These arguments are in favour of an efficacy parameter greater than one. We shall expand on this in chapter 4, where we will discuss the role of clouds in the pattern-effect.

2.6 Zero-layer approximation and the instrumental record

Although the definition of ECS remains simple and formally coincides with the one obtained from equation (2.2), the introduction of two layers to include the upper- and deep-ocean timescales comes with the price of a non-trivial analytical solution of system (2.5). Indeed, TCR case is non-trivial, but we can use our knowledge on the two timescales in the Earth system, decouple the system and obtain simple and powerful expressions for TCR and ECS in terms of transient changes in global mean surface temperature.

Zero-layer assumptions

Let us assume that (i) $N_u \approx 0$ and (ii) $T_d \approx 0$ although $\dot{T}_d := \mathrm{d}T_d/\mathrm{d}t$ is not zero (if it were, then $N_d \approx 0$). These assumptions mean that the upper-ocean is close to a

steady-state, but that the deep ocean works as an infinite sink of energy. Forcing changes should be in timescales shorter than centennial of the deep-ocean but longer than the decadal of the upper-ocean. These are the zero-layer assumptions. If we apply them to the system (2.5), we obtain the following set of equations

$$\begin{array}{rcccccc} N & \approx & 0 & + & N_d & & \\ 0 & \approx & F & + & \lambda T_u & - & \varepsilon\gamma T_u \\ N_d & \approx & & & & & \gamma T_u \end{array} \tag{2.6}$$

These are the expressions of the zero-layer approximation. The planetary energy budget is approximately equal to the deep ocean's, which increases linearly with T_u. But the key point here is that the equations become diagnostic: forcing evolution completely determines temperature evolution: $T_u \approx -F/(\lambda - \varepsilon\gamma)$. From this simple expression, we can work out approximate expressions for TCR and ECS. Given that $F(t_{2x}) = F_{2x}$, then we immediatly obtain the following expression $TCR = T_u(t_{2x}) \approx -F_{2x}/(\lambda - \varepsilon\gamma)$. If we use this to substitute $\lambda - \varepsilon\gamma$ in the diagnostic equation, then we obtain $T_u \approx (F/F_{2x})TCR$ for any time t. Similarly, if we use the equation for N_d and the definition $ECS \approx -F_{2x}/\lambda$, we obtain $ECS \approx [F_{2x}/(F - \varepsilon N)]T_u$ for any time t.

Approximate ECS and TCR

With the above expressions, we can estimate TCR or ECS from slices in the instrumental record where we think that the zero-layer assumptions are valid. Let us take two times t_1 and t_2 in the historical period and assume that in both points the zero-layer assumptions are valid. Thus, in both points, $T_u(t_i) \approx (F(t_i)/F_{2x})TCR$. If we subtract both expressions $\Delta T_u = T_u(t_2) - T_u(t_1) \approx [(F(t_2) - F(t_1))/F_{2x}]TCR = (\Delta F/F_{2x})TCR$ or

TCR and ECS from the instrumental record

$$TCR \approx \frac{F_{2x}}{\Delta F}\Delta T_u \tag{2.7}$$

where ΔF and ΔT_u are the changes in the forcing and the global mean surface temperature between times t_1 and t_2. In an analogous manner, we obtain an expression for ECS

$$ECS \approx \frac{F_{2x}}{\Delta F - \varepsilon\Delta N}\Delta T_u \tag{2.8}$$

The expression (2.8) appears to be linear in ΔT_u, but ΔN also depends on ΔT_u. Thus, it is non-linear in ΔT_u. More important is that both expressions (2.7) and (2.8) clearly have the observed changes in forcing and imbalance in the denominators.

Apart from algebraic properties, the differences between equations (2.7) and (2.8) explain why the pattern effect should not affect calculations of TCR if the zero-layer approximation is valid. The estimation of ECS considers the instantaneous action of the deep-ocean heat uptake and the pattern-effect, whereas the TCR estimate is affected in equal proportion between the idealised experimental definition and the instrumental record. Most of the authors that inferred ECS using the zero-layer approximation also made another assumption: no pattern-effect ($\varepsilon = 1$). We show in chapter 3 that this additional assumption leads to low-biased estimates of ECS. We also show that the zero-layer assumption $N_u \approx 0$ leads to TCR being low-biased. Failure of this assumption means that the upper ocean has absorbed part of the forcing, and the inferred TCR should be higher.

ECS, TCR and pattern-effect

2.7 Complex modelling, observations and the conceptual framework

Complex modellin and instrumenta recor

As we have seen in these first chapters, the instrumental record poses several caveats for the estimation of TCR, ECS and, therefore, projections of the ongoing climate change. However, tools such as the complex Earth system models can help us in the task to overcome some of these problems. First, we can simulate the instrumental record. If we force models with reconstructed external forcing from the instrumental record, we can obtain the modelled realisations of the instrumental record.

Modeled vs observed

It is true that biases exist inside models —because of parameterisations and approximations. Nevertheless, if they work appropriately, we can test hypotheses about feedback mechanisms, their contributions to modelled TCR and ECS and their effects on the simulated instrumental record. Then we can compare with the instrumental record and determine the importance of a given process. Moreover, because models should comply with the theory presented above concerning the energy cycle, we can use multi-model ensembles to derive the relationship between modelled warming and either TCR or ECS (equations (2.7) and (2.8)).

Emergent constraints on TCR and ECS from post-1970s warming

Should we leave you? As trash treat you?
Alas, where is my home now? Can you tell?
You were our mother and we have failed.

Submitted to Nature Geoscience on 2 November 2018, accepted on 3 September 2019 and published online on 7 October 2019 (Jiménez-de-la-Cuesta and Mauritsen 2019). Here it is adapted not only the main matter, but the online methods section and the downloadable supplementary material.

Abstract

Future global warming is determined by both greenhouse gas emission pathways and Earth's transient- and equilibrium climate response to doubled atmospheric CO_2. Energy-balance inference from the instrumental record typically yields central estimates of the transient response around 1.3 K and the equilibrium response of 1.5-2.0 K which is at the lower end of those from contemporary climate models. Uncertainty arises primarily from poorly known aerosol-induced cooling since the early industrialisation and a temporary cooling induced by evolving sea surface temperature patterns. Here we present an emergent constraint on post-1970s warming, taking advantage of the weakly-varying aerosol cooling during this period. We derive a relationship between the transient response and the post-1970s warming in CMIP5 models. We thereby constrain, with the observations, the transient response to 1.67 K (1.17-2.16, 5th-95th percentile). This is a 20 percent increase relative to energy-balance inference stemming from previously neglected upper-ocean energy storage. For the equilibrium climate sensitivity, we obtain a best estimate of 2.83 K (1.72-4.12) contingent on the temporary pattern-effects exhibited by climate models. If the real world's surface temperature pattern-effects are substantially stronger, then the upper bound equilibrium sensitivity may be higher than found here.

3.1 Challenges estimating sensitivities

Definitions and challenges

Future global warming is determined by greenhouse gas emission pathways, and Earth's transient climate response (TCR) and equilibrium climate sensitivity (ECS) (Hawkins and Sutton 2009; Grose et al. 2018). ECS is the Earth's long-term sensitivity to a doubling of atmospheric CO_2 over pre-industrial levels. ECS can be estimated from periods spanning typically thousands of years in which the system can attain statistical stationarity. Some palæoclimates qualify for this task (Rohling et al. 2012). On the other hand, the estimation of the Earth's transient response to increasing forcing or TCR requires a highly resolved

period of gradual warming. This requirement restricts us to the instrumental record warming as the primary source of information. Unfortunately, the anthropogenic forcing since the pre-industrial times is poorly known (Otto et al. 2013; Mauritsen and Pincus 2017; Gregory et al. 2002; Lewis and Curry 2014) and the energy imbalance of the Earth, which mostly consists of the flow of energy into the deep oceans, is only well-observed in the 21st Century (Johnson et al. 2016). On top of these uncertainties, inhomogeneous sea surface temperature (SST) patterns, hereafter referred to as pattern-effects, can temporarily dampen the transient warming (Held et al. 2010; Winton et al. 2010), e.g. by inducing more low-level clouds (Zhou et al. 2016) and, thereby, permitting a larger true ECS than that inferred from the historical warming with the help of a simple energy balance framework(Armour 2017; Andrews et al. 2018). Thus, the disequilibrium of the Earth climate system during the instrumental record warming poses several major challenges in the determination of climate sensitivity. This study presents a method to overcome several of these challenges and identifies upper-ocean heat content as an essential factor low-biasing past estimates of TCR from the instrumental record.

Aerosol cooling uncertainty

A significant limitation of the studies that infer Earth's climate sensitivity from 20th Century warming is the poorly known anthropogenic radiative forcing (Otto et al. 2013; Mauritsen and Pincus 2017; Gregory et al. 2002; Lewis and Curry 2014). Whereas the forcing from increasing greenhouse gas concentrations is sufficiently certain, the anthropogenic aerosol-induced cooling is highly uncertain. This uncertainty leaves substantial room for interpretation of the instrumental record: if the aerosol cooling was strong, such that the total anthropogenic forcing is weak, Earth's climate sensitivity has to be large, or vice-versa (Kiehl 2007). The aerosol cooling, nevertheless, exhibited a rapid increase up until around 1970. Hereafter, air quality restrictions on pollutants resulted in an only slowly-changing global aerosol cooling (Smith et al. 2011; Stevens 2015; Fiedler et al. 2017). Thus, focusing on this shorter period, though offering less warming signal than the full record, could offer a period with stronger total anthropogenic forcing and potentially overcome the aerosol uncertainty problem (Otto et al. 2013; Gregory and Forster 2008; Bengtsson and Schwartz 2013).

3.2 Constraining TCR

Emergent constraint on TCR

We indeed find a tight linear relationship between climate models' warming over the post-1970s period and their TCR, with a near-zero offset (Figure 3.1a, Table S3.4). We evaluate the statistical significance of the relationship with a leave-one-out method which indicates that the slopes and offsets obtained are not depending strongly on specific models (Methods). The statistical relationship is in line with the theoretical expectation that the historical warming is proportional to TCR (Methods). In contrast, no such proportionality of the centennial warming to TCR is found, presumably due to inter-model spread in aerosol cooling on this timescale (Forster et al. 2013). We use the identified relationship as an emergent constraint to infer TCR from the well known post-1970s temperature record, whereby the observed warming (ΔT_u) is projected on TCR via the emergent constraint slope (s) and the small offset (e) such that $TCR = s\,\Delta T_u + e$. Uncertainty in the three terms is propagated to a combined uncertainty in TCR using Monte-Carlo sampling (Methods).

TCR expected value and distribution

This straightforward technique gives us a median TCR of 1.67 K (Figure 3.2, Table

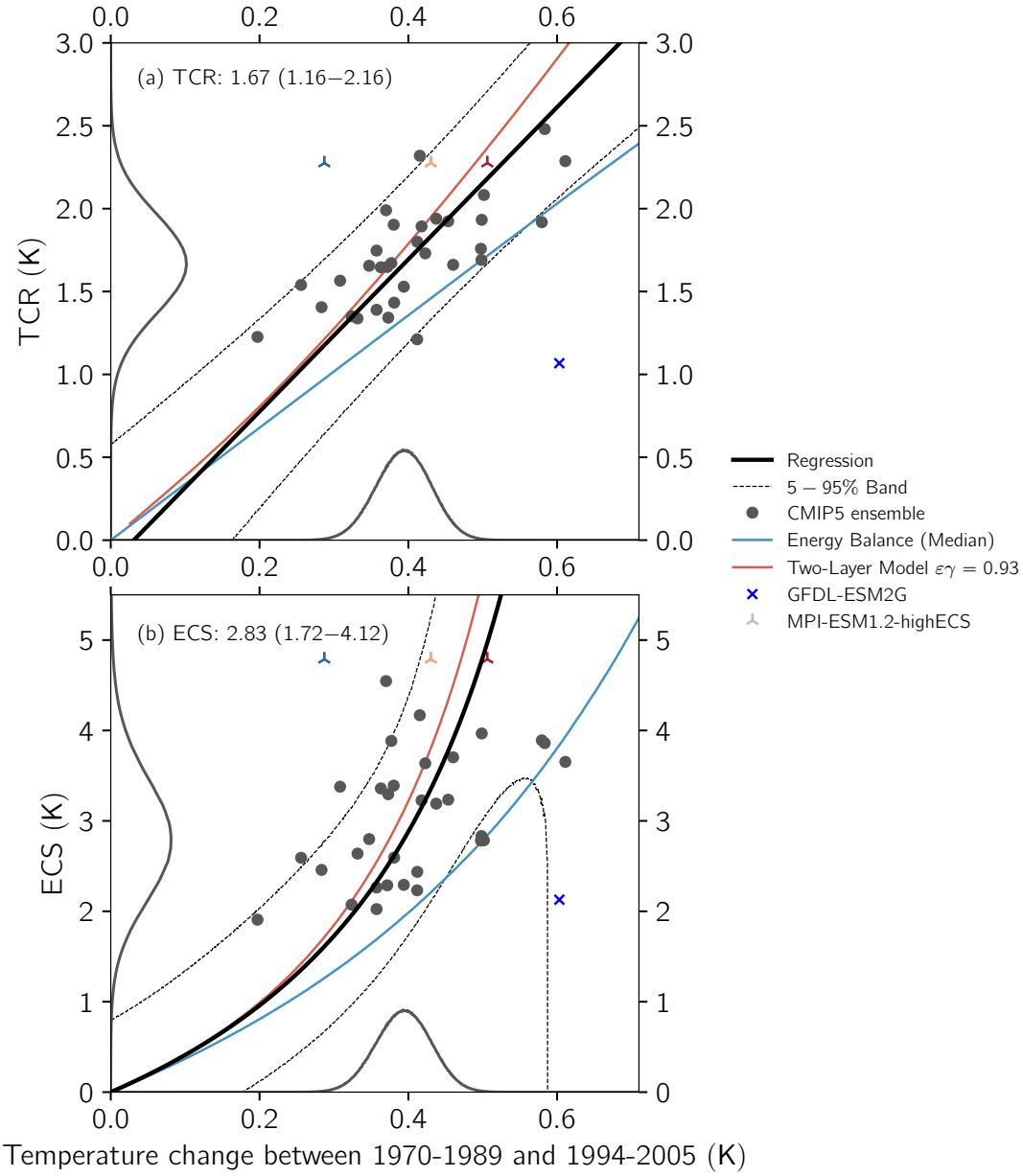

Figure 3.1: Emergent constraints based on the 1970-2005 warming on (a) TCR and (b) ECS. Thin lines show inference using energy balance (blue) and the two-layer model (orange) frameworks, whereas the thick black line shows the relationship found in the CMIP5 ensemble (grey dots, Table S3.2) fitted using orthogonal distance regression (Methods). Each dot is an ensemble mean over all available realisations of the historical experiment. The MPI-ESM1.2-highECS and GFDL-ESM2G models were not used in the regression. The dashed line is the 5-95 percent statistical prediction band for the regression. The probability distribution on the x-axis is based on the average of five data sets and an estimate of systematic error plus natural variability found in a large model ensemble. The observational distribution is mapped via the fitted relationship to obtain the probability of TCR and ECS as shown on the y-axes. Stated estimates are median and 5-95th percentiles.

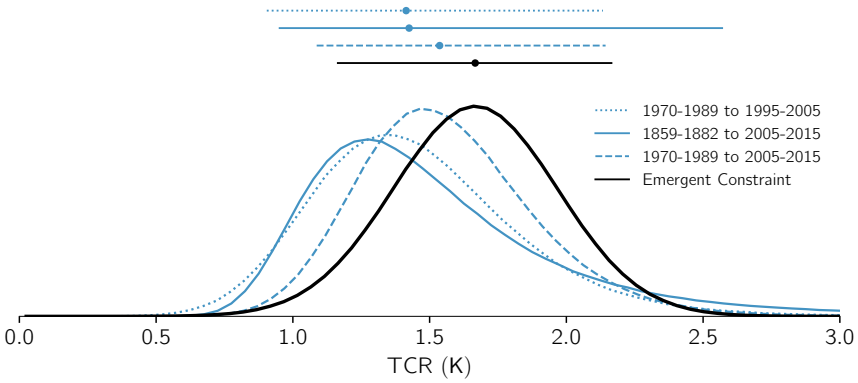

Figure 3.2: Probability distributions of TCR: the here derived emergent constraint is shown in black and energy balance estimates based on observations in blue. Horizontal lines show the median and the 5-95th percentile range.

S3.5). This median is roughly 20 percent higher than the energy-balance inferred values for the post-1970s warming period (1.41 K), the later period 1970-1989 to 2005-2015 (1.54 K) and the centennial warming (1.42 K). Moreover, the emergent constraint places considerably less likelihood on lower TCRs than any of the energy-balance estimates (Figure 3.2), e.g. the probability of TCR being below 1 K decreases from 2.2-9.6 percent to a merely 1.5 percent (Table S3.5). The centennial warming inference gives a 5.6 percent probability that TCR exceeds 2.5 K, whereas both the emergent constraint and energy-balance inference based on post-1970s warming place near-zero probability at such large TCR: chiefly a consequence of the tighter constraint on aerosol cooling for the post-1970s period. If we vary in a reasonable range the assumed natural temperature variability on the post-1970s warming, the uncertainty in the TCR estimate varies scanty and, instead, it is dominated by the relationship coefficients.

Aerosol forcing uncertainty do not increse median TCR

The larger median TCR found with the emergent constraint could either be caused by a stronger aerosol cooling increase in models during the post-1970s or by the underlying assumptions of energy-balance inference. It turns out that aerosol forcing is an unlikely candidate. For instance, the MPI-ESM1.1 model show larger $TCR/\Delta T_u$ ratios than assumed in energy-balance inference, despite the fact that it has a weaker increase in aerosol cooling (Mauritsen et al. 2019). This behaviour is consistent with aerosol-forcing uncertainty not being a dominant source of uncertainty on post-1970s warming. Furthermore, since a majority of models have weaker TCR to post-1970s warming than MPI-ESM1.1, a strong aerosol cooling in CMIP5 models, in general, is not a viable explanation for the higher TCR obtained using the emergent constraint compared to energy balance.

Physical grounds for the larger TCR

Instead, we find a plausible physical explanation for the larger median TCR. Energy-balance inference of TCR relies on the zero-layer assumption, wherein the heat capacity of the upper ocean is neglected (Methods). This assumption is only valid if the forcing increases gradually over multiple decades and the increase is slow enough that the upper ocean, atmosphere and land are approximately in equilibrium. Until the equilibrium between these components is attained, the system warms less than expected from the zero-layer

approximation since part of the energy is stored in the upper ocean (Gregory et al. 2015). For instance, this happens when the forcing rapidly changes, e.g. in the cooling arising from explosive volcanic eruptions (Gregory et al. 2016). In the historical record, the bulk of the warming occurred over just a few decades since the 1970s and, therefore, the validity of the zero-layer assumption is questionable. Indeed, if we relax this assumption and use the two-layer model instead (see Methods), we obtain a slope indistinguishable from that obtained with the emergent constraint based on complex climate models. Thus, it is plausible that the zero-layer assumption has low-biased previous inferences (Otto et al. 2013; Mauritsen and Pincus 2017; Lewis and Curry 2014) of TCR from the instrumental record.

Exploring natural variability

Low-frequency natural variability in global mean temperature can introduce a non-forced signal in the instrumental record. The non-forced signal is typically handled by the selection of two periods with similar states of natural variability, for instance, related to El Niño and the Atlantic multidecadal oscillation (AMO) (Lewis and Curry 2014). A challenge with the post-1970s period is that the AMO index shifted from negative to positive, leading to a possible contribution of natural variability to global warming. We find, however, model-based evidence that the shift is forced: across most models the positive shift in AMO occurs in the historical simulations, even when subtracting the contribution from global warming which can be done on large ensembles (Methods, Figure S3.4). Hence, we do not compensate for AMO change in this study, but remark that a blind compensation for an assumed unforced AMO would lead to both a reduction of the observed ΔT_u and a change in the emergent constraint (Table S3.7), which means a merely 10 percent reduction of the median TCR (Figures S3a, S5 and Table S3.8).

Challenging the lower-bound TCR

Out-of-range TCR would be possible if post-1970s aerosol cooling change deviates considerably from the IPCC AR5 best estimate of -0.15 Wm^{-2} (Table S3.3). Even though the precursor emissions stagnated (Smith et al. 2011), an argument for a weakly strengthening aerosol cooling is the geographical shift in the emissions from the North Atlantic towards East Asia and other tropical regions. As the relationship between aerosol concentrations and reflected sunlight is logarithmic, the geographic shift distributes the same amount of aerosols in a larger and more sunny region, leading to a strengthened aerosol cooling. The described behaviour is in line with a majority of models (Shindell et al. 2011). Thus, a constant or weakening aerosol cooling change would allow a lower TCR to match post-1970s warming, as some models show (Regayre et al. 2014; Zhao et al. 2018). If the aerosol cooling best estimate would be zero, the energy-balance inferred median TCR reduces by 12 percent.

Challenging the upper-bound TCR

We now challenge the upper bound on TCR by constructing a version of the MPI-ESM1.2 model with strong positive cloud feedbacks resulting in high-end TCR of 2.3 K and ECS of 4.8 K (Figure 3.1, Methods). A new feature of the MPI-ESM1.2 model over the predecessor MPI-ESM1.1 is the representation of aerosol-cloud interactions as a parameterised Twomey-effect (Fiedler et al. 2017; Mauritsen et al. 2019). With an unaltered total aerosol forcing of around -0.6 Wm^{-2} relative to pre-industrial, the model clearly warms more than observed from 1960 onward (Figure 3.3). With an enhanced total aerosol cooling of -1.2 Wm^{-2} both centennial and post-1970s warming agrees with observations (Figures 3.1 and 3.3). However, for a long period between 1940 and 2000, the model is on average colder than observed. Further enhancement of the aerosol cooling leads

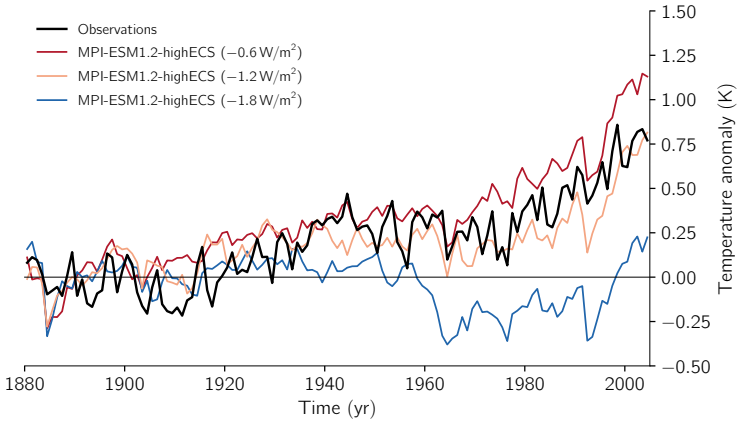

Figure 3.3: Comparison of the MPI-ESM-1.2-highECS model to observations. The curves show the instrumental temperature record and model runs with different aerosol-cooling strengths. The model was run four times with each aerosol setting, and the ensemble mean is displayed.

to a negative total forcing starting in the 1960s, leading to inconsistency with observed warming during that period. Thus, larger TCR than indicated by the emergent constraint, paired with stronger aerosol cooling, yields an implausible historical temperature evolution.

3.3 Constraining ECS

Emergent constraint on ECS

We now explore if post-1970s warming can constrain ECS. For constraining ECS from non-equilibrium states, we need information on deep-ocean heat uptake (Hansen et al. 1985) and pattern-effects. Energy-balance inference of ECS usually does not consider the pattern-effects that can temporarily dampen the warming (Armour 2017; Andrews et al. 2018). We assume that the form of the relationship between warming and ECS is $ECS = \Delta T_u/(s' - e'\Delta T_u)$, where the parameter s' is related to post-1970s forcing and e' represents the combined damping by the deep-ocean heat uptake and pattern-effects (Methods, Table S3.4). Using the same methods as with the TCR case, we find a median ECS of 2.83 K, which is 20-30 percent above the energy-balance inferred value (Figures 3.1 and 3.4, Table S3.6). Whereas the probability for ECS exceeding 4.5 K is similar to energy-balance estimates, the likelihood of an ECS below 1.5 K is reduced from 4-23 to only 2.4 percent (Table S3.6). An earlier study (Armour 2017) used idealised runs with CMIP5 models to correct the energy-balance inferred ECS from centennial warming and obtained an ECS of 2.9 K (1.7-7.1). Our estimate is consistent with this result and our considerably smaller upper bound can be ascribed to a less uncertain aerosol cooling change during the post-1970s era.

Explaining the shift to higher ECSs

The higher median ECS arise primarily from the pattern-effects that temporarily buffer the warming (Armour 2017). Pattern-effects are represented in the two-layer framework as the deep-ocean heat uptake efficacy ε. From climate models (Geoffroy et al. 2013b), ε is 1.28 (range: 0.83-1.82) and the deep-ocean heat uptake coefficient γ is 0.73 $Wm^{-2}K^{-1}$ (0.5-1.16). The product $\varepsilon\gamma$ (0.93 $Wm^{-2}K^{-1}$) controls the relationship between transient and equilibrium warming as can be shown. We run the two-layer model. Running the

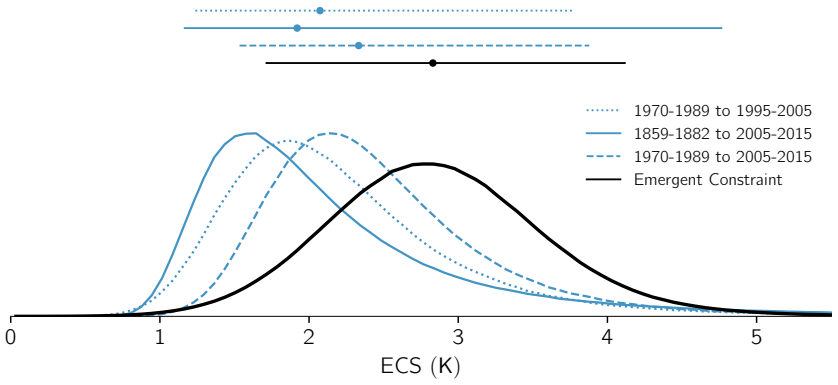

Figure 3.4: Probability distributions of ECS, otherwise as Figure 3.2.

two-layer model with the model mean value of the $\varepsilon\gamma$ delivers a striking similarity to the emergent constraint relationship (Figure 3.1). If we introduce the uncertainty on $\varepsilon\gamma$, the resulting relationships encompass almost all CMIP5 models (Figure 3.5b) and potentially explain much of the inter-model spread. The reader should note that $\varepsilon\gamma$ has no impact on the emergent constraint of TCR (Figure 3.5a) because both transient historical warming and TCR are affected in equal proportion by $\varepsilon\gamma$. This independence of TCR to pattern-effects further corroborates our main finding: the difference between the TCR from the emergent constraint and energy-balance inference is primarily due to upper-ocean warming.

3.4 Summary

Taking into account the disequilibrium of the Earth system —including that of the upper ocean— is crucial to inferring climate sensitivities from the instrumental record. Foremost, the oceans buffer anthropogenic warming for centuries by both sequestering most of the trapped energy into the deep ocean and through a pattern of sea surface temperature that enables the atmosphere to radiate more efficiently to space. If pattern-effects of the Earth are stronger than that indicated by models, as recently suggested in a study (Andrews et al. 2018), then higher ECS than that found by our emergent constraint cannot be ruled out. Hence, low ECS values would be even less likely than found here and by Armour (2017). Finally, the here-gained insight that the often-neglected upper ocean dampens transient warming and, consequently, impacts inferred TCR, has particular value since the instrumental record is practically the only period with sufficient temporal resolution to estimate Earth's TCR, and thus justifies an upward revision of the central estimate and the tightening range of uncertainty.

3.5 Methods

3.5.1 Observational data, model output and radiative forcing

Temperature datasets

We use observations of global mean surface temperature from five different datasets:

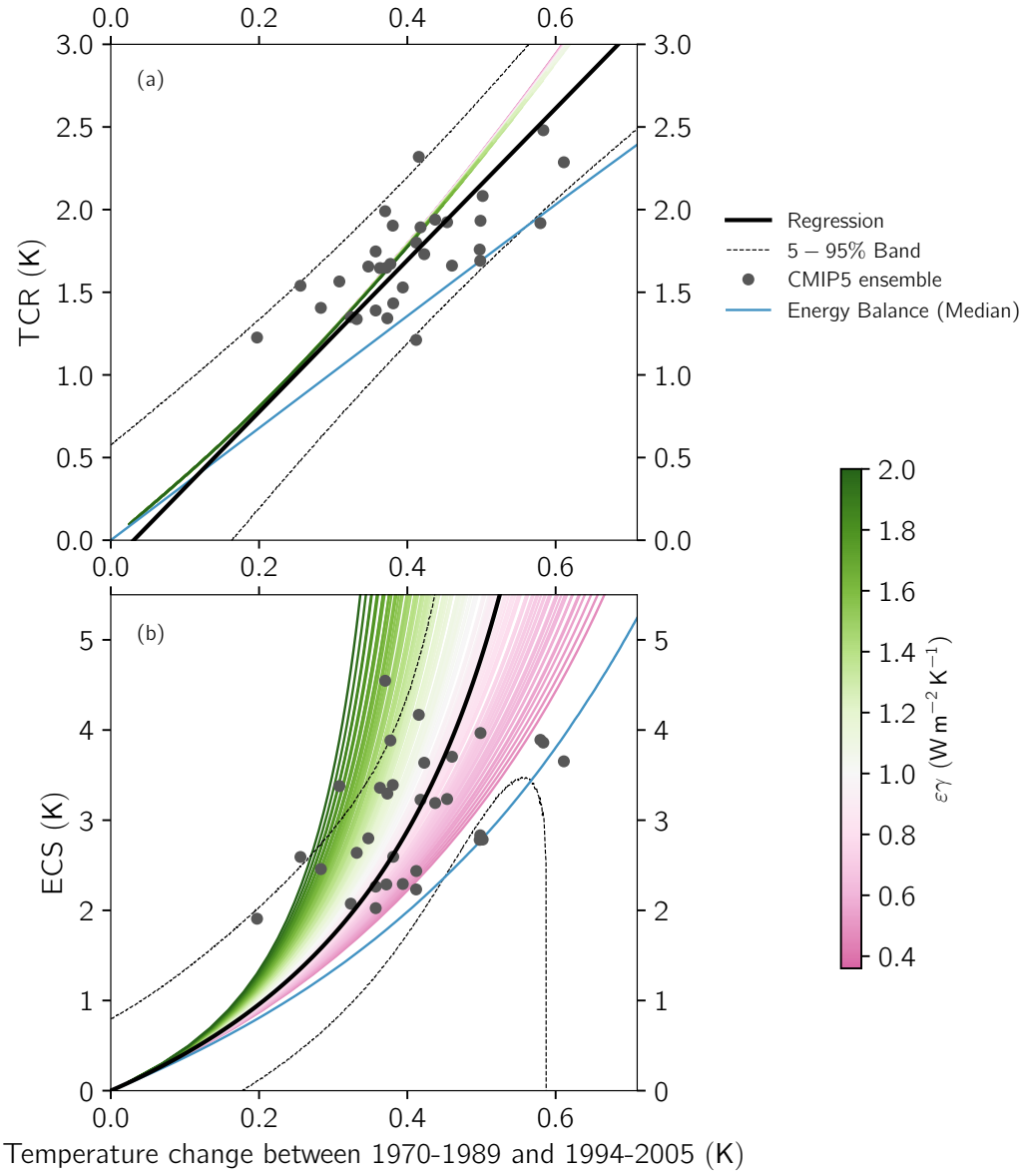

Figure 3.5: Exploration of the impact of pattern-effects, as represented by the product $\varepsilon\gamma$ (Methods), on the relationship between post-1970s warming on a) TCR and b) ECS. A range of values of pattern-effects is shown as shaded from magenta to green. Note that these curves mostly overlap for the case of TCR (panel a).

HadCRUT4.6 (Morice et al. 2012), NOAA GlobalTemp (Vose et al. 2012) (known before as MLOST, gridded version obtained from NOAA/OAR/ESRL PSD web site), GISTEMP (Hansen et al. 2010) (gridded version obtained from NOAA/OAR/ESRL PSD web site), Berkeley (Rohde et al. 2013), and Cowtan and Way 2.0 dataset (Cowtan and Way 2014). Some of these datasets take different approaches to extrapolate to un-observed regions, where possibly regional warming has been faster than globally. However, there is not much difference between their post-1970s warming (Table S3.1), and in fact, the dataset with the strongest warming (HadCRUT4.6) does not apply extrapolation so observational coverage is probably a minor issue over this period. Although the datasets agree closely, we choose to average and use the spread as an estimate of structural uncertainty. Uncertainty from natural variability is determined from a 100-member ensemble of historical climate model simulations using the MPI-ESM1.1 model, and this dominates over structural uncertainty. In practice, we generate five gaussians centred at the mean values from the temperature datasets, and randomly sample these distributions to construct a joint distribution that integrates not only the differences in the datasets but also the internal variability estimate.

Climate model output

Climate model output from CMIP5 models listed in Table S3.2 were obtained through the Earth System Grid Federation nodes. Here control experiments with constant pre-industrial boundary conditions (`piControl`), historical boundary conditions for 1850-2005 (`historical`), gradually increasing CO_2 at a rate of 1 percent per year (`1pctCO2`) and with abruptly quadrupled CO_2 (`abrupt4xCO2`) were downloaded in as many realisations as were available. The results were averaged when multiple realisations were available (see Table S3.2).

Surface vs. two-meter temperatures

To compare models and observations, we use surface temperature instead of surface air temperature. This is because the oceans cover 70 percent of the Earth's surface most of the observations used to estimate global temperature change are actually surface temperatures, not surface air temperatures as is observed on land. Furthermore, surface air temperature in models is a diagnosed quantity, and unlike surface temperature without direct influence on the results, e.g. the radiative response. Models indicate that the difference in global mean change between these is approximately 6 percent, and thus if ECS and TCR in terms of surface air temperature are sought then the results found here should be adjusted slightly upward. Since about 30 percent of the observed temperatures are already surface air temperatures, the upward adjustment should be about 4 percent.

Methodology for modelled TCR and ECS

We calculate TCR and ECS from anomalies of the surface temperature in the `1pctCO2` and `abrupt4xCO2` simulations by first subtracting the longterm mean from `piControl`. TCR as the mean temperature in a 20-year period around year 70 of the `1pctCO2` experiment when CO_2 is doubled. ECS is calculated using the de-facto standard method of a linear regression of planetary imbalance over surface temperature change of the first 150 years of the `abrupt4xCO2` experiment (Andrews et al. 2012). The temperature change in the post-1970s period is taken as the difference of the mean surface temperature anomaly in 1970-1989 to the mean temperature anomaly in 1994-2005. We chose to have the 5-year gap to reduce the influence of the Mt. Pinatubo volcanic eruption.

About the approximation on ECS

We must remark that the aforementioned definition of ECS is only an approximation. Only the steady-state of a `abrupt2xCO2` would provide the true value of ECS. The approximation underestimates the true ECS because the pattern-effect tends to enhance the warming at the end of the abrupt forcing runs. On the other hand, since the forcing does

not precisely scale in a logarithmic fashion and the water vapour feedback is stronger in a warmer climate, our estimate of ECS is larger than the one derived from the `abrupt2xCO2` experiments. In summary, pattern-effect and larger response work in opposite directions and cancel out roughly (Maria Rugenstein, personal communication).

Model exclusion

The GFDL-ESM2G model was excluded from the calculation of the regressions since it was well outside the 5-95 percentile prediction band: The GFDL-ESM2G model's `historical` simulation shows large post-1970s warming, even though its TCR is the lowest found among models. Given that we have only one realisation for this model (Table S3.2), that the closely related GFDL-ESM2M model which differ only in its ocean component is in line with the behaviour of other models, and that the aerosol forcing cannot explain the result (Ming Zhao, personal communication), we consider that this outlying behaviour is due to the model's internal variability expressing itself in this single realisation. The evolution of the historical run depends on the point of the pre-industrial control used as the initial condition. There are fluctuations in this base state (unforced variability), that may change the warming in the period. As the model had only one run, that can be affected by the initial conditions, and the warming was more substantial than what the climate responses suggested, we excluded the model. In support of this last point, GFDL-ESM2G shows a warming of 0.60 K with a TCR of 1.07 and an ECS of 2.13. For instance, CANESM2 (5 ensemble members) has a warming of 0.61 K with a TCR of 2.29 K and an ECS of 3.65 K, which are higher climate responses for the same warming. Moreover, GFDL-ESM2M with one realisation has a warming of 0.41 K with a TCR of 1.21 K and an ECS of 2.23 K; or FGOALS-G2 also has lower warming of 0.37 K with a TCR of 1.34 K and an ECS of 3.29 K (See Table S3.2).

Radiative forcing data

Whereas the emergent constraint relies only on the global mean surface temperature change, the interpretive energy-balance framework and the two-layer model integration, as will be described below, requires in addition radiative forcing. We take the forcing from greenhouse gases, aerosols, ozone, stratospheric water vapour, land use, contrails, solar variability, and black carbon on snow from Annex II of the Intergovernmental Panel on Climate Change (IPCC) Fifth Assessment (IPCC 2013a). The forcing from a doubling of atmospheric CO_2, F_{2x} is set to 3.71 Wm^{-2}, which is consistent with the tabulated forcing. Uncertainty in each component, except post-1970s aerosol forcing and greenhouse gas forcing, is taken from Ref. Mauritsen and Pincus 2017, which is based on the IPCC assessment report. Uncertainty in post-1970s aerosol forcing is assessed to be small and is modelled as a gaussian with a standard deviation of 0.1 Wm^{-2}, allowing a 7 percent probability of a weakening post-1970s aerosol cooling. Uncertainty in the well-mixed greenhouse gas forcings are assumed relative to the forcing strength and are therefore reduced for the post-1970s periods. Forcing changes and assumed uncertainties are tabulated in Table S3.3 for the three different periods.

3.5.2 Emergent-constraint regression model

The regression model used in the emergent constraint on post-1970s global warming is derived from the the energy-balance framework. To do so we notice that we can substitute back $\Delta N \approx \gamma \Delta T$ and perform a coordinate transformation such that expressions purely in

terms of the temperature evolution are obtained:

$$TCR = s\Delta T + e \tag{3.1}$$

$$ECS = \frac{\Delta T}{s' - e'\Delta T} \tag{3.2}$$

where $s = F_{2x}/\Delta F$, $s' = \Delta F/F_{2x}$ and $e' = \varepsilon\gamma/F_{2x}$. Additionally, we introduce an off-set in Equation (3.1) which should be indistinguishable from zero and can be considered a test whether sufficient information is contained in the CMIP5 model ensemble.

We apply Orthogonal Distance Regression (ODR) that considers uncertainty in the independent variable (Boggs et al. 1987) to fit the theoretically derived models that link post-1970s warming to TCR and ECS, Equations (3.1) and (3.2). Equal weighting of each model is applied. Models that supply only one or a few ensemble members will induce uncertainty in the regression that is due to natural variability, which inflates the estimates of uncertainty in TCR and ECS as we also account for natural variability in the distribution of observed post-1970s warming. Nevertheless, we deem this is a minor effect as most models supply multiple ensemble members (Table S3.2). We perform the regression on the set of model ensemble means.

We take a Monte-Carlo approach to estimate the uncertainty in TCR and ECS from the emergent constraints. With the results of the regression algorithm, we generate a joint distribution of the parameters and the error in the estimation, taking into account the covariance of the parameters. We draw random samples of parameters from this distribution to generate the distribution of the prediction uncertainty, which is the 5-95 percentile range around regression curves, as shown in Figure 3.1. We generate a joint distribution of parameters, error in estimation and the observed temperature change in the post-1970s, draw random samples and calculate with them the corresponding TCRs and ECSs. These sets of TCRs and ECSs form the predicted distributions for TCR and ECS, and from them, we obtain the 5th, 50th (median) and 95th percentiles (Tables S5 and S6).

3.5.3 Statistical measure of the robustness

We use one metric that can show the statistical goodness-of-fit. The metric is a jackknife. It consists of the calculation of a set of regressions where we leave out one of the data points. For both TCR and ECS, the results for the jackknife (Figure S3.1) show that all the jackknife regressions are close to the respective regressions based on all models. Thus, we show that the derived relationships are statistically robust and support the physical significance of the results, which are the actual finding. Moreover, for both TCR and ECS, in Figure S3.2, we show that the distributions derived from the jackknife regressions are not appreciably broader than the distributions derived from the regressions based on all models. The median values are also not far from the median from the full regressions.

3.5.4 Experiments with MPI-ESM1.2-highECS

To explore the upper bound of the constrained ECS and TCR, we modified the Max-Planck-Institut MPI-ESM1.2 coupled model to have stronger positive cloud feedbacks. Foremost, the modifications alter the mixing rate between lower and middle troposphere, a feature

that can explain half of the variance of ECS in the CMIP5 ensemble (Sherwood et al. 2014; Brient et al. 2016). The shallow mixing dries the lower troposphere by exporting the moisture out of the boundary layer. The mixing rate increases with warming and how it increases depends on the initial mixing rate. Thus, as the Earth warms, a higher initial mixing ratio dries the boundary layer and promotes a decrease in the shallow clouds, resulting in a positive cloud feedback. To do so, we increased the shallow mixing by reducing the lateral entrainment rate in the shallow convective parameterisation. To enhance shallow clouds in the base state, such that they can contribute to cloud feedback, the critical relative humidity profile was altered. Further, the negative mixed-phase cloud feedback dominant at mid- to high latitudes were weakened by enhancing a cloud ice concentration threshold for the fast conversion from cloud liquid to cloud ice. Finally, to explore the influence of uncertainty in aerosol cooling, we modify the parameterisation of aerosol-cloud induced forcing. In MPI-ESM1.2 the aerosol forcing is parameterised using a Twomey effect which is sensitive to the assumed background cloud condensation nuclei concentration (Fiedler et al. 2017; Stevens et al. 2017). To obtain a stronger aerosol cooling, we reduce the assumed background concentration by a factor of ten to hundred. The stronger cooling is considered a surrogate for non-Twomey aerosol-cloud interactions not represented by the model.

3.5.5 Internal variability: the AMO–IPO correction

We calculate SST indices for the major modes of variability, the AMO,Niño 3.4 and IPO, for each of the experiments the CMIP5 models following. We obtain the monthly and the corresponding yearly time series. Using the results from `piControl` experiments, we find for each model an empirical linear relationship between SST index and GMST in an equilibrium state. We select one of the Pacific Ocean modes and the AMO and regress GMST over them using the model

$$\mathrm{T}_{\texttt{piControl}} = \beta_0 + \beta_1 \mathrm{AMO}_{\texttt{piControl}} + \beta_2 \mathrm{SPI}_{\texttt{piControl}}$$

where SPI is either Niño 3.4 or IPO. With the coefficients β_i obtained from the regressions, in principle, we can correct the other experiments (`1pctCO2`,`abrupt4xCO2` and `historical`) for the influence of these internal variability patterns using indices values for each experiment

$$\mathrm{T}_{\mathrm{corr}} = \mathrm{T} - \beta_0 - \beta_1 \mathrm{AMO} - \beta_2 \mathrm{SPI} \tag{3.3}$$

To have a standard for the corrections, instead of using each model coefficients, we compute the correction with the coefficients obtained for the MPI-ESM1.1 100-member ensemble. Most of the coefficients for the other models are similar in magnitude to those of MPI-ESM1.1 (Table S3.11). Because the index of the IPO includes northern, southern and equatorial zones of the Pacific basin, we consider SPI = IPO, although the coefficients with Niño 3.4 are similar. Table S3.10 is analogous to Table S3.2, but using the corrections. When a comparison between tables is made, it is evident that TCR and ECS differences are small, but ΔT differences are large. This suggests that historical forcing projects on these modes of variability, meaning they are partly forced.

From gridded datasets of the observations, we can also calculate the indices and apply the correction to obtain a corrected time series of the GMST. Corrected temperature

datasets now can be used to repeat the analyses. A summary of the corrections for the observations is given in Table S3.1.

Data Availability CMIP5 data can be accessed through ESGF nodes. HadCRUT4 data is provided by the UK Met Office Hadley Centre. NOAA/OAR/ESRL PSD dataset website provided the NOAA GlobalTemp dataset as well as the GISTEMP dataset. BEST was downloaded from the Berkeley Earth website. Cowtan and Way 2.0 dataset is provided from the authors website. Forcing data comes from the IPCC AR5 WG1 report.

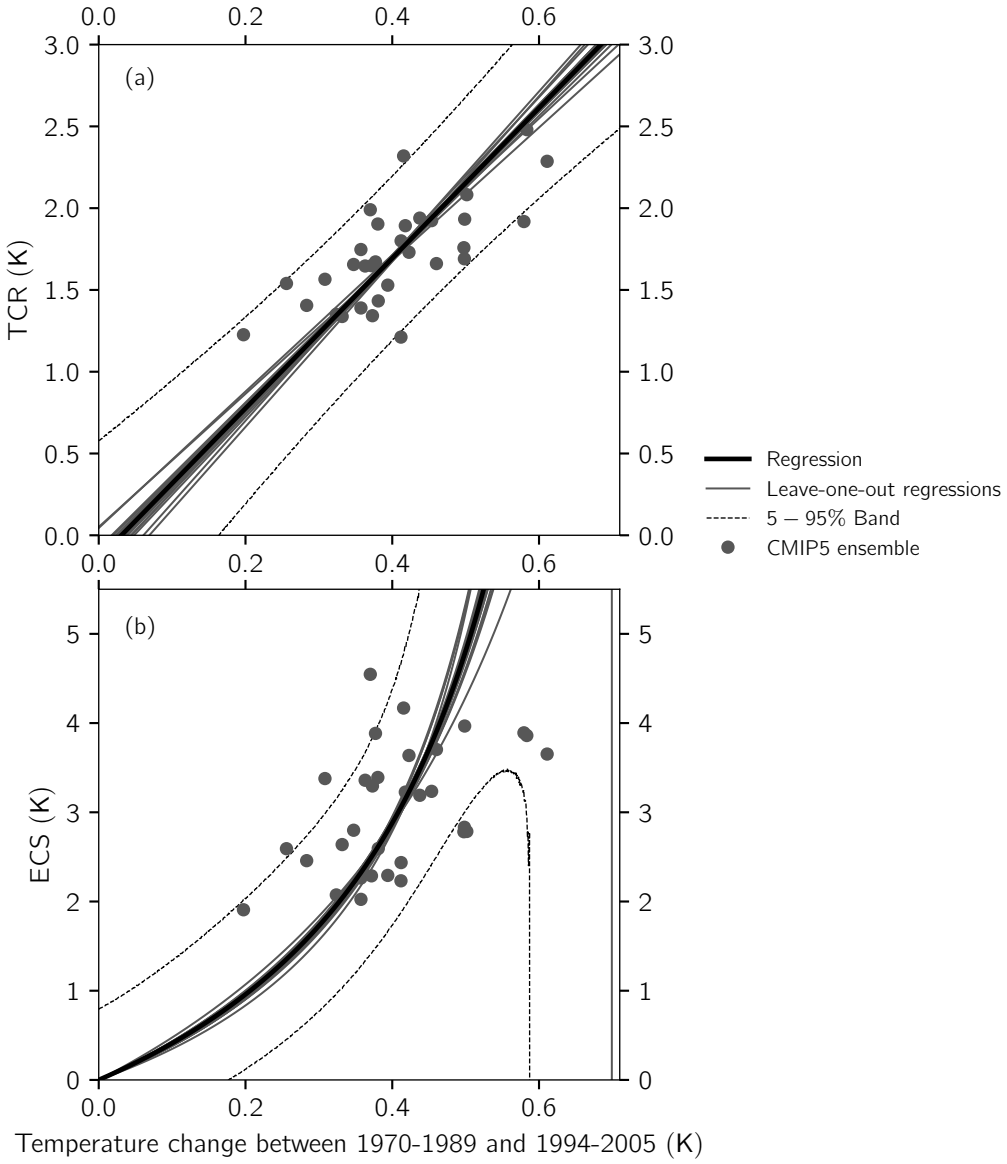

Figure S3.1: Jackknife or Leave-one-out regressions for (a) TCR and (b) ECS. Grey lines are the regressions leaving out each one of the grey dots that are CMIP5 ensemble members (means for each model). The heavy black line is the regression using all the grey dots. Dotted lines show the 5-95 percentile region of the black line regression.

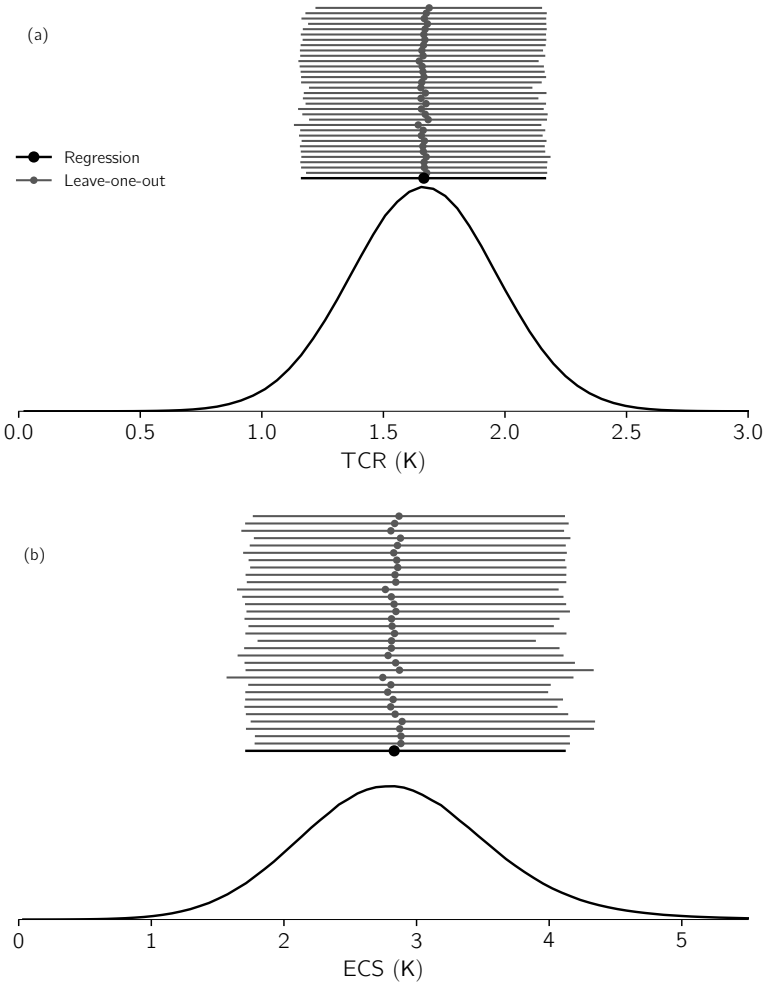

Figure S3.2: Jackknife or Leave-one-out distribution estimates for (a) TCR and (b) ECS. Grey lines show the 5-95 percentile range of the Jackknife-derived PDFs for TCR and ECS. The grey dots represent the position of the median value of the distributions. Black heavy lines show the same range and the actual distribution obtained from the full regressions.

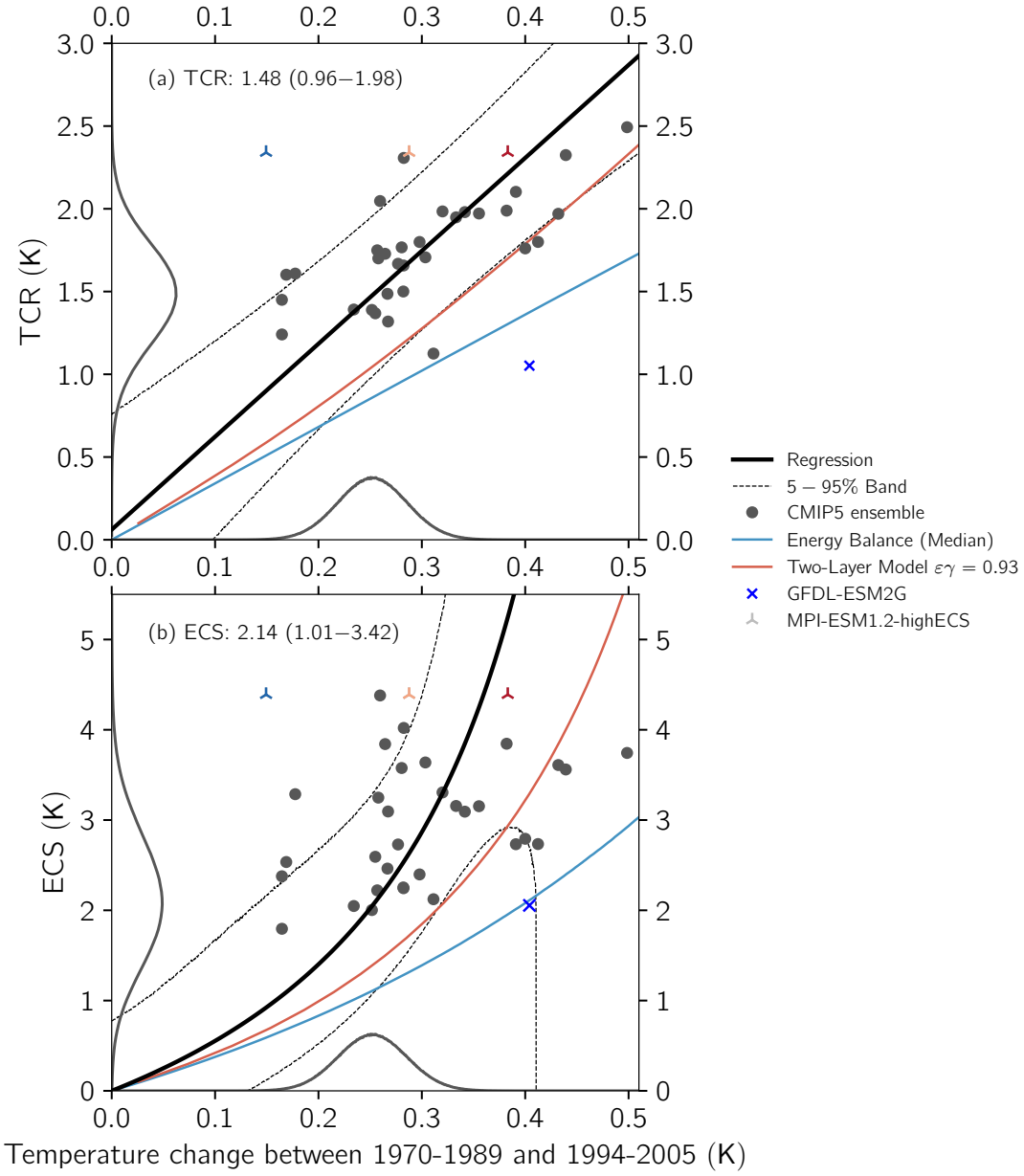

Figure S3.3: Regression results **with a correction for AMO–IPO modes of SST variability**. (a) TCR and 1970-2005 warming and (b) the corresponding results for ECS. Thin lines show reference estimates using usual energy balance (blue) and the two-layer model (orange) frameworks, whereas the heavy black line shows the corresponding functional relationship found in the CMIP5 ensemble (grey dots, Table S3.10).

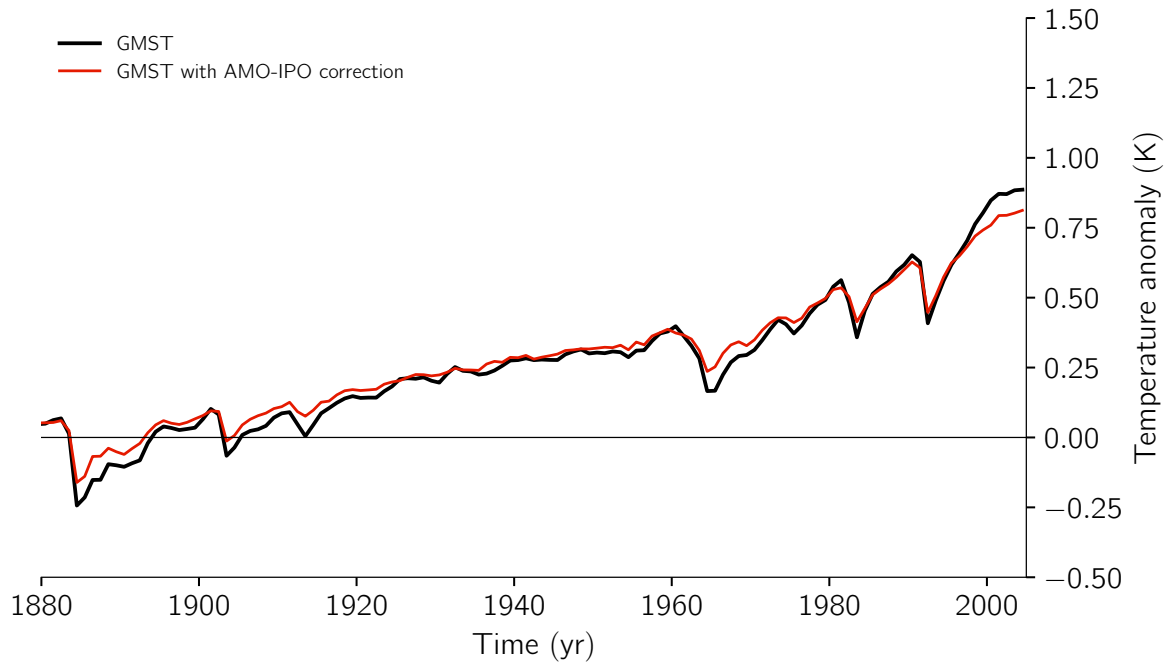

Figure S3.4: **AMO–IPO correction** in the MPI-ESM1.1. Here is shown the mean time series of the 100 `historical` runs without correction (black) and with correction (red).

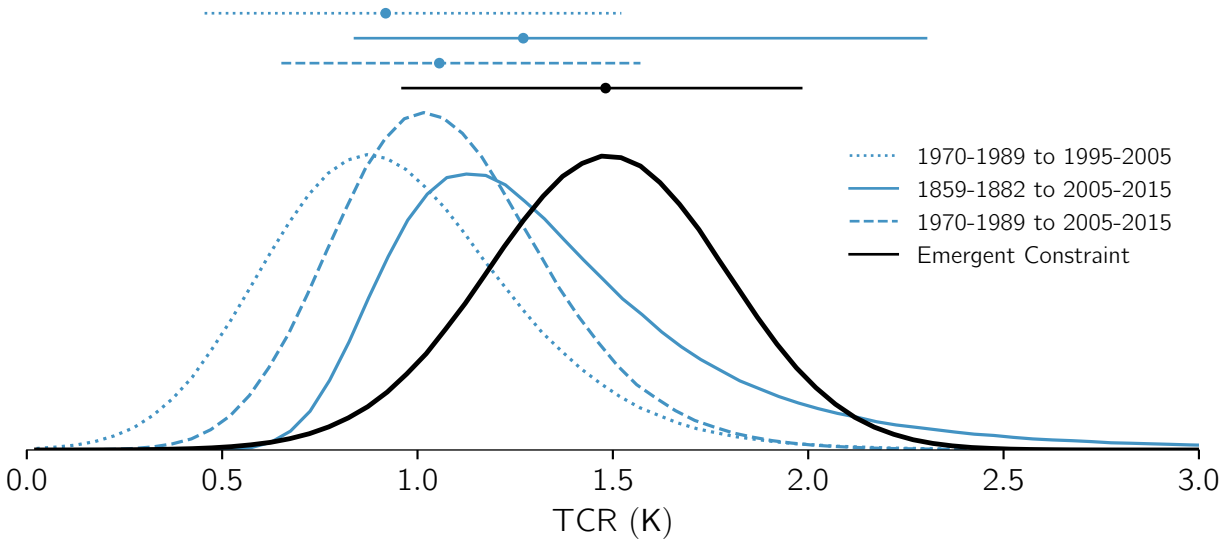

Figure S3.5: Probability density functions of TCR **with AMO–IPO correction**. Usual energy balance estimates based on observations (blue) and the functional relationship between TCR and warming from CMIP5 ensemble constrained by the observed warming (black).

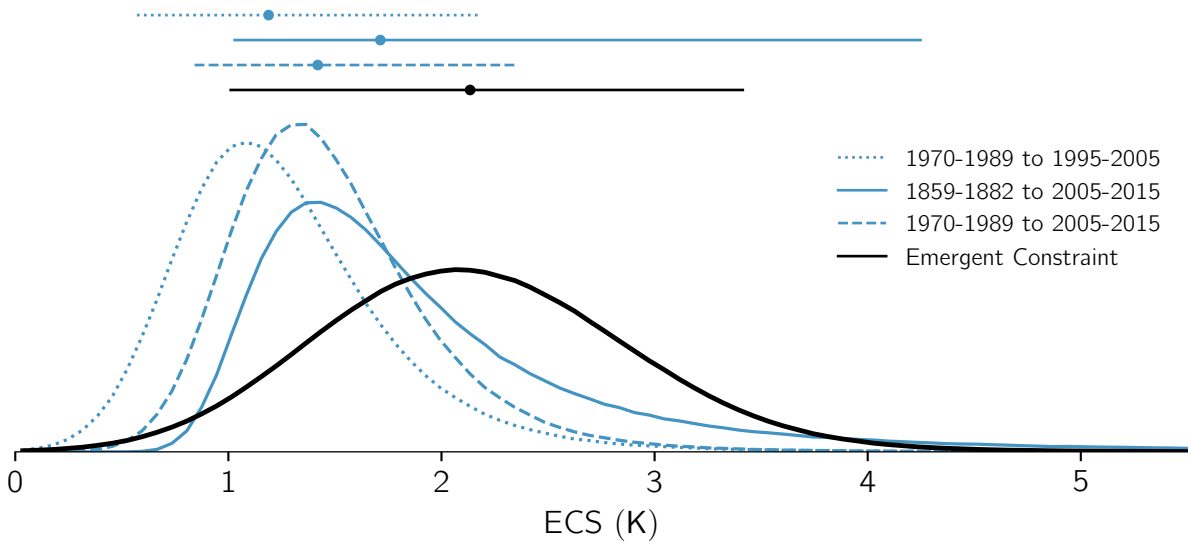

Figure S3.6: Probability density functions of ECS **with AMO–IPO correction**. Usual energy balance estimates based on observations (blue) and the functional relationship between TCR and warming from CMIP5 ensemble constrained by the observed warming (black).

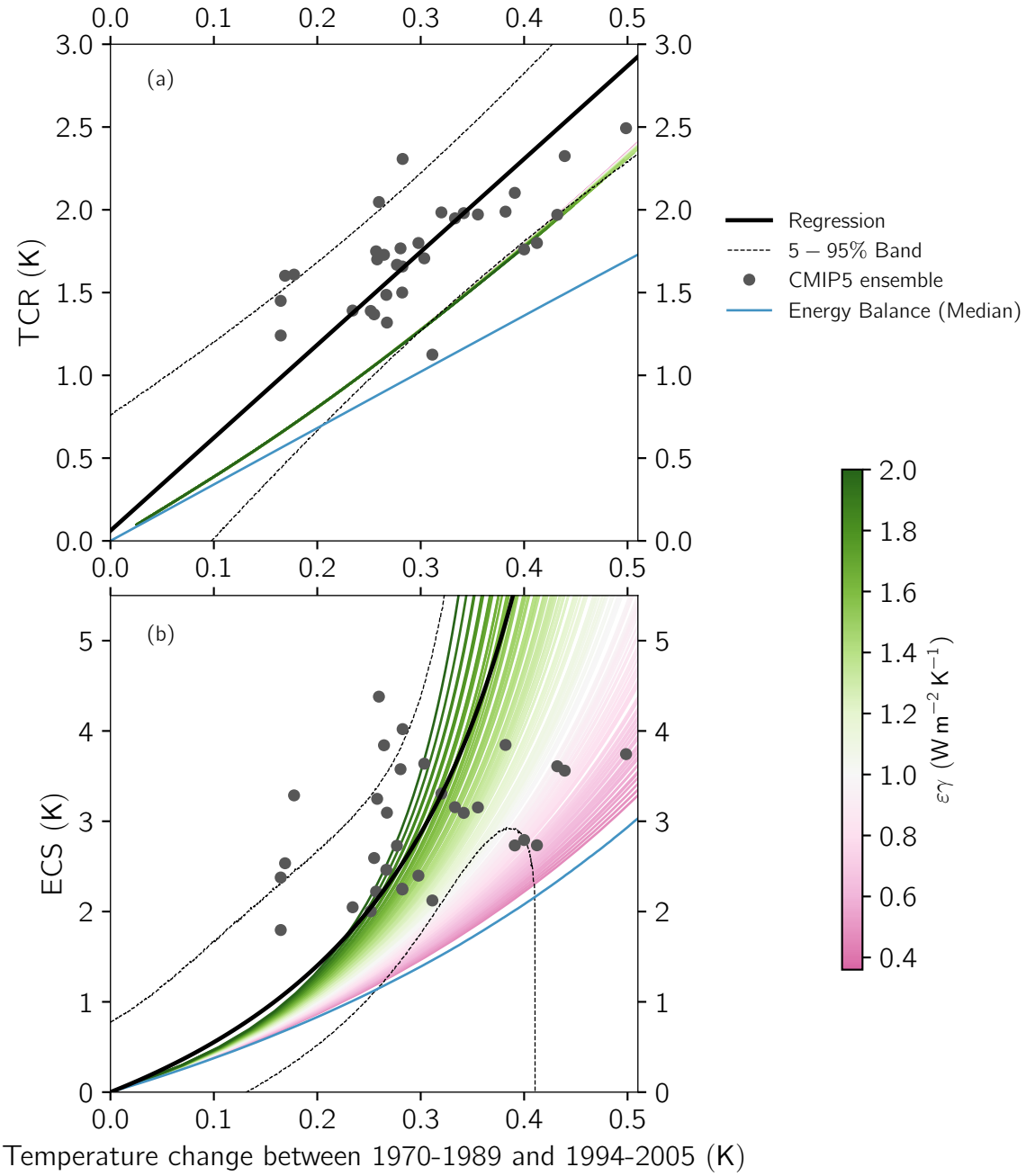

Figure S3.7: Comparison of the regression of TCR and ECS (**with AMO–IPO correction**) over warming in the post-1970s period from CMIP5 models (black) and the energy balance (blue) and two-layer model (shaded from magenta to green in terms of the product $\varepsilon\gamma$).

		monthly		**yearly**	
Dataset	# of sets	ΔT (K)	rel. corr. (%)	ΔT (K)	rel. corr. (%)
BEST	1	0.40	−26	0.40	−38
CowtanWay2.0	1	0.40	−25	0.40	−36
GISTEMP1.2.0.0	1	0.38	−24	0.38	−35
HadCRUT4.6.0.0	100	0.41	−24	0.41	−35
NOAAGlobalTemp4.0.1	1	0.37	−24	0.37	−35

Table S3.1: Post-1970s warming in the instrumental record. Means of the datasets and relative correction with AMO–IPO.

Model	Physics	TCR (K)	ECS (K)	# of Runs	ΔT (K)	std. dev.
BCC-CSM1-1	1	1.76	2.78	3	0.50	0.06
BCC-CSM1-1-M	1	2.08	2.79	3	0.50	0.09
BNU-ESM	1	2.48	3.86	1	0.58	0.00
CANESM2	1	2.29	3.65	5	0.61	0.04
CNRM-CM5	1	1.94	3.19	9	0.44	0.06
CNRM-CM5-2	1	1.65	3.36	1	0.36	0.00
ACCESS1-0	1	1.73	3.64	1	0.42	0.00
ACCESS1-3	1	1.57	3.38	3	0.31	0.03
CSIRO-MK3-6-0	1	1.67	3.88	9	0.38	0.08
INMCM4	1	1.23	1.91	1	0.20	0.00
IPSL-CM5A-LR	1	1.92	3.89	6	0.58	0.11
IPSL-CM5A-MR	1	1.93	3.97	3	0.50	0.02
IPSL-CM5B-LR	1	1.41	2.46	1	0.28	0.00
FGOALS-G2	1	1.34	3.29	3	0.37	0.01
MIROC-ESM	1	1.99	4.55	3	0.37	0.03
MIROC5	1	1.43	2.59	5	0.38	0.08
HADGEM2-ES	1	2.32	4.17	4	0.42	0.02
MPI-ESM-LR	1	1.90	3.39	3	0.38	0.04
MPI-ESM-MR	1	1.92	3.23	3	0.45	0.04
MPI-ESM-P	1	1.89	3.23	2	0.42	0.07
MPI-ESM1.1	0	1.66	2.80	100	0.35	0.07
MPI-ESM1.2-highECS	1	2.28	4.79	5	0.51	0.07
	2	2.28	4.79	4	0.29	0.04
	3	2.28	4.79	5	0.43	0.06
	4	2.28	4.79	5	0.49	0.10
MRI-CGCM3	1	1.54	2.59	3	0.26	0.08
GISS-E2-H	1	1.65	2.29	6	0.37	0.03
	2	1.75	2.26	6	0.36	0.02
	3	1.80	2.44	6	0.41	0.04
GISS-E2-R	1	1.39	2.02	6	0.36	0.04
	2	1.35	2.07	6	0.32	0.05
	3	1.53	2.29	6	0.39	0.03
CCSM4	1	1.69	2.83	6	0.50	0.03
NORESM1-M	1	1.34	2.64	3	0.33	0.03
GFDL-CM3	1	1.66	3.70	5	0.46	0.08
GFDL-ESM2G	1	1.07	2.13	1	0.60	0.00
GFDL-ESM2M	1	1.21	2.23	1	0.41	0.00

Table S3.2: Summary of parameters for the earth system models. The first column shows the name of the model or ensemble. The second column is the physics setting as classified in ESGF. The third and fourth columns are the TCR and ECS. The last three columns show information about the warming in the post-1970s: the number or `historical` runs, the mean ΔT and the spread represented by the standard deviation. Models with zero standard deviation are those with only one realisation.

	Value ($W\,m^{-2}$)		
Quantity	1859–1882 to 05–15	70–89 to 05–15	70–89 to 95–05
N (Second period)[1]	0.71 ± 0.06	0.71 ± 0.06	0.61 ± 0.05
N (First period)[2]	0.15 ± 0.07	0.27 ± 0.04	0.27 ± 0.04
ΔN	0.56 ± 0.10	0.44 ± 0.07	0.35 ± 0.06
ΔF[3]	2.16 ± 0.59	1.29 ± 0.18	1.09 ± 0.18
Contribution to ΔF[4]			
GHG	2.53 ± 0.18	1.10 ± 0.08	0.77 ± 0.05
Aerosol	-0.69 ± 0.55	-0.13 ± 0.10	-0.15 ± 0.10
Black carbon on snow	0.02 ± 0.02	-0.01 ± 0.02	-0.01 ± 0.02
Stratospheric water vapor	0.06 ± 0.03	0.01 ± 0.03	0.01 ± 0.03
Land use change	-0.10 ± 0.06	-0.01 ± 0.06	-0.01 ± 0.06
Ozone	0.29 ± 0.12	0.06 ± 0.12	0.04 ± 0.12
Contrails	0.05	0.04	0.02
Natural	0.00	0.25	0.42

Table S3.3: Forcing input for energy balance inference from observations.

TCR		ECS	
e	s	e'	s'
$(-0.14 \pm 0.33)\,K$	4.59 ± 0.80	$(0.35 \pm 0.22)\,K^{-1}$	0.28 ± 0.09

Table S3.4: Regression coefficients with standard errors for the TCR and ECS.

					%	
Type	Initial	Final	TCR (K)	5-95% (K)	P(<1.0 K)	P(>2.5 K)
Constrain	1970 - 1989	1995 - 2005	1.67	1.17 - 2.16	1.5	0.3
Energy Balance	1970 - 1989	1995 - 2005	1.41	0.90 - 2.14	9.6	1.3
Energy Balance	1970 - 1989	2005 - 2015	1.54	1.09 - 2.15	2.2	0.9
Energy Balance	1859 - 1882	2005 - 2015	1.42	0.95 - 2.56	7.7	5.6

Table S3.5: Summary of some statistics of the TCR probability density functions. Columns show calculation method, initial and final periods, median value and 5-95 percent interval. The last two columns show the likelihood of a TCR lesser than 1.0 K and greater than 2.5 K, respectively.

					%	
Type	Initial	Final	ECS (K)	5-95% (K)	P(<1.5 K)	P(>4.5 K)
Constrain	1970 - 1989	1995 - 2005	2.83	1.72 - 4.12	2.4	2.2
Energy Balance	1970 - 1989	1995 - 2005	2.07	1.24 - 3.76	14.9	2.2
Energy Balance	1970 - 1989	2005 - 2015	2.33	1.53 - 3.89	4.2	2.2
Energy Balance	1859 - 1882	2005 - 2015	1.92	1.17 - 4.75	23.0	5.7

Table S3.6: Summary of some statistics of the ECS probability density functions. Columns show calculation method, initial and final periods, median value and 5-95 percent interval. The last two columns show the likelihood of an ECS lesser than 1.5 K and greater than 4.5 K, respectively.

With AMO–IPO correction			
TCR		ECS	
e	s	e'	s'
$(0.06 \pm 0.33)\,\mathrm{K}$	5.62 ± 1.07	$(0.38 \pm 0.31)\,\mathrm{K}^{-1}$	0.22 ± 0.09

Table S3.7: Regression coefficients for the TCR and ECS. Presented with standard errors.

With AMO–IPO correction					%	
Type	Initial	Final	TCR (K)	5-95% (K)	P(<1.0 K)	P(>2.5 K)
Constrain	1970 - 1989	1995 - 2005	1.48	0.96 - 1.98	6.3	0.0
Energy Balance	1970 - 1989	1995 - 2005	0.92	0.46 - 1.52	60.2	0.1
Energy Balance	1970 - 1989	2005 - 2015	1.06	0.65 - 1.57	41.7	0.0
Energy Balance	1859 - 1882	2005 - 2015	1.27	0.84 - 2.30	18.1	3.5

Table S3.8: Summary of some statistics of the TCR probability density functions. Columns show calculation method, initial and final periods, median value and 5-95 percent interval. The last two columns show the likelihood of a TCR lesser than 1.0 K and greater than 2.5 K, respectively.

With AMO–IPO correction					%	
Type	Initial	Final	ECS (K)	5-95% (K)	P(<1.5 K)	P(>4.5 K)
Constrain	1970 - 1989	1995 - 2005	2.13	1.01 - 3.41	18.4	0.4
Energy Balance	1970 - 1989	1995 - 2005	1.19	0.57 - 2.19	73.7	0.1
Energy Balance	1970 - 1989	2005 - 2015	1.42	0.84 - 2.35	57.4	0.1
Energy Balance	1859 - 1882	2005 - 2015	1.71	1.03 - 4.28	35.5	4.4

Table S3.9: Summary of some statistics of the ECS probability density functions. Columns show calculation method, initial and final periods, median value and 5-95 percent interval. The last two columns show the likelihood of an ECS lesser than 1.5 K and greater than 4.5 K, respectively.

Model	Physics	TCR (K)	ECS (K)	# of Runs	ΔT (K)	std. dev.
BCC-CSM1-1	1	1.80	2.73	3	0.41	0.05
BCC-CSM1-1-M	1	2.10	2.73	3	0.39	0.07
BNU-ESM	1	2.49	3.74	1	0.50	0.00
CANESM2	1	2.32	3.56	5	0.44	0.04
CNRM-CM5	1	1.98	3.09	9	0.34	0.06
CNRM-CM5-2	1	1.70	3.25	1	0.26	0.00
ACCESS1-0	1	1.77	3.58	1	0.28	0.00
ACCESS1-3	1	1.61	3.29	3	0.18	0.03
CSIRO-MK3-6-0	1	1.73	3.84	9	0.26	0.05
INMCM4	1	1.24	1.80	1	0.16	0.00
IPSL-CM5A-LR	1	1.97	3.61	6	0.43	0.03
IPSL-CM5A-MR	1	1.99	3.85	3	0.38	0.05
IPSL-CM5B-LR	1	1.45	2.38	1	0.16	0.00
FGOALS-G2	1	1.32	3.09	3	0.27	0.01
MIROC-ESM	1	2.05	4.38	3	0.26	0.01
MIROC5	1	1.49	2.46	5	0.27	0.04
HADGEM2-ES	1	2.31	4.02	4	0.28	0.03
MPI-ESM-LR	1	1.98	3.31	3	0.32	0.03
MPI-ESM-MR	1	1.95	3.16	3	0.33	0.01
MPI-ESM-P	1	1.97	3.15	2	0.36	0.03
MPI-ESM1.1	0	1.67	2.73	100	0.28	0.05
MPI-ESM1.2-highECS	1	2.34	4.39	5	0.38	0.05
	2	2.34	4.39	4	0.15	0.02
	3	2.34	4.39	5	0.29	0.04
	4	2.34	4.39	5	0.38	0.07
MRI-CGCM3	1	1.60	2.53	3	0.17	0.08
GISS-E2-H	1	1.66	2.24	6	0.28	0.02
	2	1.75	2.22	6	0.26	0.02
	3	1.80	2.40	6	0.30	0.02
GISS-E2-R	1	1.39	2.00	6	0.25	0.04
	2	1.39	2.05	6	0.23	0.03
	3	1.50	2.25	6	0.28	0.04
CCSM4	1	1.76	2.79	6	0.40	0.02
NORESM1-M	1	1.37	2.59	3	0.25	0.03
GFDL-CM3	1	1.71	3.64	5	0.30	0.06
GFDL-ESM2G	1	1.05	2.05	1	0.40	0.00
GFDL-ESM2M	1	1.13	2.12	1	0.31	0.00

Table S3.10: Summary of parameters **with AMO–IPO correction**. The first column shows the name of the model or ensemble. The second column is the physics setting as classified in ESGF. The third and fourth columns are the TCR and ECS. The last three columns show information about the warming in the post-1970s: the number or `historical` runs, the mean ΔT and the spread represented by the standard deviation. Models with zero standard deviation are those with only one realisation.

		AMO–Niño 3.4				AMO–IPO			
		monthly		yearly		monthly		yearly	
Model	Physics	β_1	β_2	β_1	β_2	β_1	β_2	β_1	β_2
BCC-CSM1-1	1	0.15	0.06	0.32	0.06	0.14	0.11	0.30	0.08
BCC-CSM1-1-M	1	0.34	0.05	0.78	0.05	0.32	0.09	0.78	0.08
BNU-ESM	1	0.23	0.07	0.39	0.08	0.19	0.11	0.32	0.11
CANESM2	1	0.30	0.08	0.45	0.09	0.22	0.12	0.34	0.12
CNRM-CM5	1	0.30	0.05	0.50	0.07	0.29	0.07	0.49	0.08
CNRM-CM5-2	1	0.35	0.05	0.94	0.06	0.35	0.06	0.97	0.06
ACCESS1-0	1	0.29	0.08	0.45	0.10	0.28	0.11	0.44	0.11
ACCESS1-3	1	0.21	0.08	0.25	0.10	0.19	0.10	0.23	0.10
CSIRO-MK3-6-0	1	0.26	0.09	0.31	0.12	0.24	0.11	0.30	0.11
INMCM4	1	0.13	0.06	0.19	0.07	0.13	0.08	0.21	0.07
IPSL-CM5A-LR	1	0.20	0.09	0.32	0.08	0.19	0.09	0.32	0.07
IPSL-CM5A-MR	1	0.22	0.08	0.30	0.09	0.18	0.10	0.26	0.09
IPSL-CM5B-LR	1	0.22	0.07	0.31	0.07	0.22	0.06	0.31	0.06
FGOALS-G2	1	0.24	0.06	0.65	0.03	0.25	0.08	0.66	0.04
MIROC-ESM	1	1.36	−0.01	3.41	−0.41	1.51	−0.08	3.27	−0.37
MIROC5	1	0.30	0.09	0.43	0.08	0.27	0.10	0.39	0.09
HADGEM2-ES	1	0.29	0.08	0.41	0.10	0.31	0.09	0.44	0.09
MPI-ESM-LR	1	0.22	0.09	0.33	0.09	0.21	0.10	0.35	0.09
MPI-ESM-MR	1	0.18	0.08	0.28	0.09	0.18	0.09	0.29	0.08
MPI-ESM-P	1	0.22	0.08	0.34	0.09	0.21	0.10	0.33	0.09
MPI-ESM1.1		**0.23**	**0.09**	**0.32**	**0.09**	**0.22**	**0.09**	**0.33**	**0.08**
MPI-ESM1.2-highECS	1	0.38	0.07	0.44	0.07	0.39	0.07	0.47	0.06
	2	0.38	0.07	0.44	0.07	0.39	0.07	0.47	0.06
	3	0.38	0.07	0.44	0.07	0.39	0.07	0.47	0.06
	4	0.38	0.07	0.44	0.07	0.39	0.07	0.47	0.06
MRI-CGCM3	1	0.15	0.06	0.27	0.06	0.15	0.08	0.27	0.07
GISS-E2-H	1	0.18	0.07	0.31	0.06	0.18	0.09	0.31	0.07
	2	0.23	0.07	1.23	0.03	0.24	0.08	1.28	0.02
	3	0.48	0.06	2.00	−0.05	0.52	0.06	1.99	−0.07
GISS-E2-R	1	0.17	0.07	0.31	0.07	0.18	0.07	0.34	0.06
	2	0.18	0.07	0.27	0.06	0.20	0.06	0.29	0.05
	3	0.24	0.07	0.33	0.07	0.25	0.07	0.35	0.06
CCSM4	1	0.24	0.06	0.40	0.06	0.19	0.08	0.33	0.08
NORESM1-M	1	0.27	0.06	0.47	0.05	0.22	0.08	0.40	0.07
GFDL-CM3	1	0.62	0.04	1.36	0.00	0.65	0.03	1.55	−0.08
GFDL-ESM2G	1	0.31	0.09	0.44	0.09	0.31	0.10	0.45	0.09
GFDL-ESM2M	1	0.33	0.06	0.50	0.05	0.29	0.08	0.46	0.07

Table S3.11: Coefficients of the regression of `piControl` GMSTs and SST patterns. In all cases, the offset parameter β_0 is close to zero and is not listed but is used in the calculations. Highlighted are the results of the MPI-ESM1.1 ensemble.

The central role of clouds in the evolution of the climate feedback parameter in response to forcing

But in the meantime this is only one future.
Dónde no hay nada y todo es oscuro.
Wir können entscheiden die Wissenschaft zu folgen.

Abstract

An evolving sea surface temperature pattern changes the cloud feedback between decadal and centennial timescales. We find that this change in the cloud feedback not only explains almost half of the change in the climate feedback parameter but also controls the remaining mechanisms explaining the parameter change. By using a cloud locking technique, we prevent that clouds respond to the sea surface temperature pattern in the MPI-ESM1.2 model and the lapse-rate feedback weakens. The weakening substantially reduces the tropical free-tropospheric warming across both timescales. As some authors have proposed, the role of clouds in the evolution of the climate feedback parameter depends on the tropical free-tropospheric warming. Thus, the synergy between the cloud and lapse-rate feedbacks induces the warming that the lapse-rate feedback cannot provide alone.

4.1 Introduction

λ varies

The climate feedback parameter λ represents the response of Earth's feedback mechanisms that counteract an energy imbalance at the top of the atmosphere (TOA) generated, for instance, by radiative forcing. This TOA energy imbalance entails changes in the surface temperature, and the feedback mechanisms respond to these changes (Sherwood et al. 2015; Schlesinger and Mitchell 1987), gradually reducing the TOA energy imbalance. Hence, the ratio of the change in global mean TOA imbalance to the change in global mean surface temperature defines the climate feedback parameter. We estimate the climate feedback parameter in models with abrupt forcing experiments in which we quadruple the atmospheric CO_2 concentration starting from pre-industrial conditions (`abrupt4xCO2` experiments). In these experiments, one usually regresses the annual averages of global mean TOA imbalance change on the corresponding global mean surface temperature change (Gregory et al. 2004). Depending on the period used to compute the regression, the climate feedback parameter changes (Senior and Mitchell 2000; Andrews et al. 2015). Commonly, a curvature in a plot of annually-averaged global mean TOA imbalance versus surface temperature shows the inconstancy of the climate feedback parameter: in the first decades of the experiment the climate feedback parameter is more negative than thereafter in most climate models.

This noticeable change in the climate feedback parameter poses questions such as

which feedback mechanisms contribute to the inconstancy and if these changes exist under different forcing. Some authors identified, under different forcing pathways, that the feedback mechanisms depend on the system's base state (Good et al. 2015; Gregory et al. 2015; Senior and Mitchell 2000; Voss and Mikolajewicz 2001; Colman and McAvaney 2009; Caballero and Huber 2013; Jonko et al. 2013; Block and Mauritsen 2013; Meraner et al. 2013). In these cases, the feedback mechanisms contribute to the climate feedback parameter depending on the applied forcing, thereby explaining part of the inconstancy as state-dependence. Other authors formulate the inconstancy as a time-dependence in terms of the regional contributions of feedback mechanisms in relation to an evolving surface temperature pattern (Winton et al. 2010; Armour et al. 2013). Notwithstanding this discussion between state- or time-dependence, several studies found a relationship between the climate feedback parameter inconstancy and variations in the cloud feedback as well as in high-latitude mechanisms such as surface-albedo feedback (Senior and Mitchell 2000; Block and Mauritsen 2013; Andrews et al. 2015; Winton et al. 2010; Armour et al. 2013).

Cloud feedback and $\Delta\lambda$

In the ensemble of the climate model intercomparison project phase five (CMIP5), Andrews et al. (2015) found that cloud feedback mainly evolves in the tropical regions. They connect this changing cloud feedback to an evolving sea surface temperature (SST) pattern induced by the CO_2 forcing. This SST pattern consists of regions that warm at different rates compared to the global mean and that this pattern changes between early and later periods after a forcing has been applied. Between the decadal and centennial timescales, the tropical deep-convective regions warm less than the global mean, whereas subsidence regions warm more. Zhou et al. (2016) proposed that the free-tropospheric warming provided by the tropical deep convection remotely warms the air aloft subsidence regions where low-level stratocumuli form. The warming aloft leads to more stratocumuli by increasing low-level atmospheric stability. More stratocumuli reflect more shortwave radiation, leading to a temporary dampening of global warming. As the SST pattern evolves, the subsidence regions warm more and catch up with the remote free-tropospheric warming. Therefore, stability reduces and stratocumuli wane, reflecting less shortwave radiation. Observations link decadal cloud variations with variations in Earth's energy budget (Zhou et al. 2016; Mauritsen 2016), giving foundations to the mechanism. Ceppi and Gregory (2017) also showed a correlation between the SST pattern and lapse-rate and surface-albedo feedbacks in CMIP5 models.

Objectives and results

We investigate the role of clouds in the evolution of the climate feedback parameter within the context of one complex climate model, the Max Planck Institute Earth System Model version 1.2.01p1 (MPI-ESM1.2 Mauritsen et al. 2019). We use a cloud-locking technique to prevent that clouds evolve following the SST pattern. Without cloud feedback, and by construction without cloud feedback changes, we evaluate not only the direct role of clouds in the evolution of the climate feedback parameter but also possible influences on other feedback mechanisms. We conclude that the role of clouds goes beyond a purely radiative cloud feedback mechanism.

4.2 Preparatory enquiries

CMIP5 and MPI-ESM1.2 $\Delta\lambda$

To show the inconstancy of the climate feedback parameter λ in the CMIP5 ensemble, we inspect results from the `abrupt4xCO2` experiment. We define two periods in these

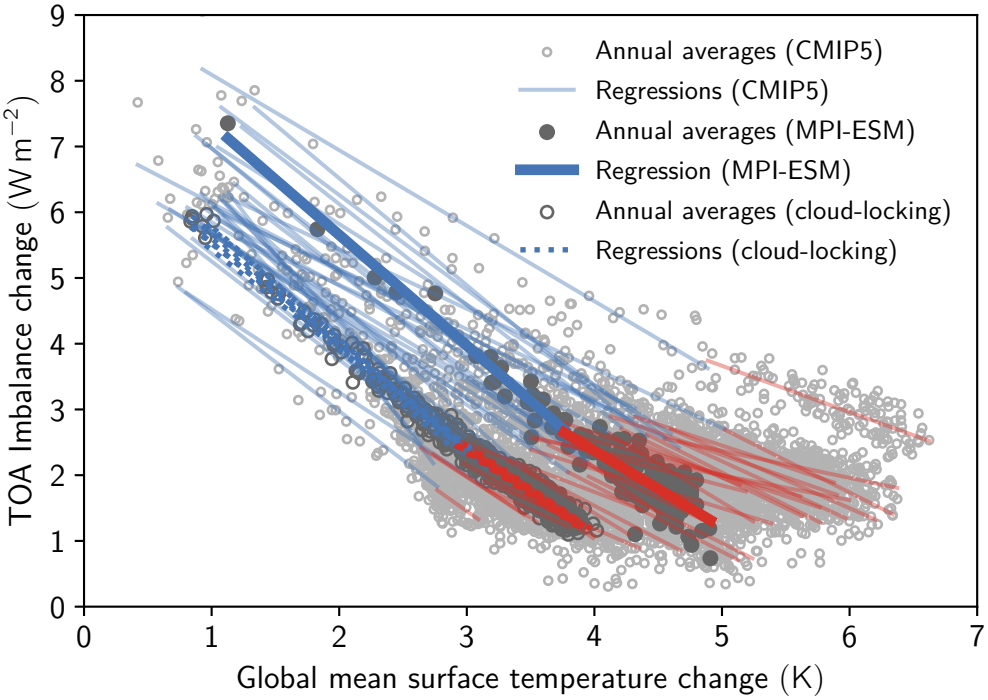

Figure 4.1: Inconstancy of λ. TOA imbalance - surface temperature plot for an abrupt quadrupling of atmospheric CO_2. Dots are annual averages. Blue lines are regressions using years 1-20 (early period), whereas red lines use years 21-150 (late period). Clear thin lines and small hollow dots depict the CMIP5 ensemble. Solid thick lines and large dots show the Max-Planck-Institute Earth System Model version 1.2.01p1 (MPI-ESM1.2) and dotted lines and large hollow dots show seven experiments with cloud-locking in the MPI-ESM1.2 model. In most models, the slope (λ) becomes less negative as time goes by.

experiments: the *early period* includes the first twenty years, and the *late period* goes from year 21 to year 150 (figures 4.1 and 4.2). The regressions on the early period data show a more negative slope than those done on the late period: In most models, the change in temperature relative to the TOA imbalance change during the early period is smaller than during the late period. The ensemble mean change in the climate feedback parameter between late and early periods is $\Delta\lambda = 0.49\ \mathrm{W\,m^{-2}\,K^{-1}}$ (-0.14 to 1.08, 5-95 percentile range). The MPI-ESM1.2 model also shows a $\Delta\lambda$ comparable with the CMIP5 ensemble mean: $0.51\ \mathrm{W\,m^{-2}\,K^{-1}}$ (0.11 to 0.85, 5-95 percentile range).

MPI-ESM1.2 and SST pattern

The SST pattern is defined as the regression of the local surface temperature change on the global mean surface temperature change (Andrews et al. 2015). The comparison between regressions using early and late periods in the MPI-ESM1.2 model shows the pattern's evolution in this model (figure 4.3). The Southeastern and Northeastern Pacific regions warm more during the late period, as well as the Southern Ocean and the North Atlantic region, which is consistent with the Zhou et al. (2016) mechanism that we described in the introduction. MPI-ESM1.2 SST pattern is also similar to the pattern found in the CMIP5 models by Andrews et al. (2015).

MPI-ESM1.2 and shortwave cloud feedback

We can also check if the MPI-ESM1.2 model shows such an expected variation in the

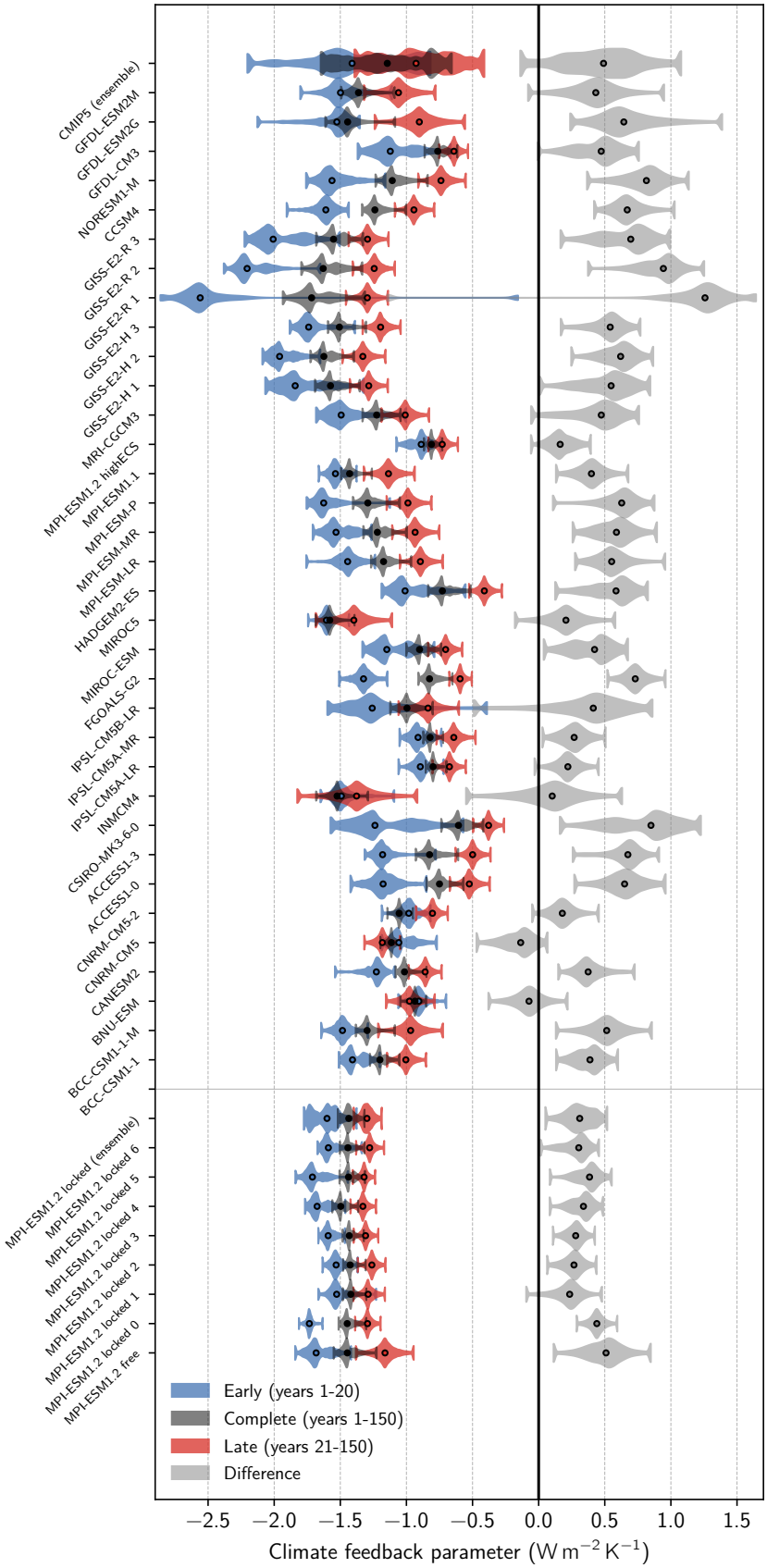

Figure 4.2: Modelled climate feedback parameter for CMIP5 models, MPI-ESM1.2-highECS, MPI-ESM1.1 Grand Ensemble and MPI-ESM1.2 free- and locked-cloud experiments. Blue distributions correspond to the early period (years 1 to 20). Red distributions correspond to the late period (years 21 to 150). Dark grey distributions correspond to the complete `abrupt4xCO2` run (years 1 to 150). Light grey distributions show the difference between red and blue. The dots mark the median values of the distributions. The limits mark the 5 to 95 percentile range.

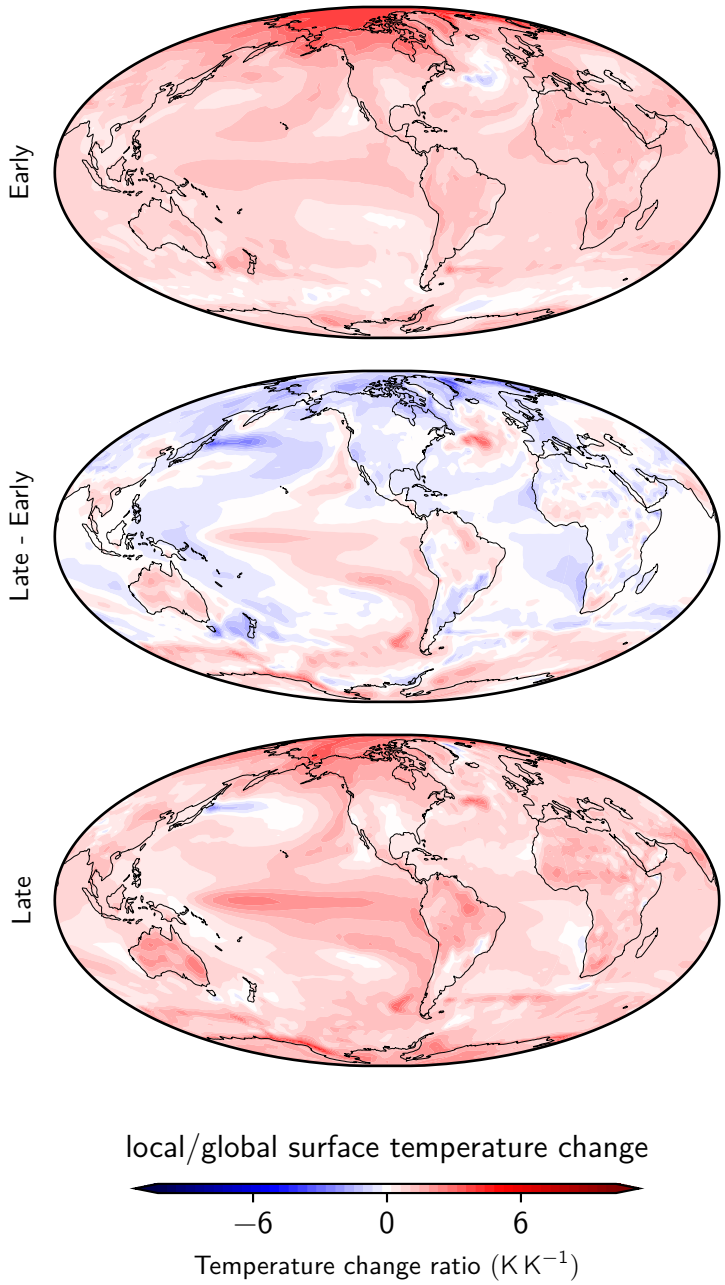

Figure 4.3: SST pattern in MPI-ESM1.2 for an `abrupt4xCO2` experiment. The slope of the regression of local surface temperature change on global mean surface temperature change. Top panel: Early period (years 1-20). Bottom panel: Late period (years 21-150). Middle panel: Late-Early.

shortwave cloud feedback between early and late periods (figure 4.4). There is a more negative shortwave cloud feedback during the early period in the trade regions, that switch to mostly positive feedback during the late period. Thus, these results show that the MPI-ESM1.2 model is suitable for studying the mechanism presented by Zhou et al. (2016).

4.3 Methods

Cloud-locking The idea of cloud-locking is that the cloud properties seen by the radiation do not change across the forced experiments, thereby leading to zero cloud feedback. Using this technique, one can assess the effect of cloud feedback mechanisms on a given phenomenon. Researchers have used the technique to study the influence of the cloud feedbacks on surface temperature change (Wetherald and Manabe 1988), the cloud-induced amplification of the El Niño Southern Oscillation (ENSO) (Rädel et al. 2016) and its periodicity (Middlemas et al. 2019), as well as the storm tracks and mid-latitude eddy-driven jets (Grise et al. 2019). Other studies have locked other feedback mechanisms and studied their influence, e.g. of water-vapour feedback (Hall and Manabe 1999) and surface-albedo feedback in surface temperature (Hall 2004; Graversen and Wang 2009), multiple feedback mechanisms role in polar amplification (Langen et al. 2012; Graversen et al. 2014), or to study synergies between feedback processes (Mauritsen et al. 2013).

Cloud-locking implementation

In this work, the cloud-locking consists of prescribing the cloud water and ice content, as well as the cloud fraction, used in the radiative transfer calculations. The prescribed fields come from a pre-industrial control experiment with evolving clouds. The method of specifying the clouds in the locked-cloud experiments differs across studies. Usually, stored cloud fields are prescribed in sequence, either repeating a single year or a sequence of years, though some studies concerned with sub-annual natural variability randomly shuffle the prescribed fields by selecting a given day and time from a set of years of stored clouds (Rädel et al. 2016; Olonscheck et al. 2019). In this study, we store seven years of clouds and run locked-cloud experiments with each one of them at a time. Thereby we wish to preserve an annual cycle but suppress inter-annual variability, while at the same time exploring the possible influence of the choice of year that is prescribed. To this end, we selected the years by their El Niño 3.4 index in the free-cloud pre-industrial control experiment. We choose three years with positive index and three with negative index. We select each one of the three years from years with strong, medium and weak index, respectively. Additionally, we choose another case with positive index, corresponding to the year with the strongest positive index in the free-cloud pre-industrial control run. With each of the seven stored years, we run a locked-cloud pre-industrial control and, starting from this control, an `abrupt4xCO2` experiment.

4.4 Global mean results and SST pattern under cloud-locking

Comparison of λ

All the locked-cloud experiments evolve essentially in the same manner, regardless of the prescribed clouds used in each experiment. From the slopes of the early-period regressions, we find that the free-cloud λ is $-1.68\ \mathrm{W\,m^{-2}\,K^{-1}}$ (-1.84 to -1.42, 5-95 percentile range) and it is within the range of the locked-cloud ensemble: $-1.60\ \mathrm{W\,m^{-2}\,K^{-1}}$ (-1.78 to

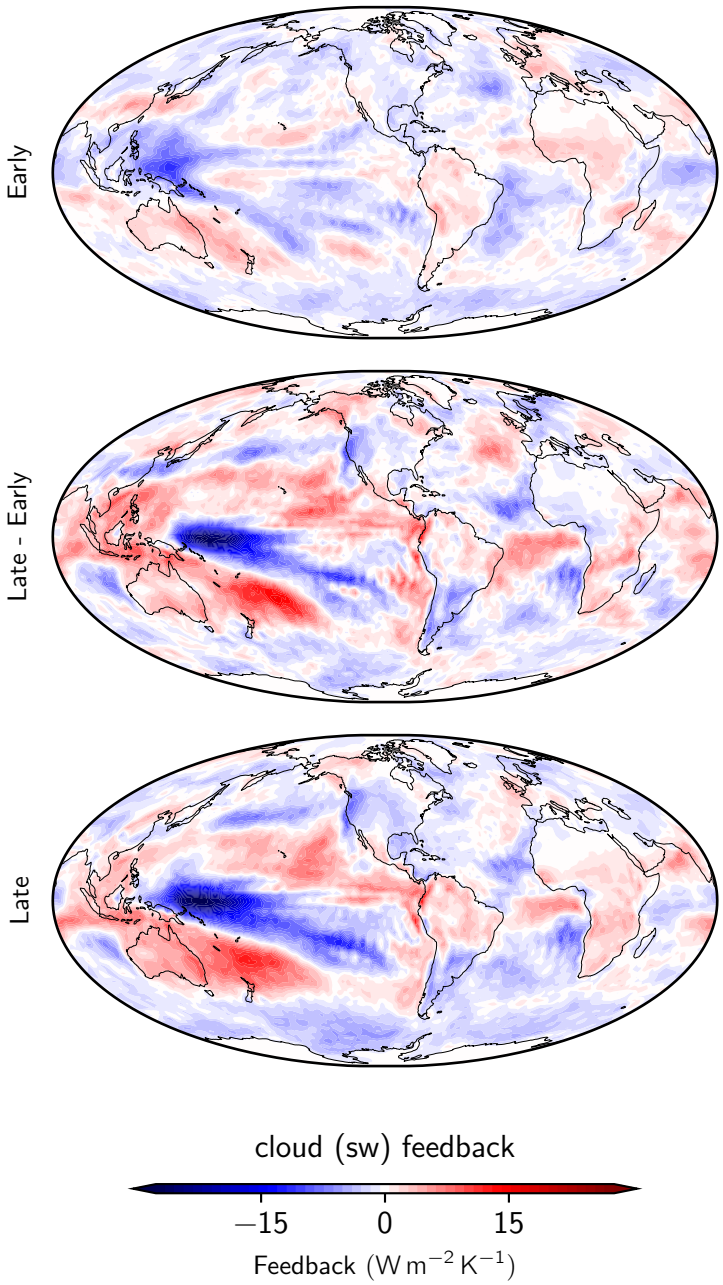

Figure 4.4: Shortwave cloud feedback in MPI-ESM1.2 for an `abrupt4xCO2` experiment. Top panel: Early period (years 1-20). Bottom panel: Late period (years 21-150). Middle panel: Late-Early.

-1.38, 5-95 percentile range). In contrast, late-period free-cloud λ is -1.16 W m^{-2} K^{-1} (-1.38 to -0.94) and more positive than the lock-cloud ensemble mean: -1.30 W m^{-2} K^{-1} (-1.40 to -1.19, 5-95 percentile range). Hence there is a statistically significant change in feedback between the eperiments which is is in line with our expectation.

Cloud radiative adjustment

The other very notable aspect that the locked-cloud `abrupt4xCO2` experiments show is a lack of cloud radiative forcing adjustment. The adjustment happens at the beginning of the run when the change in forcing modifies the atmospheric temperature, not necessarily with a linkage to the surface temperature. The perturbed temperature profile alters clouds and increases the initial TOA imbalance (Sherwood et al. 2015). If clouds do not change, then the adjustment cannot happen, and the system starts with a smaller global mean TOA imbalance (figure 4.1).

Comparison of $\Delta\lambda$

Nevertheless, turning our attention again to the change in λ, we find that the locked-cloud ensemble mean change in the climate feedback parameter is $\Delta\lambda = 0.31$ W m^{-2} K^{-1} (0.05 to 0.52, 5-95 percentile range) in comparison with the 0.51 W m^{-2} K^{-1} (0.11 to 0.85) of the free-cloud experiment (figure 4.2). Thus, in MPI-ESM1.2, clouds explain 0.19 W m^{-2} K^{-1} (-0.29 to 0.65) of the change in the climate feedback parameter: almost a half of the difference in the free-cloud experiment. These results are consistent with the SST pattern-effect mechanism. By cancelling cloud feedback, the locked-cloud late period does not lose stratocumuli, thereby changing less the climate feedback parameter between the early and the late period. However, the $\Delta\lambda$ in the locked-cloud experiments is not negligible, considering that its value and uncertainty are within the CMIP5 5-95 percentile range of -0.14 to 1.08 W m^{-2} K^{-1} and zero is not included in the locked-cloud 5-95 percentile range. Thus, it is of value to understand this remaining non-cloud pattern effect, which, if mechanistically sound, could add confidence to the overall sign of the pattern effect.

SST pattern in locked-cloud experiments

To investigate the origin of this remaining change in the climate feedback parameter, we first inspect the SST pattern of the locked-cloud experiments (figure 4.5). Because experiments behave globally in a similar fashion, we take one of them, obtain its SST pattern and analyse the zonal mean compared to the free-cloud case (figure 4.6). We detect the similarities in the pattern: both free- and locked-cloud experiments present polar amplification, as well as a shift of the warming from the Northern Hemisphere to the Southern Hemisphere between the early and late periods. However, during the early period, the Southern Ocean warms more in the locked- than in the free-cloud experiment. The southern polar amplification during the late period also becomes stronger in the locked- than in the free-cloud case. In contrast, the northern polar amplification during the early period is weaker in the locked- than in the free-cloud case. Notwithstanding, apart from high- and middle-latitude differences, the locked-cloud southern and equatorial tropics warm in the same proportion during the early and late periods.

Vertical changes

Since the tropospheric warming plays an essential role in the Zhou et al. (2016) mechanism, we now examine the vertical temperature changes (figure 4.7) across the locked-cloud ensemble. In the tropics, during the early and late periods and in both locked- and free-cloud experiments, the free troposphere warms in a similar proportion to the corresponding surface warming, signalling the role of the tropical deep convection in warming the profile. However, the free troposphere consistently warms less in the locked-cloud ensemble than in the free-cloud experiment. Thus, the rise of the tropical anvil

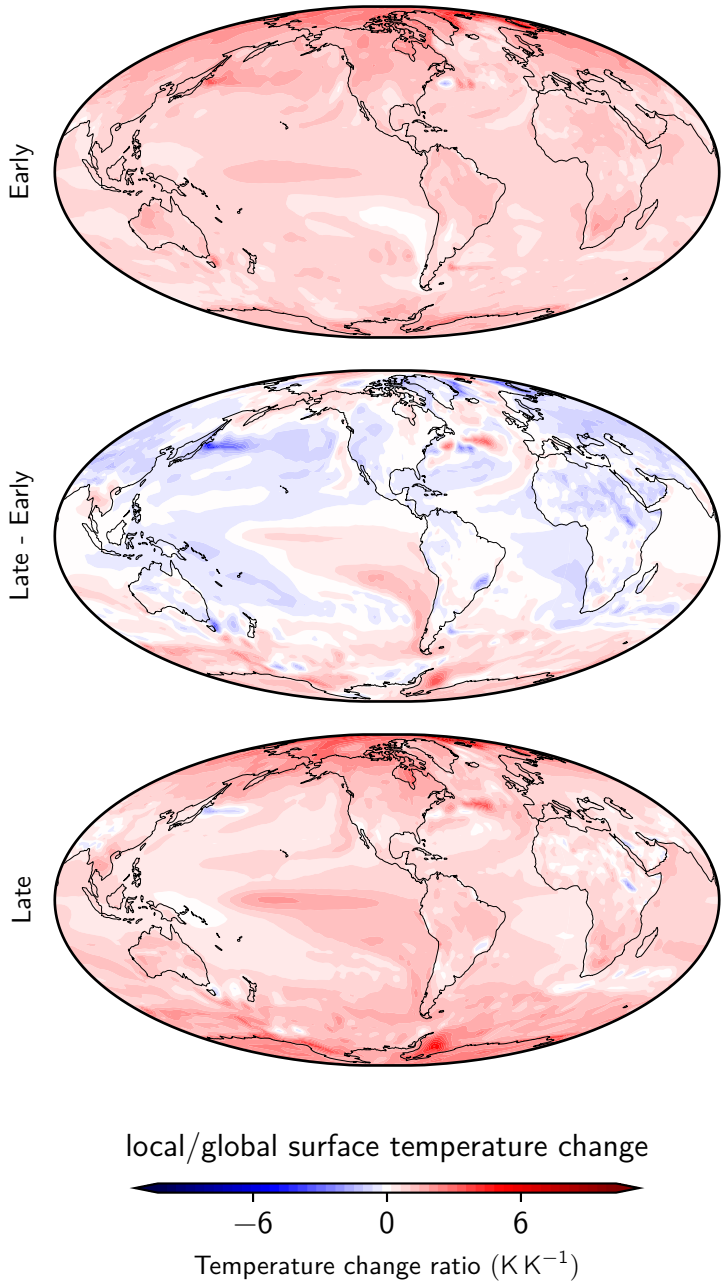

Figure 4.5: SST pattern in the MPI-ESM1.2 model for an `abrupt4xCO2` experiment with cloud-locking. The slope of the regression of local surface temperature change on global mean surface temperature change. Top panel: Early period (years 1-20). Bottom panel: Late period (years 21-150). Middle panel: Late-Early. Same colour scale as in figure 4.3. Note the stronger southern polar amplification during the late period in comparison to the free-cloud case.

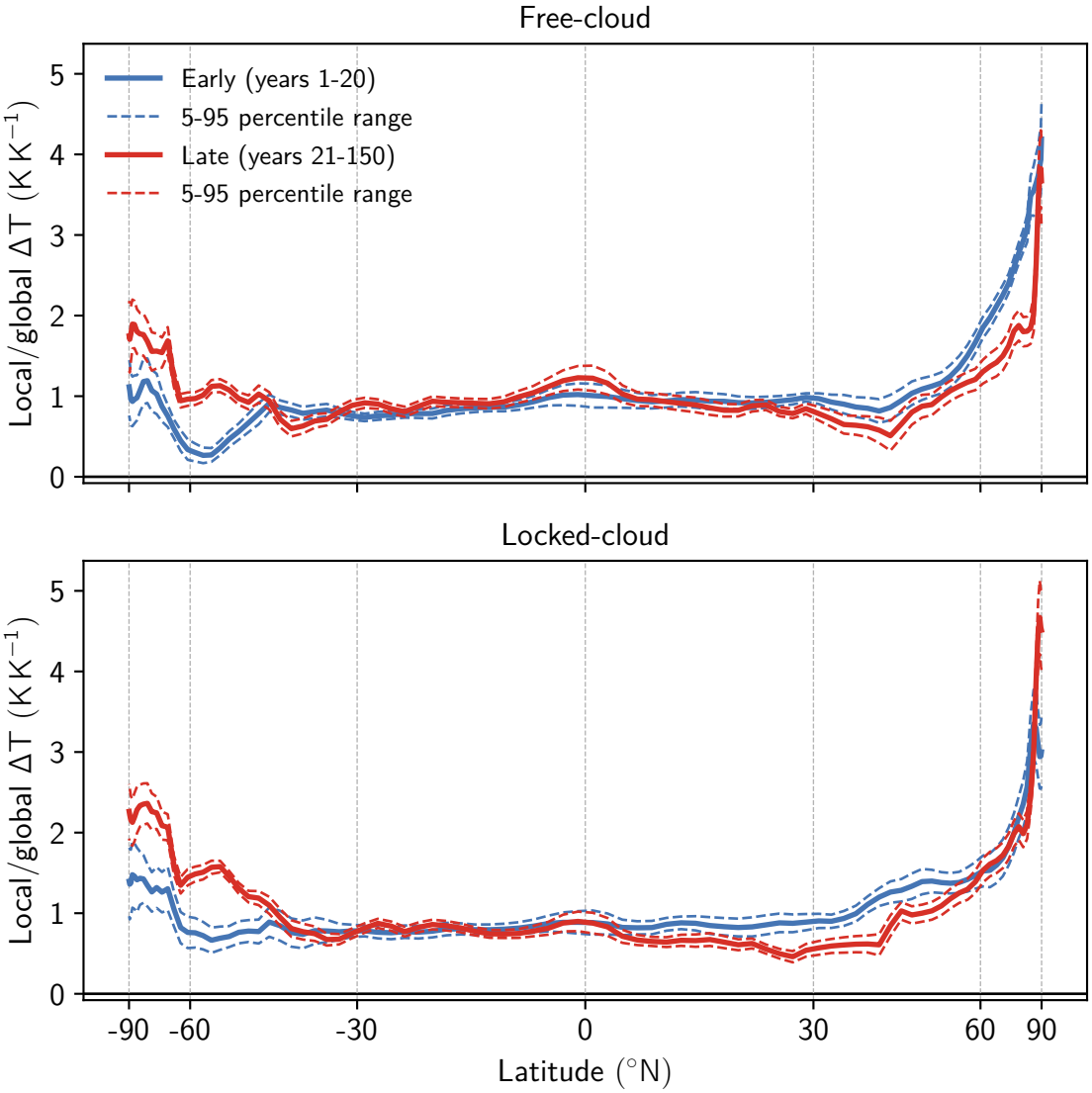

Figure 4.6: Warming pattern in the free and locked-cloud `abrupt4xCO2` experiments. The slope of the regression of local surface temperature change on global mean surface temperature change. Zonal mean. Blue is the early period (years 1-20). Red is the late period (years 21-150). Dashed lines mark the 5-95 percentile range in the estimate of the slope. Top panel: Free-cloud case. Bottom panel: Locked-cloud case.

clouds provides the necessary tropical free-tropospheric warming that regulates the stability in the subsidence regions, thereby enabling changes in cloud feedback. In the middle and high latitudes, the profiles are similar between locked- and free-cloud experiments. In the southern middle latitudes, the free-cloud experiment shows the shift in the magnitude of the warming between early and the late periods. This shift is part of the Zhou et al. (2016) mechanism that controls the stability in the subsidence regions. Although the shift is also present in the locked-cloud ensemble, it becomes less prominent. In the northern hemisphere, the shift is inverted and reduced in magnitude, possibly by the influence of northern hemisphere landmasses.

The weaker tropical warming also suggests changes in other feedback mechanisms such as the water-vapour feedback and with that explaining the remaining difference in the climate feedback parameter between the early and late periods. To investigate this, we apply the partial radiation perturbations (PRP) technique to one of the locked-cloud experiments and analyse the components of the TOA imbalance.

4.5 Feedback analysis

Partial radiation perturbations The partial radiation perturbations technique separates the influence of individual state variables on the radiative flux. The technique takes a reference for a given state variable s and compares the radiation calculations with the actual state ($R(x)$) and that with the actual state but with the variable s in the reference state ($R(x^*)$). Thus, the difference $R(x) - R(x^*)$ is the contribution to the radiative flux of the change in the state variable (Wetherald and Manabe 1988; Colman and McAvaney 1997). Some biases result from the implicit assumption that the state variables are temporarily uncorrelated (Colman and McAvaney 1997). To solve this problem, one can take a reference value for all the variables and make four radiative flux calculations. Then one calculates a forward and a backward difference. To alleviate the decorrelation, one takes the average of the differences. This technique is computationally far more expensive than the radiative kernels (Soden et al. 2008). However, radiative kernels assume a linear relationship in the response function (Soden et al. 2008), which is unsuitable for certain feedbacks such as clouds (Klocke et al. 2013) and other feedbacks under strong forcing (Mauritsen et al. 2019; Meraner et al. 2013). Instead, partial radiation perturbations give a complete solution for all feedbacks, only limited by the spectral resolution and the numerical approximations of the radiative transfer scheme.

Global lapse-rate and water-vapour feedbacks

The free-cloud experiment has positive cloud feedback, whereas cloud-locking is zero by construction (figure 4.8). The lapse-rate feedback decreases in magnitude in the locked-cloud experiment (See also table S4.1). The difference between early and late periods is more substantial than in the free-cloud case. The same, though with opposite sign, occurs to the magnitude of the water-vapour feedback. Remarkably, the sum of the lapse-rate and water-vapour feedbacks and their change between the early and late periods is almost the same in the locked- and free-cloud experiments (table S4.1). Thus, a significant fraction of the remaining change in the climate feedback parameter comes from this almost-invariant joint contribution of lapse-rate and water-vapour feedbacks.

Zonally-averaged lapse-rate and water-vapour feedbacks

The differences in the zonally-averaged lapse-rate feedback between early and late periods in the free-cloud case are limited to the deep tropics and the high latitudes (figure

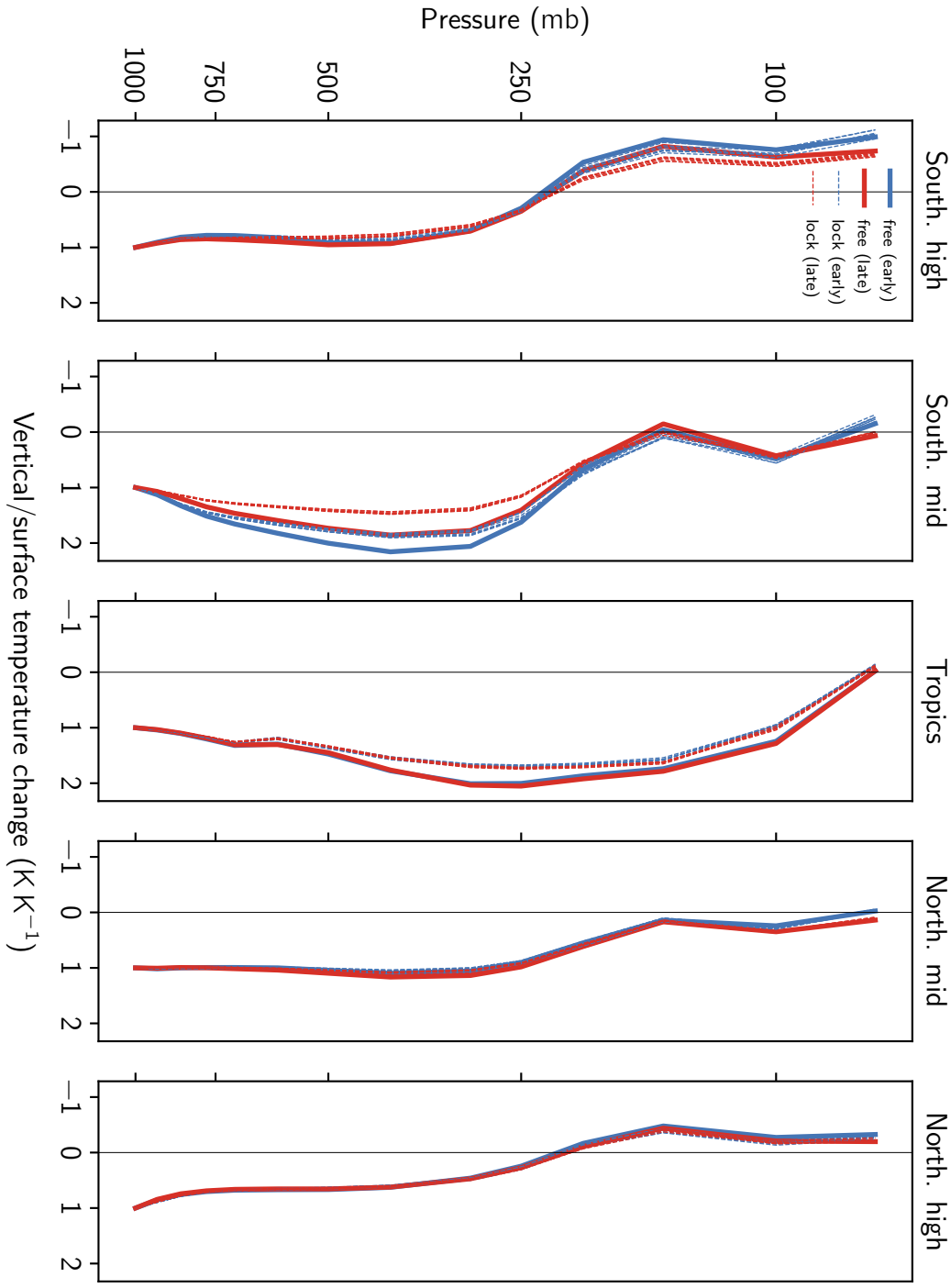

Figure 4.7: Vertical temperature change profiles normalised by the corresponding surface change. Each panel shows the mean profiles in latitudinal bands (in °N): -90 to -60, -60 to -30, -30 to 30, 30 to 60 and 60 to 90. Blue profiles correspond to the early period (years 1-20). Red profiles show the late period (years 21-150). Dashed lines designate locked-cloud experiments and solid lines the free-cloud experiment.

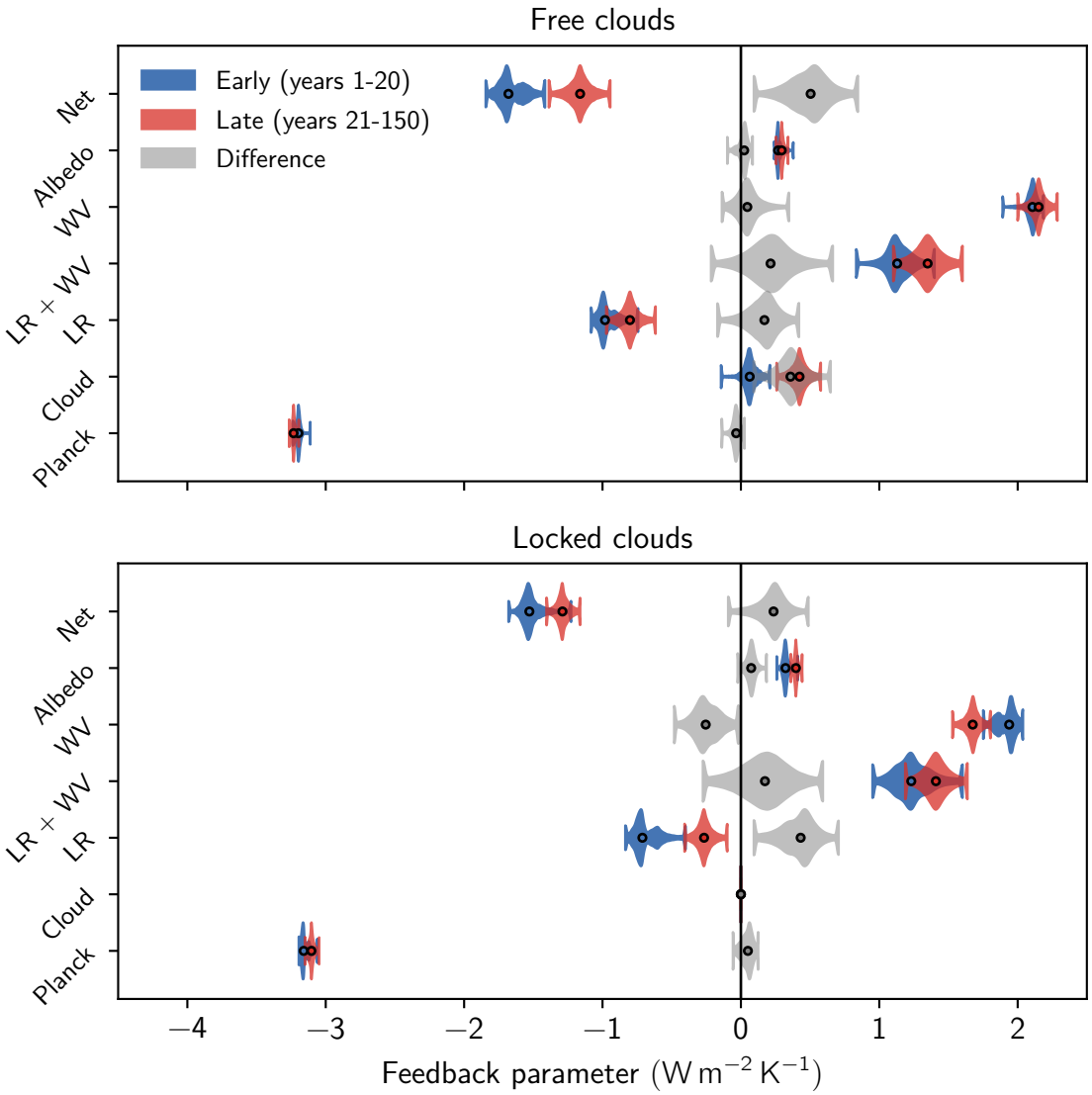

Figure 4.8: Feedback mechanisms in the free- and locked-cloud experiments. The diagrams show the shape of their probability distributions with the 5-95 percentile range and the median as a black dot. Blue distributions are the estimates using the early period (years 1-20). Red distributions come from the late period (years 21-150). Grey distributions are the difference between the late and the early periods. Top panel: Free-cloud case. Bottom panel: Locked-cloud case.

4.5). The lock-cloud case is shifted to more positive values in general, thereby explaining the weaker global lapse-rate feedback. Despite this shift, the lock-cloud northern tropical and middle latitudes behave in a similar way as in the free-cloud case. In contrast, the lock-cloud southern hemisphere presents the strongest differences between early and late periods, broadening the change in the lock-cloud global lapse-rate feedback between timescales. The strongest differences come from the Southern Ocean. Albeit a similar shift to weaker values as in the lapse-rate feedback case, the water-vapour feedback in the early period behaves in almost the same fashion between the free- and locked-cloud experiments outside the tropics (figure 4.4). During the late period, the difference in the southern tropics is striking: the free-cloud case presents a strongly positive peak at the equator, whereas the lock-cloud experiment shows no such peak and the southern tropical water-vapour feedback remains below the early period levels.

Synergy of clouds, lapse-rate and water-vapour feedback

The above-described features of the lapse-rate and water-vapour feedbacks are consistent with the weaker free-tropospheric warming that we presented in figure 4.7. Thus, the weaker lapse-rate and water-vapour feedbacks stem from the weaker tropical free-tropospheric warming. Therefore, evolving tropical clouds enhance warming, leading to stronger lapse-rate feedback. A warmer troposphere can also contain more water-vapour, enhancing the atmospheric absorptivity of infrared radiation in the tropics and, thereby compensating for the strengthened lapse-rate feedback. Although the difference between early and late periods in the combined lapse-rate plus water-vapour feedback does not appreciably change between locked- and free-cloud experiments, these results show the intricate role of the clouds in determining the combined feedback strength. The outstanding robustness of the combined feedback to whether or not clouds are present could be explained by state-dependencies. Other studies suggest that the water-vapour feedback is enhanced in warmer climates (e.g. Meraner et al. 2013; Popp et al. 2016). Since quadrupled CO_2 impose a sizeable forcing, we might be seeing such enhanced feedback in the course of our experiments. The compensation between lapse-rate and water-vapour feedbacks appears outstandingly robust to whether or not cloud changes are present, considering that it is almost equal between the locked- and free-cloud experiments, showing the intricate role of clouds in determining their strength.

Global Planck and surface-albedo feedbacks

Planck feedback decreases in magnitude between locked- and free-cloud experiments (figure 4.8). Prominently, the Planck feedback is weaker during the locked-cloud late period than during the early period, whereas in the free-cloud case occurs the converse (see also table S4.1). This reversal in the behaviour provides a positive difference in the locked-cloud Planck feedback between the early and late periods. This positive difference sums up to the positive difference provided by the surface-albedo feedback. The locked-cloud surface-albedo feedback not only becomes stronger than in the free-cloud case but also its difference between early and late periods becomes larger (figure 4.8). Therefore, Planck and surface-albedo feedback explain the rest of the difference that the lapse-rate and water-vapour feedbacks does not explain.

Zonally-averaged Planck and surface-albedo feedbacks

The zonally-averaged surface-albedo feedback behaves in a similar way between free- and locked-cloud experiments, as the main changes are in the high latitudes (figure 4.9). However, the magnitude of the changes explains the enhanced locked-cloud global surface-albedo feedback. With comparable magnitudes during the early and late periods, the southern high-latitude surface-albedo feedback is stronger than in the free-cloud case.

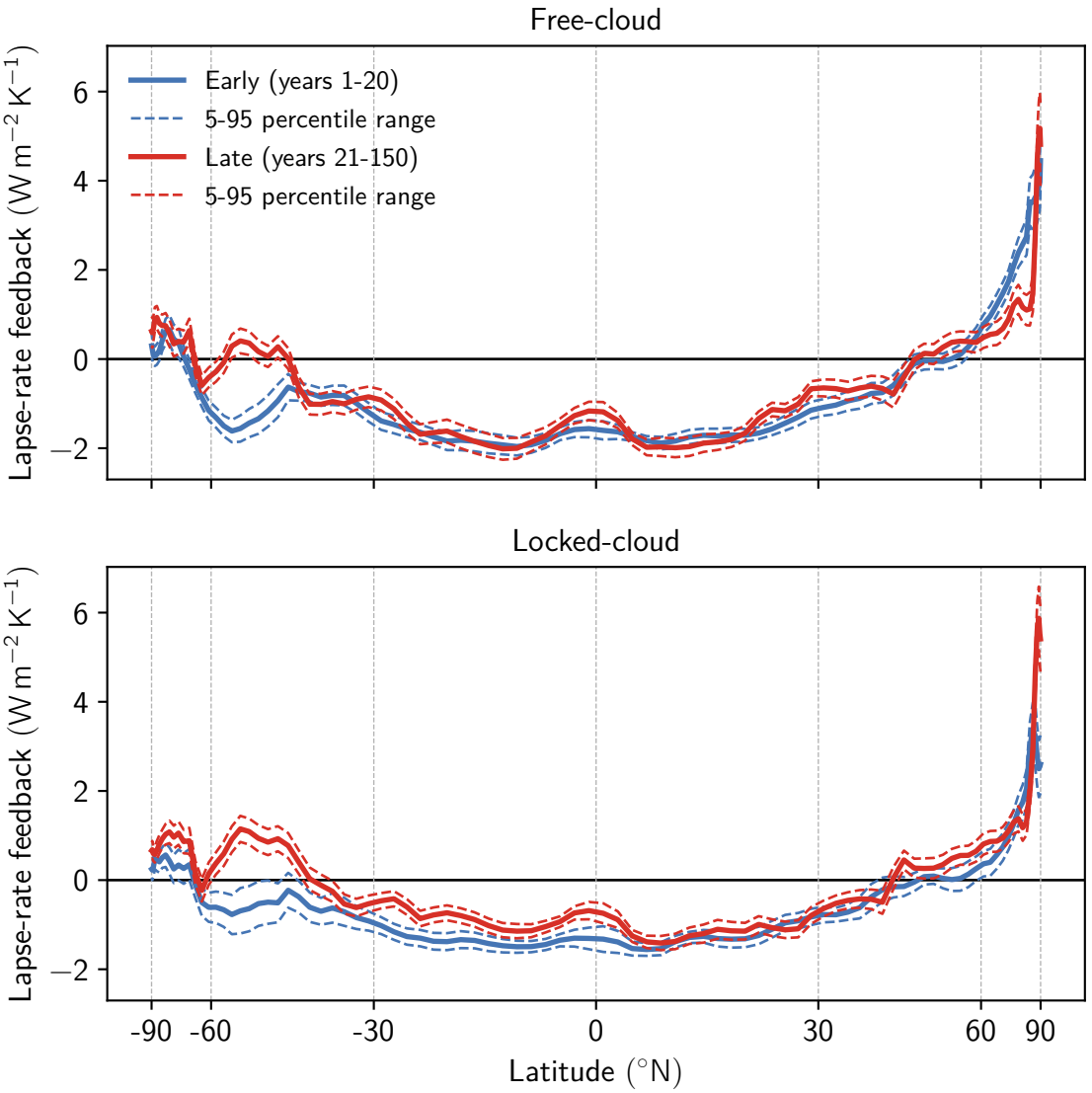

Figure 4.9: Lapse-rate feedback in free- and locked-cloud experiments. Zonal mean. Blue is the early period (years 1-20). Red is the late period (years 21-150). Dashed lines mark the 5-95 percentile range in the estimate of the feedback. Top panel: Free-cloud case. Bottom panel: Locked-cloud case.

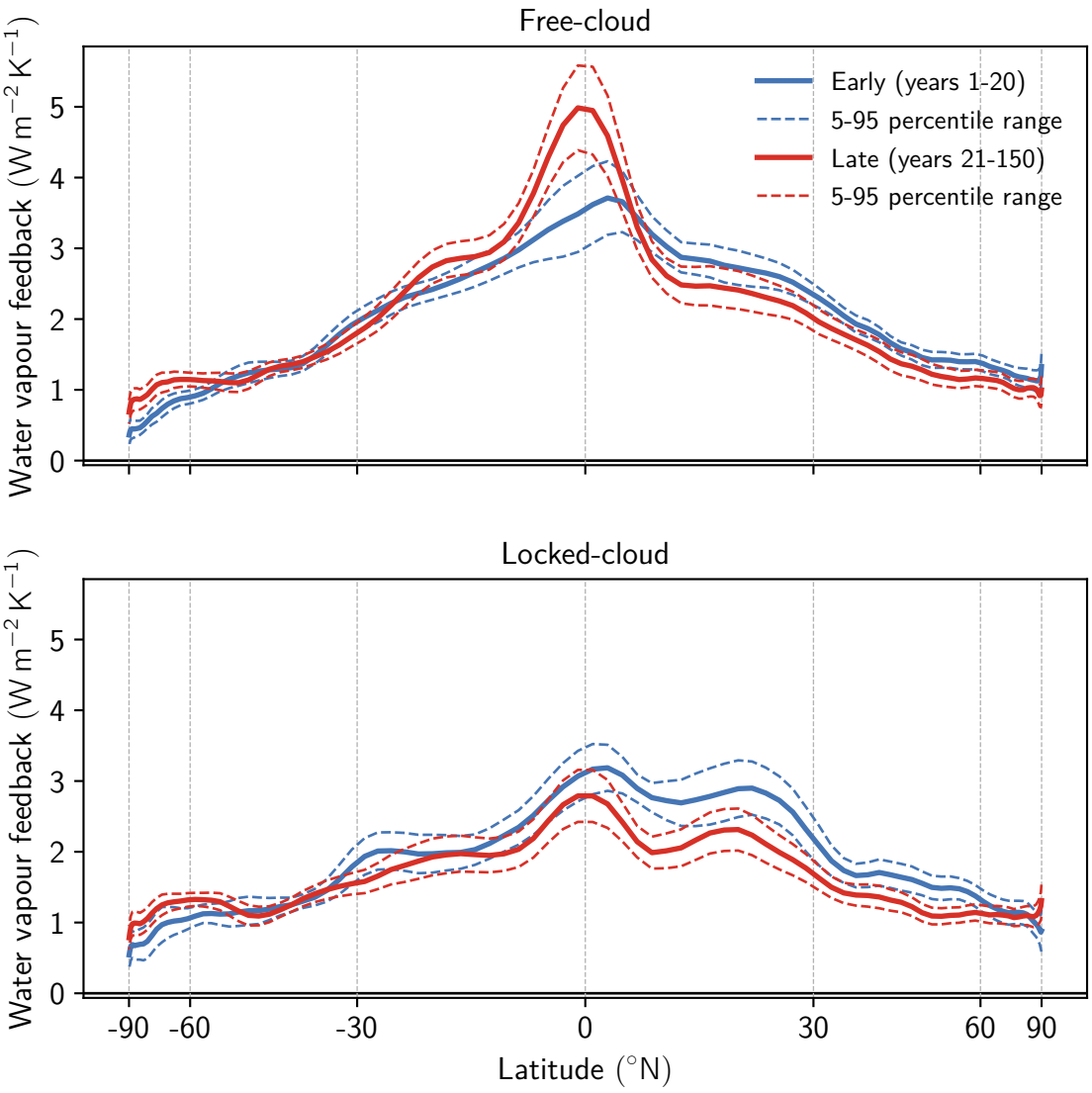

Figure 4.10: Water-vapour feedback in free- and locked-cloud experiments. Zonal mean. Blue is the early period (years 1-20). Red is the late period (years 21-150). Dashed lines mark the 5-95 percentile range in the estimate of the feedback. Top panel: Free-cloud case. Bottom panel: Locked-cloud case.

Albeit the locked-cloud Planck feedback shows a general shift to less negative values, the behaviour of the locked-cloud experiment stays in line with the free-cloud experiment (figure 4.10). However, the locked-cloud northern tropics present a stronger weakening between early and late periods than in the free-cloud experiment. In contrast to the free-cloud experiment, the lock-cloud Planck feedback substantially strengthens in the Southern Ocean and the southern high-latitudes. These high-latitude changes in the Planck and surface-albedo feedbacks are in line with the high-latitude changes in the lapse-rate feedback. Thus, the Southern Ocean possibly has the key to understand the remaining difference in the climate feedback parameter between the early and late periods.

4.6 Conclusions

We showed with a cloud-locking technique that clouds explain almost half of the difference in the climate feedback parameter λ between the early and late periods in the MPI-ESM1.2 model. In comparison to the free-cloud case, we detected reduced tropical free-tropospheric warming in the locked-cloud experiments. This reduced warming stems from non-rising tropical anvil clouds in the locked-cloud experiment, that possibly modified other feedback mechanisms such as water-vapour feedback, explaining the remaining difference. Therefore, we analysed the feedback mechanism contributions using the partial radiation perturbations technique. On the one hand, we found a weakened lapse-rate and water-vapour feedbacks: a result consistent with the reduced free-tropospheric warming. Locked clouds reduce the free-tropospheric warming in the tropics, thereby weakening the lapse-rate feedback. The reduced tropical free-tropospheric warming also decreases the amount of water vapour in the troposphere, thereby weakening the water-vapour feedback. On the other hand, the remaining changes in λ come from the high-latitude contributions of the surface-albedo and the Planck feedback, with particular emphasis in the Southern Ocean.

In summary, in the MPI-ESM1.2 model, we found that clouds are the most influential element that explains the variation of the climate feedback parameter in the `abrupt4xCO2` experiment. Cloud processes, in particular the rise of tropical anvil clouds with warming and their synergy with the lapse-rate feedback, produce the necessary tropical free-tropospheric warming that controls the stability in subsidence regions. Deep clouds warm the tropical free troposphere, responding to the evolving sea surface temperature pattern and induce a delay in the surface warming by enhancing shallow cloudiness in the trade regions.

4.7 Supplement

Feedback	Free ($W\,m^{-2}\,K^{-1}$)			Locked ($W\,m^{-2}\,K^{-1}$)		
	Early	Late	Difference	Early	Late	Difference
Planck	−3.20 (−3.24 to −3.11)	−3.23 (−3.26 to −3.19)	−0.03 (−0.14 to 0.03)	−3.16 (−3.19 to −3.06)	−3.10 (−3.15 to −3.05)	0.05 (−0.06 to 0.12)
Cloud	0.06 (−0.14 to 0.21)	0.42 (0.26 to 0.58)	0.36 (0.09 to 0.65)	0.00 (0.00 to 0.00)	0.00 (0.00 to 0.00)	0.00 (0.00 to 0.00)
LR	−0.98 (−1.08 to −0.74)	−0.80 (−0.97 to −0.62)	0.17 (−0.17 to 0.42)	−0.71 (−0.84 to −0.40)	−0.27 (−0.41 to −0.10)	0.43 (0.09 to 0.71)
LR + WV	1.13 (0.83 to 1.40)	1.35 (1.10 to 1.60)	0.21 (−0.21 to 0.67)	1.23 (0.95 to 1.60)	1.41 (1.19 to 1.64)	0.17 (−0.27 to 0.60)
WV	2.11 (1.89 to 2.19)	2.15 (2.00 to 2.29)	0.05 (−0.14 to 0.34)	1.94 (1.75 to 2.04)	1.68 (1.53 to 1.80)	−0.25 (−0.48 to −0.02)
Albedo	0.27 (0.24 to 0.38)	0.29 (0.26 to 0.34)	0.02 (−0.10 to 0.08)	0.32 (0.26 to 0.41)	0.40 (0.36 to 0.44)	0.07 (−0.02 to 0.19)
Net	−1.68 (−1.84 to −1.42)	−1.16 (−1.39 to −0.94)	0.50 (0.09 to 0.85)	−1.53 (−1.68 to −1.23)	−1.29 (−1.40 to −1.16)	0.24 (−0.09 to 0.48)

Table S4.1: Summary of the feedback mechanisms contribution. The 5-95 percentile range is given between parenthesis.

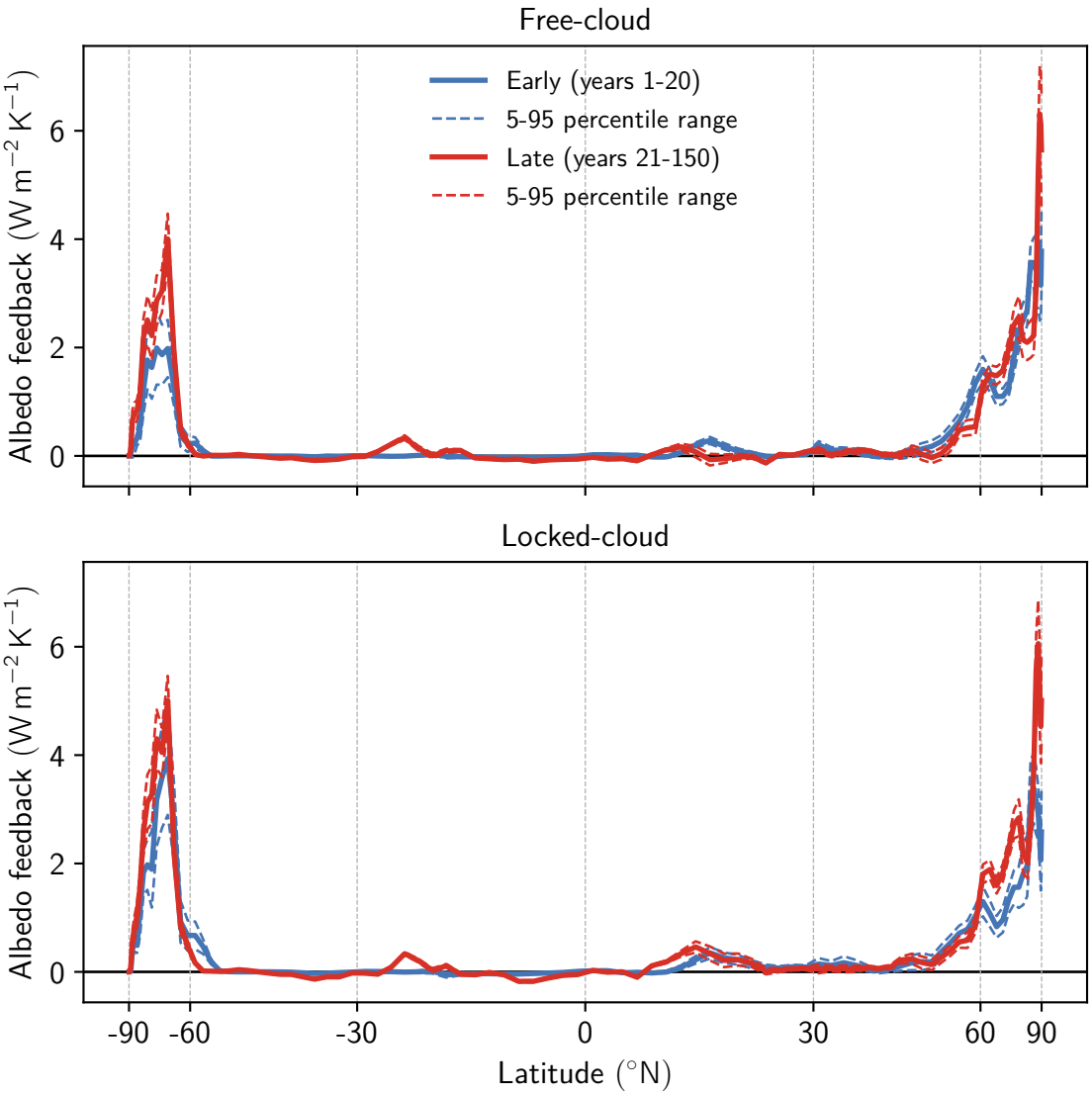

Figure S4.1: Surface-albedo feedback in free- and locked-cloud experiments. Zonal mean. Blue is the early period (years 1-20). Red is the late period (years 21-150). Dashed lines mark the 5-95 percentile range in the estimate of the feedback. Top panel: Free-cloud case. Bottom panel: Locked-cloud case.

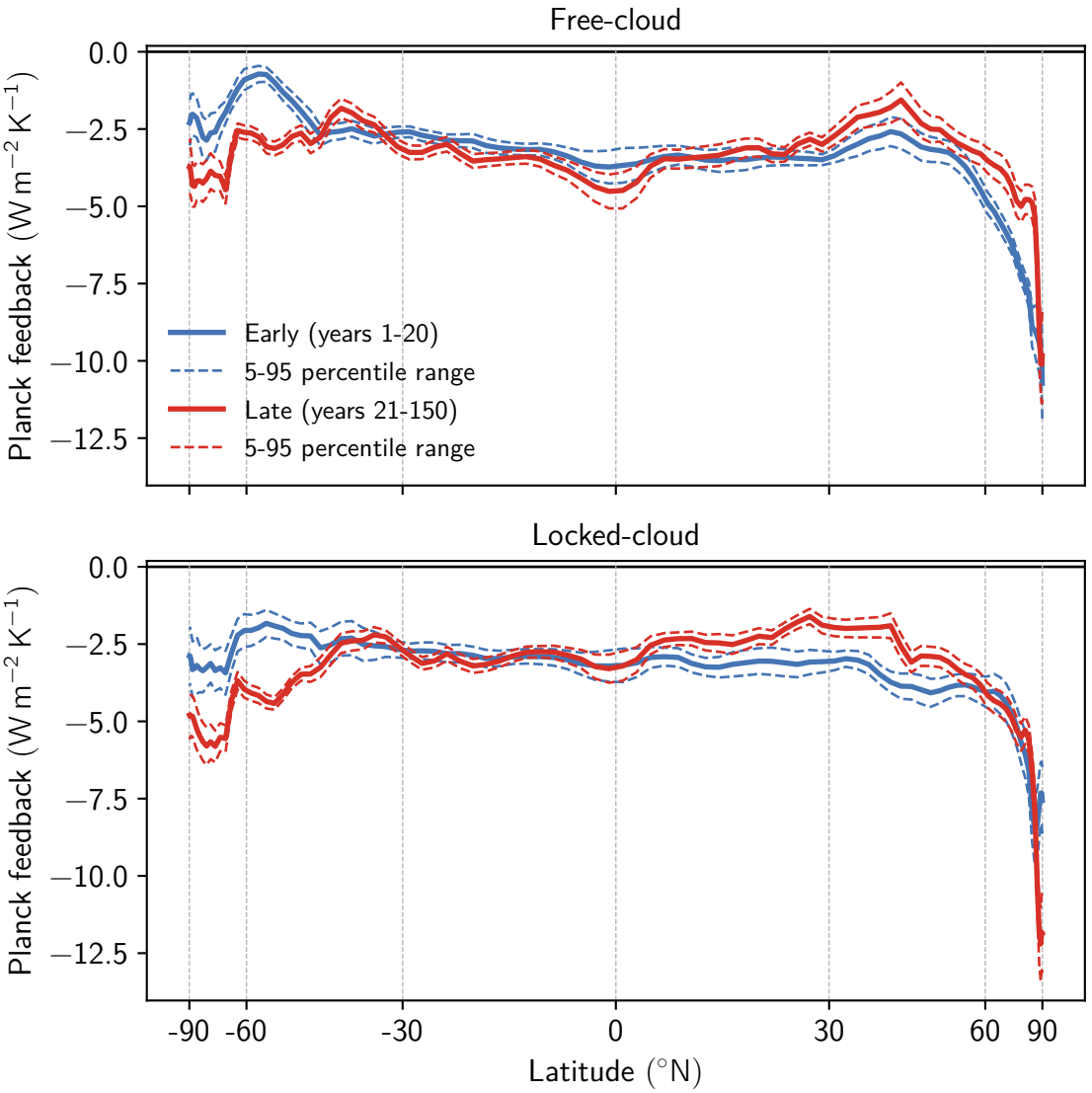

Figure S4.2: Planck feedback in free- and locked-cloud experiments. Zonal mean. Blue is the early period (years 1-20). Red is the late period (years 21-150). Dashed lines mark the 5-95 percentile range in the estimate of the feedback. Top panel: Free-cloud case. Bottom panel: Locked-cloud case.

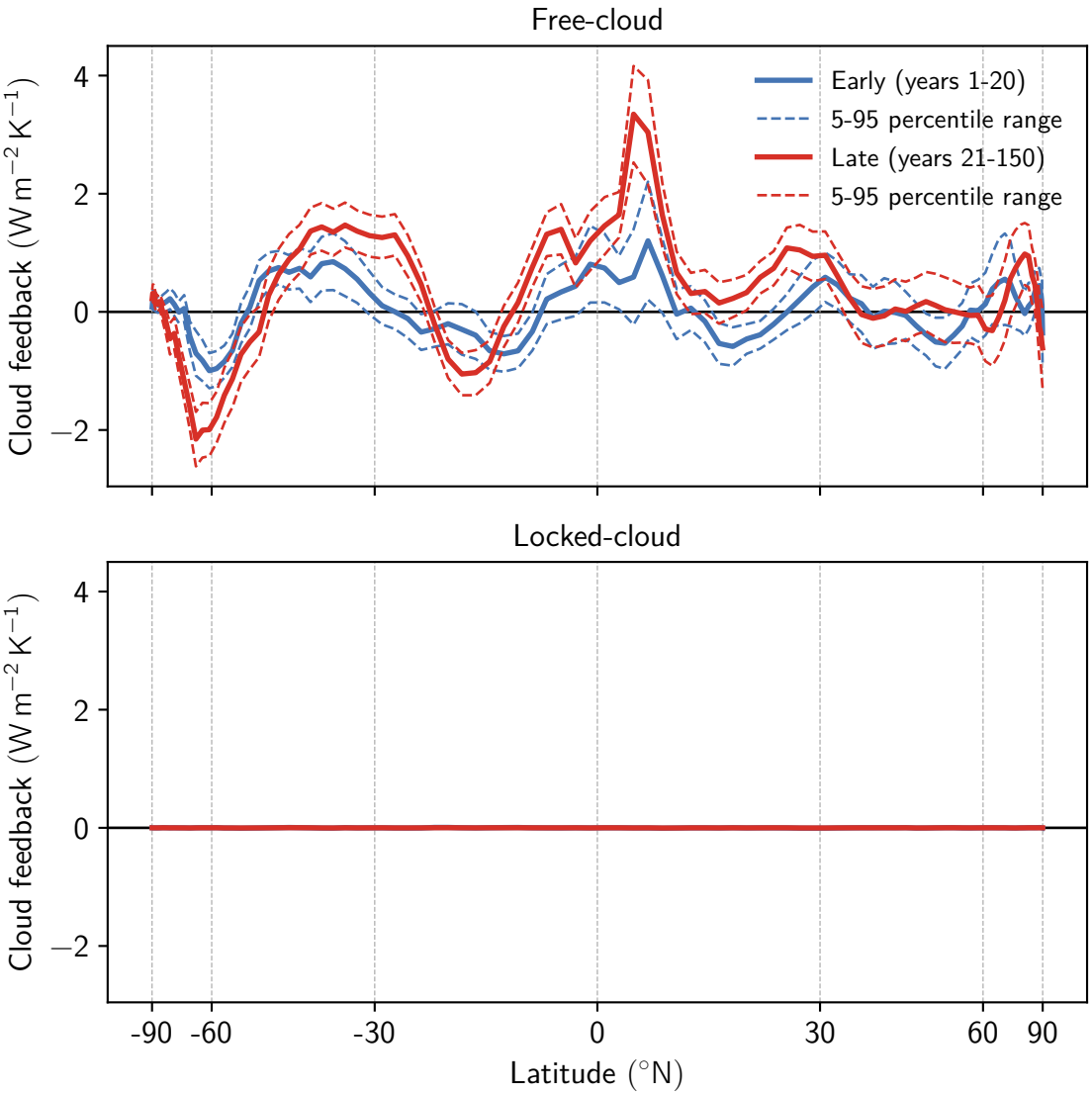

Figure S4.3: Cloud feedback in free- and locked-cloud experiments. Zonal mean. Blue is the early period (years 1-20). Red is the late period (years 21-150). Dashed lines mark the 5-95 percentile range in the estimate of the feedback. Top panel: Free-cloud case. Bottom panel: Locked-cloud case.

Discussion and Conclusion

I've seen things you people wouldn't believe. Attack ships on fire off the shoulder of Orion. I watched C-beams glitter in the dark near the Tannhäuser Gate. All those moments will be lost in time, like tears in rain. Time to die.

Roy Batty. Blade Runner. David W. Peoples and Rutger Hauer

Climate sensitivity indexes, such as TCR and ECS, provide a measure of the system response to forcing. Therefore, climate projections need precise estimates of climate sensitivity to finely determine the future effects of the present anthropogenic intervention on the climate system (Grose et al. 2018). Historical warming lets us obtain estimates of climate sensitivity. However, uncertainty in the anthropogenic aerosol forcing and the variations in the feedback mechanisms controlled by the evolving sea-surface temperature warming pattern difficult the interpretation of the historical warming in terms of climate sensitivity. Throughout this dissertation, we use simple physical concepts to shed light in complex model results. We refine the climate sensitivity estimates with the help of complex-modelling output by reducing the uncertainty and explaining the reduction on physical grounds. We also study the underlying physical mechanisms leading to the uncertainty in the long-term projections due to the evolving sea-surface temperature warming pattern.

We use in chapter 3 the popular multi-purpose method of emergent constraints to interpret the historical warming in terms of TCR and ECS. In essence, an emergent constraint is a statistical device. The idea is simple. We have two variables. One is observable. The other is complicated to measure, a model parameter or a modelled quantity. If we have an ensemble of models, then we can look for a statistical model that relates, in the ensemble, both quantities. If we find such a relationship, we can constrain the non-observable variable by using the observable quantity and the derived statistical relationship. Numerous studies use the emergent constraints and, therefore, there is an extensive discussion on its use (Klein and Hall 2015; Qu et al. 2018). In the case of TCR and ECS, studies have focused in two observables: clouds (Sherwood et al. 2014; Brient et al. 2016) and surface temperature change (Bender et al. 2010; Hargreaves et al. 2012; Hargreaves and Annan 2016; Renoult et al. 2020). As with any statistical technique, one should be careful: statistical relationships do not guarantee real physical relationships (Caldwell et al. 2014). Our study uses the conceptual framework (chapter 2) as a basis for the emergent constraints on TCR and ECS. Thus, we duly solved one of the caveats of the emergent constraints framework. We are only limited by the validity of the approximations made to construct the conceptual models.

The more constant anthropogenic aerosol forcing during the post-1970s period suggest that the analysis of the warming during this period can improve the estimates of TCR and ECS. We interpret the relationships of the post-1970s warming and climate sensitivity

as modelled in the CMIP5 ensemble. The CMIP5-based relationship between post-1970s warming and TCR shows a better agreement with the analogous relationship derived from the two-layer model (figure 3.1, panel a). The better agreement with the two-layer model indicates that the upper ocean is not close to the frequently assumed steady-state (zero-layer approximation) during the post-1970s period. Instead, during this period the upper ocean buffers part of the forcing. This buffering is not unthinkable, given that a significant fraction of the anthropogenic forcing has been applied after 1970 (figure 1.1). Thus, because more complex climate models also simulate this buffering, when using the CMIP5-based relationship between warming and TCR as an emergent constraint on TCR, our TCR estimate is higher than the usual estimates using the zero-layer approximation. Furthermore, the likelihood of lower TCRs is substantially reduced not only because the aerosol forcing is more certain during the post-1970s period, but also because we consider the upper-ocean energy storage. Hence, we used basic physical understanding to appreciate the underlying cause of the reduction in the uncertainty and an increment in the TCR estimate. Our results (Jiménez-de-la-Cuesta and Mauritsen 2019) have been confirmed to hold also for the CMIP6 ensemble in a recent paper under public discussion by Nijsse et al. (2020), where they derive the emergent constraint instead using Bayesian methods.

The analogous relationship between post-1970s warming and ECS shows another use of the conceptual framework. Although here the emergent constraint on ECS using the observed warming is not as successful as in the TCR case, we also show that the usual zero-layer approximation fails to represent the model behaviour. CMIP5 behaviour is also closer to the relationship derived from the two-layer model, which includes the sea-surface temperature pattern effect (figure 3.1, panel b). Then here we find another cue that confirms the field's course: towards understanding the influence of the atmosphere-ocean interactions. We opted to follow the course, and then the research of chapter 4 began. We find that not only clouds have a substantial role in the sea-surface temperature pattern effect, but also the evolving tropical clouds provide the necessary tropical free-tropospheric warming that fuels the mechanism presented by (Zhou et al. 2016). Thus, we find that tropical clouds substantially control the trade stratocumuli, which are central to delay the surface warming (Zhou et al. 2016; Ceppi and Gregory 2017; Mauritsen 2016). Given that a sizeable amount of the remaining non-cloud sea-surface temperature pattern effect comes from the lapse-rate and water-vapour feedback mechanisms, the robust quasi-constancy of the sum of their strengths and that other studies indicate an enhancement of the water-vapour feedback mechanism in warmer climates (Meraner et al. 2013; Popp et al. 2016); we ought to ask if this remaining non-cloud sea-surface temperature pattern effect comes from state-dependency. Moreover, this highlights the essential and intricate role of cloud processes and cloud feedback in the determination of climate sensitivity.

Bibliography

Fourier, J.-B. J. (1827). "Mémoire sur les Températures du Globe Terrestre et des Espaces Planétaires". *Mémoires d lAcadémie Royale des Sciences de lInstitute de France* 7, pp. 570–604.

Tyndall, J. (1861). "On the Absorption and Radiation of Heat by Gases and Vapours, and on the Physical Connexion of Radiation, Absorption, and Conduction". *Philosophical Transactions of the Royal Society of London* 151, pp. 1–36.

Arrhenius, S. (1896). "On the Influence of Carbonic Acid in the Air upon the Temperature of the Ground". *Philosophical Magazine and Journal of Science* 41, pp. 237–276.

Callendar, G. S. (1938). "The artificial production of carbon dioxide and its influence on temperature". *Quarterly Journal of the Royal Meteorological Society* 64(275), pp. 223–240.

IPCC (2013a). "Annex II: Climate System Scenario Tables". *Climate Change 2013: The Physical Science Basis. Contribution of Working Group I to the Fifth Assessment Report of the Intergovernmental Panel on Climate Change*. Ed. by T. F. Stocker, D. Qin, G.-K. Plattner, M. M. B. Tignor, S. K. Allen, J. Boschung, A. Nauels, Y. Xia, V. Bex, and P. M. Midgley. Cambridge University Press. Chap. AII, pp. 1395–1446.

Cowtan, K. and R. G. Way (2014). "Coverage bias in the HadCRUT4 temperature series and its impact on recent temperature trends". *Quarterly Journal of the Royal Meteorological Society* 140(683), pp. 1935–1944.

Trenberth, K. E., J. T. Fasullo, and J. Kiehl (2009). "Earth's Global Energy Budget". *Bulletin of the American Meteorological Society* 90(3), pp. 311–324.

Sherwood, S. C., S. Bony, O. Boucher, C. Bretherton, P. M. Forster, J. M. Gregory, and B. Stevens (2015). "Adjustments in the Forcing-Feedback Framework for Understanding Climate Change". *Bulletin of the American Meteorological Society* 96(2), pp. 217–228.

Held, I. M. and B. J. Soden (2006). "Robust Responses of the Hydrological Cycle to Global Warming". *Journal of Climate* 19(21), pp. 5686–5699.

Lambert, F. H. and M. J. Webb (2008). "Dependency of global mean precipitation on surface temperature". *Geophysical Research Letters* 35(16), p. L16706.

Hansen, J. E., R. A. Ruedy, M. Sato, and K.-W. K. Lo (2010). "Global surface temperature change". *Reviews of Geophysics* 48(4), RG4004.

Otto, A., F. E. L. Otto, O. Boucher, J. Church, G. Hegerl, P. M. Forster, N. P. Gillet, J. M. Gregory, G. C. Johnson, R. Knutti, N. Lewis, U. Lohmann, J. Marotzke, G. Myhre, D. Shindell, B. Stevens, and M. R. Allen (2013). "Energy budget constraints on climate response". *Nature Geoscience* 6(6), pp. 415–416.

Mauritsen, T. and R. Pincus (2017). "Committed warming inferred from observations". *Nature Climate Change* 7(9), pp. 652–655.

Gregory, J. M. and P. M. Forster (2008). "Transient Climate Response Estimated from Radiative Forcing and Observed Temperature Change". *Journal of Geophysical Research: Atmospheres* 113(D23), p. D23105.

Gregory, J. M., W. J. Ingram, M. A. Palmer, G. S. Jones, P. A. Stott, R. B. Thorpe, J. A. Lowe, T. C. Johns, and K. D. Williams (2004). "A new method for diagnosing radiative forcing and climate sensitivity". *Geophysical Research Letters* 31(3), p. L03205.

Gregory, J. M., R. J. Stouffer, S. C. B. Raper, P. A. Stott, and N. A. Rayner (2002). "An Observationally Based Estimate of the Climate Sensitivity". *Journal of Climate* 15(22), pp. 3117–3121.

Lewis, N. and J. A. Curry (2014). "The implications for climate sensitivity of AR5 forcing and heat uptake estimates". *Climate Dynamics* 45(3–4), pp. 1009–1023.

IPCC (2013b). "Chapter 8: Anthropogenic and Natural Radiative Forcing". *Climate Change 2013: The Physical Science Basis. Contribution of Working Group I to the Fifth Assessment Report of the Intergovernmental Panel on Climate Change*. Ed. by G. Myhre, D. Shindell, F.-M. Breón, W. Collins, J. Fuglestvedt, J. Huang, D. Koch, J.-F. Lamarque, D. Lee, B. Mendoza, T. Nakajima, A. Robock, G. Stephens, T. Takemura, and H. Zhang. Cambridge University Press. Chap. 8, pp. 659–740.

Smith, S. J., J. van Aardenne, Z. Klimont, R. J. Andres, A. Volke, and S. Delgado Arias (2011). "Anthropogenic sulfur dioxide emissions: 18502005". *Atmospheric Chemistry and Physics* 11(3), pp. 1101–1116.

Stevens, B. (2015). "Rethinking the Lower Bound on Aerosol Radiative Forcing". *Journal of Climate* 28(12), pp. 4794–4819.

Fiedler, S., B. Stevens, and T. Mauritsen (2017). "On the sensitivity of anthropogenic aerosol forcing to modelinternal variability and parameterizing a Twomey effect". *Journal of Advances in Modeling Earth Systems* 9(2), pp. 1325–1341.

Loeb, N. A., B. A. Wielicki, D. R. Doellingast, G. L. Smith, D. F. Keyes, S. K. Kato, N. Manalo-Smith, and T. Wong (2009). "Toward Optimal Closure of the Earth's Top-of-Atmosphere Radiation Budget". *Journal of Climate* 22(3), pp. 748–766.

Levitus, S., J. Antonov, T. Boyer, O. Baranova, H. Garcia, R. Locarnini, A. Mishonov, J. Reagan, D. Seidov, E. Yarosh, and M. Zweng (2012). "World ocean heat content and thermosteric sea level change (0–2000 m), 1955–2010". *Geophysical Research Letters* 39(10), p. L10603.

Trenberth, K. E. and M. A. Balmaseda (2014). "Earth's Energy Imbalance". *Journal of Climate* 27(9), pp. 3129–3144.

Zanna, L., S. Khatiwala, J. M. Gregory, J. Ison, and H. Patrick (2019). "Global reconstruction of historical ocean heat storage and transport". *Proceedings of the National Academy of Sciences* 116(4), pp. 1126–1131.

Resplandy, L., R. Keeling, Y. Eddebbar, M. Brooks, R. Wang, L. Bopp, M. Long, J. Dunne, W. Koeve, and A. Oschlies (2014). "Quantification of ocean heat uptake from changes in atmospheric O2 and CO2 composition". *Nature* 563(7729), pp. 105–108.

Johnson, G. C., J. M. Lyman, and N. G. Loeb (2016). "Improving estimates of Earth's energy imbalance". *Nature Climate Change* 6(7), pp. 639–640.

Good, P., J. A. Lowe, T. Andrews, A. Wiltshire, R. Chadwick, J. K. Ridley, M. B. Menary, N. Bouttes, J. L. Dufresne, J. M. Gregory, N. Schaller, and H. Shiogama (2015). "Nonlinear

regional warming with increasing CO2 concentrations". *Nature Climate Change* 5(2), pp. 138–142.

Gregory, J. M., T. Andrews, and P. Good (2015). "The inconstancy of the transient climate response parameter under increasing CO_2". *Philosophical Transactions of the Royal Society A* 373(2054), p. 20140417.

Armour, K. C. (2017). "Energy budget constraints on climate sensitivity in light of inconstant climate feedbacks". *Nature Climate Change* 7(5), pp. 331–335.

Zhou, C., M. D. Zelinka, and S. A. Klein (2016). "Impact of decadal cloud variations on the Earths energy budget". *Nature Geoscience* 9(12), pp. 871–874.

Ceppi, P. and J. M. Gregory (2017). "Relationship of tropospheric stability to climate sensitivity and Earths observed radiation budget". *Proceedings of the National Academy of Sciences* 114(50), pp. 13126–13131.

Box, G. E. (1976). "Science and Statistics". *Journal of the American Statistical Association* 71(356), pp. 791–799.

Mauritsen, T., B. Stevens, E. Roeckner, T. Crueger, M. Esch, M. Giorgetta, H. Haak, J. Jungclaus, D. Klocke, D. Matei, U. Mikolajewicz, D. Notz, R. Pincus, S. Hauke, and L. Tomassini (2012). "Tuning the climate of a global model". *Journal of Advances in Modeling Earth Systems* 4(3), M00a01.

Mauritsen, T., J. Bader, T. Becker, J. Behrens, M. Bittner, R. Brokopf, V. Brovkin, M. Claussen, T. Crueger, M. Esch, I. Fast, S. Fiedler, D. Fläschner, V. Gayler, M. Giorgetta, D. S. Goll, H. Haak, S. Hagemann, C. Hedemann, C. Hohenegger, T. Ilyina, T. Jahns, D. Jiménez-de-la-Cuesta, J. Jungclaus, T. Kleinen, S. Kloster, D. Kracher, S. Kinne, D. Kleberg, G. Lasslop, L. Kornblueh, J. Marotzke, D. Matei, K. Meraner, U. Mikolajewicz, K. Modali, B. Möbis, W. A. Müller, J. E. M. S. Nabel, C. C. W. Nam, D. Notz, S.-S. Nyawira, H. Paulsen, K. Peters, R. Pincus, H. Pohlmann, J. Pongratz, M. Popp, T. J. Raddatz, S. Rast, R. Redler, C. H. Reick, T. Rohrschneider, V. Schemann, H. Schmidt, R. Schnur, U. Schulzweida, K. D. Six, L. Stein, I. Stemmler, B. Stevens, J.-S. von Storch, F. Tian, A. Voigt, P. Vrese, K.-H. Wieners, S. Wilkenskjeld, A. Winkler, and E. Roeckner (2019). "Developments in the MPI-M Earth System Model version 1.2 (MPI-ESM1.2) and its response to increasing CO_2". *Journal of Advances in Modeling Earth Systems* 11(4), pp. 998–1038.

Mauritsen, T., R. G. Graversen, D. Klocke, P. L. Langen, B. Stevens, and L. Tomassini (2013). "Climate feedback efficiency and synergy". *Climate Dynamics* 41(9-10), pp. 2539–2554.

Manabe, S. and R. F. Strickler (1964). "Thermal Equilibrium of the Atmosphere with a Convective Adjustment". *Journal of the Atmospheric Sciences* 21(4), pp. 361–385.

Budyko, M. (1969). "The effect of solar radiation variations on the climate of the Earth". *Tellus* 21(5), pp. 611–619.

Held, I. M., M. Winton, K. Takahashi, T. Delworth, F. Zeng, and G. K. Vallis (2010). "Probing the Fast and Slow Components of Global Warming by Returning Abruptly to Preindustrial Forcing". *Journal of Climate* 23(9), pp. 2418–2427.

Dacie, S., L. Kluft, H. Schmidt, B. Stevens, S. A. Buehler, P. J. Nowack, S. Dietmüller, N. L. Abraham, and T. Birner (2019). "A 1D RCE Study of Factors Affecting the Tropical Tropopause Layer and Surface Climate". *Journal of Climate* 32(20), pp. 6769–6782.

Kluft, L. and S. Dacie (2019). "Re-Examining the First Climate Models: Climate Sensitivity of a Modern RadiativeConvective Equilibrium Model". *Journal of Climate* 32(23), pp. 8111–8125.

Rohrschneider, T., B. Stevens, and T. Mauritsen (2019). "On simple representations of the climate response to external radiative forcing". *Climate Dynamics* 3(5-6), pp. 3131–3145.

Jiménez-de-la-Cuesta, D. and T. Mauritsen (2019). "Emergent constraints on Earth's transient and equilibrium response to doubled CO_2 from post-1970s warming". *Nature Geoscience* 12(11), pp. 902–905.

Hasselmann, K. (1976). "Stochastic climate models Part I. Theory". *Tellus* 28(6), pp. 473–485.

Lunt, D. J., A. M. Haywood, G. A. Schmidt, U. Salzmann, P. J. Valdes, and H. J. Dowsett (2010). "Emergent constraints on Earth's transient and equilibrium response to doubled CO_2 from post-1970s warming". *Nature Geoscience* 3(1), pp. 60–64.

Geoffroy, O., D. Saint-Martin, D. J. L. Olivié, A. Voldoire, G. Bellon, and S. Tytéca (2013a). "Transient Climate Response in a Two-Layer Energy-Balance Model. Part I: Analytical Solution and Parameter Calibration Using CMIP5 AOGCM Experiments". *Journal of Climate* 26(6), pp. 1841–1857.

Senior, C. A. and J. F. B. Mitchell (2000). "The timedependence of climate sensitivity". *Geophysical Research Letters* 27(17), pp. 2685–2688.

Voss, R. and U. Mikolajewicz (2001). "Long-term climate changes due to increased CO2 concentration in the coupled atmosphere-ocean general circulation model ECHAM3/LSG". *Climate Dynamics* 17(1), pp. 45–60.

Colman, R. A. and B. J. McAvaney (2009). "Climate feedbacks under a very broad range of forcing". *Geophysical Research Letters* 36(1), p. L01702.

Caballero, R. and M. Huber (2013). "State-dependent climate sensitivity in past warm climates and its implications for future climate projections". *Proceedings of the National Academy of Sciences* 110(35), pp. 14162–14167.

Jonko, A. K., K. M. Shell, B. M. Sanderson, and G. Danabasoglu (2013). "Climate Feedbacks in CCSM3 under Changing CO2 Forcing. Part II: Variation of Climate Feedbacks and Sensitivity with Forcing". *Journal of Climate* 26(9), pp. 2784–2795.

Block, K. and T. Mauritsen (2013). "Forcing and feedback in the MPIESMLR coupled model under abruptly quadrupled CO2". *Journal of Advances in Modeling Earth Systems* 5(4), pp. 676–691.

Meraner, K., T. Mauritsen, and A. Voigt (2013). "Robust increase in equilibrium climate sensitivity under global warming". *Geophysical Research Letters* 40(2), pp. 5944–5948.

Andrews, T., J. M. Gregory, and M. J. Webb (2015). "The Dependence of Radiative Forcing and Feedback on Evolving Patterns of Surface Temperature Change in Climate Models". *Journal of Climate* 28(4), pp. 1630–1648.

Winton, M., K. Takahashi, and I. M. Held (2010). "Importance of Ocean Heat Uptake Efficacy to Transient Climate Change". *Journal of Climate* 23(9), pp. 2333–2344.

Armour, K. C., C. M. Bitz, and G. H. Roe (2013). "Time-Varying Climate Sensitivity from Regional Feedbacks". *Journal of Climate* 26(13), pp. 4518–4534.

Geoffroy, O., D. Saint-Martin, G. Bellon, A. Voldoire, D. J. L. Olivié, and S. Tytéca (2013b). "Transient Climate Response in a Two-Layer Energy-Balance Model. Part II:

Representation of the Efficacy of Deep-Ocean Heat Uptake and Validation for CMIP5 AOGCMs". *Journal of Climate* 26(6), pp. 1859–1876.

Hawkins, E. and R. Sutton (2009). "The Potential to Narrow Uncertainty in Regional Climate Predictions". *Bulletin of the American Meteorological Society* 90(8), pp. 1095–1107.

Grose, M. R., J. Gregory, R. Colman, and T. Andrews (2018). "What Climate Sensitivity Index Is Most Useful for Projections?" *Geophysical Research Letters* 45(3), pp. 1559–1566.

Rohling, E. J., A. Sluijs, H. A. Dijkstra, P. Köhler, R. S. W. van de Wal, A. S. von der Heydt, D. J. Beerling, A. Berger, P. K. Bijl, M. Crucifix, R. DeConto, S. S. Drijfhout, A. Fedorov, G. L. Foster, A. Ganopolski, J. Hansen, B. Hönisch, H. Hooghiemstra, M. Huber, P. Huybers, R. Knutti, D. W. Lea, L. J. Lourens, D. Lunt, V. Masson-Delmotte, M. Medina-Elizalde, B. Otto-Bliesner, M. Pagani, H. Pälike, H. Renssen, D. L. Royer, M. Siddall, P. Valdes, J. C. Zachos, and R. E. Zeebe (2012). "Making sense of palaeoclimate sensitivity". *Nature* 491(7426), pp. 683–691.

Andrews, T., J. M. Gregory, D. Paynter, L. G. Silvers, C. Zhu, T. Mauritsen, M. J. Webb, K. Armour, P. M. Forster, and H. Tichner (2018). "Accounting for Changing Temperature Patterns Increases Historical Estimates of Climate Sensitivity". *Geophysical Research Letters* 45(16), pp. 8490–8499.

Kiehl, J. (2007). "Twentieth century climate model response and climate sensitivity". *Geophysical Research Letters* 34(22), p. L22710.

Bengtsson, L. and S. E. Schwartz (2013). "Determination of a lower bound on Earth's climate sensitivity". *Tellus B: Chemical and Physical Meteorology* 65(1), p. 21533.

Forster, P. M., T. Andrews, P. Good, J. M. Gregory, L. S. Jackson, and M. Zelinka (2013). "Evaluating adjusted forcing and model spread for historical and future scenarios in the CMIP5 generation of climate models". *Journal of Geophysical Research: Atmospheres* 118(3), pp. 1139–1150.

Gregory, J. M., T. Andrews, P. Good, T. Mauritsen, and P. M. Forster (2016). "Small global-mean cooling due to volcanic radiative forcing". *Climate Dynamics* 47(12), pp. 3979–3991.

Shindell, D. T., J.-F. Lamarque, M. Schulz, M. Flanner, C. Jiao, M. Chin, P. J. Young, Y. H. Lee, L. Rotstayn, N. Mahowald, G. Milly, G. Faluvegi, Y. Balkanski, W. J. Collins, A. J. Conley, S. Dalsoren, R. Easter, S. Ghan, L. Horowitz, X. Liu, G. Myhre, T. Nagashima, V. Naik, S. T. Rumbold, R. Skeie, K. Sudo, S. Szopa, T. Takemura, A. Voulgarakis, J.-H. Yoon, and F. Lo (2011). "Radiative forcing in the ACCMIP historical and future climate simulations". *Atmospheric Chemistry and Physics* 13(6), pp. 2939–2974.

Regayre, L. A., K. J. Pringle, B. B. B. Booth, L. A. Lee, G. W. Mann, J. Browse, M. T. Woodhouse, A. Rap, C. L. Reddington, and K. S. Carslaw (2014). "Uncertainty in the magnitude of aerosolcloud radiative forcing over recent decades". *Geophysical Research Letters* 41(24), pp. 9040–9049.

Zhao, M., J.-C. Golaz, I. M. Held, H. Guo, V. Balaji, R. Benson, J.-H. Chen, X. Chen, L. J. Donner, J. P. Dunne, K. Dunne, J. Durachta, S.-M. Fan, S. M. Freidenreich, S. T. Garner, P. Ginoux, L. M. Harris, L. W. Horowitz, J. P. Krasting, A. R. Langenhorst, Z. Liang, P. Lin, S.-J. Lin, S. L. Malyshev, E. Mason, P. C. D. Milly, Y. Ming, V. Naik, F. Paulot, D. Paynter, P. Phillipps, A. Radhakrishnan, V. Ramaswamy, T. Robinson,

D. Schwarzkopf, C. J. Seman, E. Shevliakova, Z. Shen, H. Shin, L. G. Silvers, J. R. Wilson, M. Winton, A. T. Wittenberg, B. Wyman, and B. Xiang (2018). "The GFDL Global Atmosphere and Land Model AM4.0/LM4.0: 1. Simulation Characteristics With Prescribed SSTs". *Journal of Advances in Modeling Earth Systems* 10(3), pp. 691–734.

Hansen, J. E., G. Russell, A. Lacis, I. Fung, D. Rind, and P. Stone (1985). "Climate Response Times: Dependence on Climate Sensitivity and Ocean Mixing". *Science* 229(4716), pp. 857–859.

Morice, C. P., J. J. Kennedy, and N. A. Rayner (2012). "Quantifying uncertainties in global and regional temperature change using an ensemble of observational estimates: The HadCRUT4 data set". *Journal of Geophysical Research: Atmospheres* 117(D8), p. D08101.

Vose, R. S., D. Arndt, V. F. Banzon, D. R. Easterling, B. Gleason, B. Huang, E. Kearns, J. H. Lawrimore, M. J. Menne, T. C. Peterson, R. W. Reynolds, T. M. Smith, C. N. J. Williams, and D. B. Wuertz (2012). "NOAA's Merged LandOcean Surface Temperature Analysis". *Bulletin of the American Meteorological Society* 93(11), pp. 1677–1685.

Rohde, R., R. A. Muller, R. Jacobsen, E. Muller, S. Perlmutter, A. Rosenfeld, J. Wurtele, D. Groom, and C. Wickham (2013). "A New Estimate of the Average Earth Surface Land Temperature Spanning 1753 to 2011". *Geoinformatics & Geostatistics: An Overview* 1(1).

Andrews, T., J. M. Gregory, M. J. Webb, and K. E. Taylor (2012). "Forcing, feedbacks and climate sensitivity in CMIP5 coupled atmosphere-ocean climate models". *Geophysical Research Letters* 39(9), p. L09712.

Boggs, P. T., R. H. Byrd, and R. B. Schnabel (1987). "A Stable and Efficient Algorithm for Nonlinear Orthogonal Distance Regression". *SIAM Journal on Scientific and Statistical Computing* 8(6), pp. 1052–1078.

Sherwood, S. C., S. Bony, and J.-L. Dufresne (2014). "Spread in model climate sensitivity traced to atmospheric convective mixing". *Nature* 505(7481), pp. 37–42.

Brient, F., T. Schneider, Z. Tan, S. Bony, X. Qu, and A. Hall (2016). "Shallowness of tropical low clouds as a predictor of climate models response to warming". *Climate Dynamics* 47(1–2), pp. 433–449.

Stevens, B., S. Fiedler, S. Kinne, K. Peters, S. Rast, J. Müssel, S. J. Smith, and T. Mauritsen (2017). "MACv2-SP: a parameterization of anthropogenic aerosol optical properties and an associated Twomey effect for use in CMIP6". *Geoscientific Model Development* 10(1), pp. 433–452.

Schlesinger, M. E. and J. F. B. Mitchell (1987). "Climate Model Simulations of the Equilibrium Climatic Response to Increased Carbon Dioxide". *Reviews of Geophysics* 25(4), pp. 760–798.

Mauritsen, T. (2016). "Clouds cooled the Earth". *Nature Geoscience* 9(12), pp. 865–867.

Wetherald, R. T. and S. Manabe (1988). "Cloud Feedback Processes in a General Circulation Model". *Journal of the Atmospheric Sciences* 45(8), pp. 1397–1416.

Rädel, G., T. Mauritsen, B. Stevens, D. Dommenget, D. Matei, B. Katinka, and A. Clement (2016). "Amplification of El Niño by cloud longwave coupling to atmospheric circulation". *Nature Geoscience* 9(2), pp. 106–110.

Middlemas, E. A., A. C. Clement, B. Medeiros, and B. Kirtman (2019). "Cloud Radiative Feedbacks and El NiñoSouthern Oscillation". *Journal of Climate* 32(15), pp. 4661–4680.

Grise, K. M., B. Medeiros, J. J. Benedict, and J. G. Olson (2019). "Investigating the Influence of Cloud Radiative Effects on the Extratropical Storm Tracks". *Geophysical Research Letters* 46(13), pp. 7700–7707.

Hall, A. and S. Manabe (1999). "The Role of Water Vapor Feedback in Unperturbed Climate Variability and Global Warming". *Journal of Climate* 12(8), pp. 2327–2346.

Hall, A. (2004). "The Role of Surface Albedo Feedback in Climate". *Journal of Climate* 17(7), pp. 1550–1568.

Graversen, R. G. and M. Wang (2009). "Polar amplification in a coupled climate model with locked albedo". *Climate Dynamics* 3(5), pp. 629–643.

Langen, P. L., R. G. Graversen, and T. Mauritsen (2012). "Separation of Contributions from Radiative Feedbacks to Polar Amplification on an Aquaplanet". *Journal of Climate* 25(8), pp. 3010–3024.

Graversen, R. G., P. L. Langen, and T. Mauritsen (2014). "Polar Amplification in CCSM4: Contributions from the Lapse Rate and Surface Albedo Feedbacks". *Journal of Climate* 27(12), pp. 4433–4450.

Olonscheck, D., T. Mauritsen, and D. Notz (2019). "Arctic sea-ice variability is primarily driven by atmospheric temperature fluctuations". *Nature Geoscience* 12(6), pp. 430–434.

Colman, R. A. and B. J. McAvaney (1997). "A study of general circulation model climate feedbacks determined from perturbed sea surface temperature experiments". *Journal of Geophysical Research: Atmospheres* 102(D16), pp. 19383–19402.

Soden, B. J., I. M. Held, R. Colman, K. M. Shell, J. T. Kiehl, and C. A. Shields (2008). "Quantifying Climate Feedbacks Using Radiative Kernels". *Journal of Climate* 21(14), pp. 3504–3520.

Klocke, D., J. Quaas, and B. Stevens (2013). "Assessment of different metrics for physical climate feedbacks". *Climate Dynamics* 41(5–6), pp. 1173–1185.

Popp, M., H. Schmidt, and J. Marotzke (2016). "Transition to a Moist Greenhouse with CO2 and solar forcing". *Nature Communications* 7, p. 10627.

Klein, S. A. and A. Hall (2015). "Emergent Constraints for Cloud Feedbacks". *Current Climate Change Reports* 1(4), pp. 276–287.

Qu, X., A. Hall, A. M. DeAngelis, M. D. Zelinka, S. A. Klein, H. Su, B. Tian, and C. Zhai (2018). "On the Emergent Constraints of Climate Sensitivity". *Journal of Climate* 31(2), pp. 863–875.

Bender, F. A., A. M. Ekman, and H. Rohde (2010). "Response to the eruption of Mount Pinatubo in relation to climate sensitivity in the CMIP3 models". *Climate Dynamics* 35(5), pp. 875–886.

Hargreaves, J., J. Annan, M. Yoshimori, and A. AbeOuchi (2012). "Can the Last Glacial Maximum constrain climate sensitivity?" *Geophysical Research Letters* 39(24), p. L24702.

Hargreaves, J. and J. Annan (2016). "Could the Pliocene constrain the equilibrium climate sensitivity?" *Climate of the Past* 12(8), pp. 1591–1599.

Renoult, M., J. D. Annan, J. C. Hargreaves, N. Sagoo, C. Flynn, M.-L. Kapsch, U. Mikolajewicz, R. Ohgaito, and T. Mauritsen (2020). "A Bayesian framework for emergent constraints: case studies of climate sensitivity with PMIP". *Climate of the Past*.

Caldwell, P. M., C. S. Bretherton, M. D. Zelinka, S. A. Klein, B. D. Santer, and B. M. Sanderson (2014). "Statistical significance of climate sensitivity predictors obtained by data mining". *Geophysical Research Letters* 41(5), pp. 1803–1808.

Nijsse, F. J. M. M., P. M. Cox, and M. S. Williamson (2020). "An emergent constraint on Transient Climate Response from simulated historical warming in CMIP6 models". *Earth System Dynamics Discussions*.

List of Figures

List of Tables

Acknowledgments

Many that live deserve death. And some that die deserve life. Can you give it to them? Then do not be too eager to deal out death in judgement.

Gandalf, The Lord of the Rings, J.R.R. Tolkien

I would like to thank Thorsten Mauritsen for his patience and continuous support, even during the worst moments in this journey. His advice made this thesis possible. I also thank Björn Stevens and Stefan Buehler for their support, ideas and evaluations. I learned from Jochem Marotzke, Thorsten and Björn how to concisely express my findings. For that knowledge, I am genuinely grateful, given that communicating our science is as important as the research itself.

After the doctoral defence on 11 June 2020, I would like to thank the evaluation committee for the time spent revising this doctoral thesis. Their enquiries at the examination helped me to reflect on what I have done during my doctoral studies. I acknowledge them explicitly: Prof. Dr Johanna Baehr, Prof. Dr Thorsten Mauritsen, Prof. Dr Uwe Schneider, Prof. Dr Björn Stevens and Prof. Dr Nedjeljka Žagar. Especially, I thank Prof. Dr Žagar for the excellent organisation of the examination session.

I dearly acknowledge the great effort that my beloved Violeta Arriola made during these almost four years. We spent most of this time away from each other but never apart. She has continuously supported me either with her affection or with her comments on my work. When the menacing storms were there, she made things to shine. *Elen síla lúmenn' omentielvo*.

I would also like to thank Jiawei Bao, Sally Dacie, Gábor Drótos, Katherine Fodor, George Geet, Clarissa Kroll, David Nielsen, Laura Paccini and Hauke Schmidt for their kind help as friends and proofreaders. Our conversations converted the first two chapters in a brief introduction to the discipline. This was the goal. I think that we are there not only to communicate the science but to introduce new people into the topics that we study. I thank, as well, Renate Brokopf, Angela Gruber and Sebastian Rast for their help. I also thank all the friends, either from the IMPRS or from the MPI-M, that I found during this journey.

The IMPRS-ESM Office team, which includes Antje Weitz, Connie Kampmann and Michaela Born, were fundamental in solving not only bureaucratic problems but also other kinds of issues. They fully understand that doctoral studies are difficult and care for us. I cannot thank them enough.

Finalmente, agradezco en mi lengua natal a mi familia. Mi madre Susana Jiménez de la Cuesta Otero hizo posible que hoy esté aquí. Con el gran cariño con el que me crió con la ayuda de mi abuela, formó un hombre completo. Aunque con miedos y defectos, he descubierto la felicidad en lo que hago y en mi vida con Violeta. Dedico esta tesis a mi

abuelo Javier Jiménez de la Cuesta Zamora y Duque de Heredia. Aunque no lo conocí, siempre ha sido un referente de esfuerzo y de ética.

Pero por sobre todos, le dedico esta tesis a mi abuela Susana Otero Carpio, que tanto me inspiró y apoyó. Me quiso como a un hijo, yo la quiero como a una madre.

Versicherung an Eides statt

Hiermit versichere ich an Eides statt, dass ich die vorliegende Dissertation mit dem Titel: "Historical Warming and Climate Sensitivity" selbstständig verfasst und keine anderen als die angegebenen Hilfsmittel —insbesondere keine im Quellenverzeichnis nicht benannten Internet-Quellen — benutzt habe. Alle Stellen, die wörtlich oder sinngemäß aus Veröffentlichungen entnommen wurden, sind als solche kenntlich gemacht. Ich versichere weiterhin, dass ich die Dissertation oder Teile davon vorher weder im In- noch im Ausland in einem anderen Prüfungsverfahren eingereicht habe und die eingereichte schriftliche Fassung der auf dem elektronischen Speichermedium entspricht.

Hamburg, den 06.04.2020

Diego Jiménez-de-la-Cuesta Otero

Hinweis / Reference

Die gesamten Veröffentlichungen in der Publikationsreihe des MPI-M
„Berichte zur Erdsystemforschung / Reports on Earth System Science“,
ISSN 1614-1199

sind über die Internetseiten des Max-Planck-Instituts für Meteorologie erhältlich:
http://www.mpimet.mpg.de/wissenschaft/publikationen.html

All the publications in the series of the MPI -M
„Berichte zur Erdsystemforschung / Reports on Earth System Science“,
ISSN 1614-1199

are available on the website of the Max Planck Institute for Meteorology:
http://www.mpimet.mpg.de/wissenschaft/publikationen.html